Spring 2007

# An observer-based attitude and nutation control and flexible dynamic analysis for the NASA Magnetospheric Multiscale Mission

Neil Mushaweh
*University of New Hampshire, Durham*

# AN OBSERVER-BASED ATTITUDE AND NUTATION CONTROL AND FLEXIBLE DYNAMIC ANALYSIS FOR THE NASA MAGNETOSPHEREIC MULTISCALE MISSION

BY

NEIL MUSHAWEH

B.S., University of New Hampshire, 2005

THESIS

Submitted to the University of New Hampshire
in partial fulfillment of
the requirements for the degree of

Master of Science

in

Mechanical Engineering

May 2007

UMI Number: 1443623

INFORMATION TO USERS

The quality of this reproduction is dependent upon the quality of the copy submitted. Broken or indistinct print, colored or poor quality illustrations and photographs, print bleed-through, substandard margins, and improper alignment can adversely affect reproduction.

In the unlikely event that the author did not send a complete manuscript and there are missing pages, these will be noted. Also, if unauthorized copyright material had to be removed, a note will indicate the deletion.
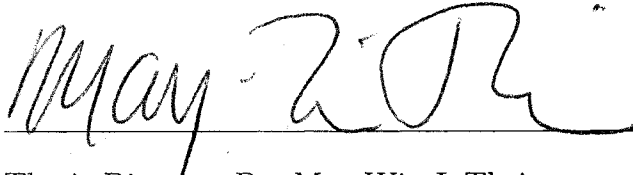
# UMI®

UMI Microform 1443623

Copyright 2007 by ProQuest Information and Learning Company.

All rights reserved. This microform edition is protected against unauthorized copying under Title 17, United States Code.
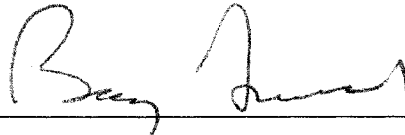
ProQuest Information and Learning Company
300 North Zeeb Road
P.O. Box 1346
Ann Arbor, MI 48106-1346

This thesis has been examined and approved.

Thesis Director, Dr. May-Win L. Thein

Associate Professor of Mechanical Engineering

Dr. Barry Fussell

Professor of Mechanical Engineering

Dr. L. Gordon Kraft, III

Professor of Electrical and Computer Engineering

Dr. Igor Tsukrov

Associate Professor of Mechanical Engineering

5/10/07

Date

# TABLE OF CONTENTS

iv

# LIST OF TABLES

# LIST OF FIGURES

# ABSTRACT

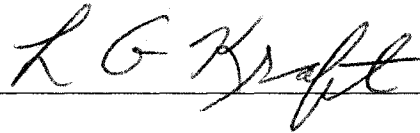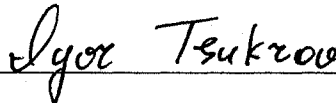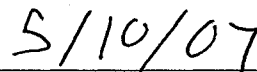## AN OBSERVER-BASED ATTITUDE AND NUTATION CONTROL AND FLEXIBLE DYNAMIC ANALYSIS FOR THE NASA MAGNETOSPHEREIC MULTISCALE MISSION

by

NEIL MUSHAWEH

University of New Hampshire, May, 2007

Current research with the NASA Goddard Space Flight Center (GSFC) involves the dynamic modeling and control of the NASA Magnetosphereic Multiscale (MMS) Mission, a Solar-Terrestrial Probe mission to study Earth's magnetosphere. Four observer-based attitude and nutation controllers are designed and evaluated to determine the most effective feedback control system as it applies to MMS. Also, a dynamic analysis of each of the four identical satellites' two Axial Double Probe (ADP) booms is performed to provide an understanding of flexible boom dynamics.

The Finite Element method is used in evaluating boom modes of vibration for confirmation of NASA GSFC theoretical analysis and use in flexible model development. The dynamic transient and modal extraction technique are investigated for vibration analysis of constrained and unconstrained bodies. A fully flexible boom and rigid spacecraft model is also developed for vibrational analysis under steady-state rotation and thruster loads. Results indicate, however, the need for future research in numerical analysis of propagating systems through finite element methods and in the stability of the observer-based control system.

Linear and nonlinear observers are developed through simulations to estimate satellite attitude and angular body rates without the use of rate sensors. Control systems are then developed assuming perfect state measurements. Euler angles are used to describe satellite attitude in this research. Finally, linear and nonlinear (Sliding Mode Control) techniques

are implemented in conjunction with the nonlinear observers to complete the observer-based control system.

The results of this research show that, of the methods analyzed, both the Extended Kalman Filter and Sliding Mode Observer implemented with Sliding Mode Control yield the most satisfactory performance. These observer-based control systems both meet NASA design requirements while reducing thruster control effort and reducing the effects of measurement noise and spacecraft uncertainties/disturbances. More simulations, however, are needed to verify performance of the proposed observer-based control system over all possible ranges of operation.

# CHAPTER 1

# INTRODUCTION

## 1.1 Objective

The NASA Magnetospheric Multiscale (MMS) satellite constellation is scheduled for launch in 2013. Each satellite is composed of six instrumentation booms reaching up to 50 meters in length that will be used to collect astrophysical data. Once operational, the three satellite formation will provide a three dimensional understanding of the Earth's magnetosphere, small scale plasma processes and other astrophysical phenomena.

The mission will progress in three stages, each requiring large orbital maneuvers. These large orbital transfers, coupled with the high sensitivity of the instruments, require the satellite to maintain a constant pure rotation about its local z-axis. Mass imbalances, external torques and other unknown disturbances cause the satellite to tend to nutate about its x and y axis undesirably. In order to effectively reject all satellite nutation, while maintaining a constant spin, it is essential that the satellite angular body rates are accurately known.

A finite element analysis is performed on the satellites highly flexible instrumentation booms. A dynamic analysis is used to extract boom natural frequencies, modes of vibration and provide an overall understanding of the flexible boom dynamics through transient simulations. This analysis is used to aid NASA engineers in the development of a mathematical model that will be used in orbital control, while laying the foundation for the integration of attitude estimation based nutation and orbital

control on a fully flexible spacecraft model.

This thesis also investigates the feasibility of an estimation algorithm that is capable of determining spacecraft angular rates with only star tracker attitude measurements. The focus of this research is on the rotational (attitude) dynamics of the spacecraft rather then the translational motion (orbit). Although these dynamics are highly coupled, the work in this thesis will decouple attitude and orbital dynamics (the control of an integrated attitude/orbital system is left for future work). The application of such estimation capabilities has implications on designs that avoid costly angular rate measurement systems while maintaining highly accurate state representations. These body rate estimates will then be used in a control algorithm that will utilize thrusters to reject satellite spin nutation. Several estimation and control techniques are explored and compared to deliver the most effective results given NASA design requirements.

The MMS satellite has 6 instrumentation booms (2 Axial Double Probe, 4 Spin Double Probe) that extend up to 50 meters in length at just under two millimeters of thickness. These highly sensitive instruments require that the satellite spin at a constant rate about its $z$-axis at 0.3 $rad/s$ while rejecting nutation (as a result of mass imbalances and/or disturbance torques) about the $x$ and $y$ axis ($\pm 0.02$ $rad/s$ $3\sigma$) which may occur from mass imbalances, or external torques. While maintaining these satellite body rates, the spacecraft must also have an orientation that is 3 degrees ($\pm$ 0.009 $rad$ $3\sigma$) about its $x$ and $y$ body-fixed reference frame.

Much research has been performed in the area of spacecraft attitude estimation and control. Additionally, the analysis of flexible space structures and flexible structure control has been a recently expanding field of research. Past research in the field of estimation, control, and flexible structure analysis will be provide a foundation for this research to expand upon. This thesis will investigate observer-based attitude

control systems for a flexible spacecraft while attempting to provide a design tool through finite element models for estimation and control design.

## 1.2  Finite Element Analysis: Overview

Finite Element Analysis (FEA) is an engineering tool that is applied to applications ranging from aerospace structural analysis, to heat transfer and electromagnetic design and analysis. As technology in solid modeling of mechanical systems and numerical analysis has advanced, the use of FEA methods on complex engineering applications has greatly increased. Today, research and development of FEA software packages is still improving and advancing the effectiveness of FEA, particularly in dynamic applications where large deformations occur.

FEA is a numerical method that involves discretization of a continuous system through interconnected finite elements connected at nodal points and constrained boundary conditions. Rather than directly soloving nonlinear time-dependent differential equations that mathematically describe a system, FEA results in systems of algebraic equations. These sometimes very large systems of equationsare solved via digital computers and numerical techniques to determine approximations of system parameters for very complex bodies. The system parameters, would, otherwise be extremely difficult to analyze through continuous equations. FEA can offer approximations of displacements and stresses at each node for structural applications, while temperatures and pressures can be found for thermal-fluid systems.

Analysis of flexible space structures has been an increasingly researched field with the high demand for cheap, light and strong spacecraft components. Lee [2] proposes dynamic continuum modeling through finite element methods for beamlike space structures which has proven to yield accurate results compared to existing methods. Hutton [3] uses modal analysis through finite element methods to investigate

dynamic characteristics of large deployable space structures. Also, Pai and Wheater
[4] present a displacement based finite element method for beams experiencing large
displacements and rotations. This type of research is particularly useful because it
offers insight into dynamic transient responses of flexible structures. Such an analysis
is helpful in understanding flexible dynamics of the NASA MMS spacecraft. How-
ever, estimation and control of the spacecraft is not considered or implemented with
the developed flexible models. This research investigates flexible structures, while
laying the foundation for an observer-based control system for a satellite with flexible
appendages.

## 1.3 Attitude Determination and Control: Overview

Attitude dynamics are used to describe a spacecraft's orientation and angular mo-
tion under the influence of external moments with respect to a fixed inertial reference
frame. In order to understand a spacecrafts attitude dynamics in space, it is essential
to obtain accurate representations of angular positions and velocities in real time.
From knowledge of these states, an automatic feedback control algorithm may be
used to rotate a spacecraft to a desired orientation, rotate the spacecraft at a desired
rate or both.

In some applications spacecraft are required to maintain an orientation within
strict design requirements due to flexible appendages, such as instrumentation booms
or solar arrays. Today's missions demand that all attitude control requirements are
met while minimizing cost. Attitude determination is a technique used to reconstruct
attitude states from real time sensor data. It can be useful in meeting design require-
ments and improving the control design while reducing costs by avoiding the use of
expensive measurement systems.

Attitude determination techniques arise from the need of understanding attitude

dynamics from corrupted or nonexistent measurement data. The attitude determination, or estimation, process works by comparing real time measurements with a dynamic model that is developed off line. By comparing measurement data of the spacecraft dynamics with what is believed to be happening from the spacecraft model, an error signal is produced. This error signal is then used in an algorithm, called an observer, to force the error signal to zero. When the error signal is at or approaching zero, the state estimates are then used to update implemented control algorithms. Measurement noise, unknown disturbances, inaccurate system models, and parametric uncertainties are just a few reasons why attitude determination methods are augmented with spacecraft sensor systems. As spacecraft have become smaller, the availability of complex measurement systems has decreased due to financial design constraints and size limitations. It is for both of these reasons that gyroscopes are typically avoided in spacecraft design. Gyroscopes are a measurement device that provide real time angular rate data of a spacecraft in orbit. Not only do these sensors consume space and are expensive, they also have a tendency to "drift" which require real-time re-calibration that is undesirable for long missions. They are also prone to failure.

In most satellite applications, there are design requirements on both the attitude and angular rate. For satellites that require solar arrays to generate electrical power, it is necessary to adjust the orientation of the satellite frequently to optimize the amount of solar power. Many satellites are spin-stabilized, requiring the satellite to maintain a constant spin rate. In both instances, actuators are used to orientate or spin the spacecraft at desired values based on the real time attitude dynamics. As with observer techniques, many different control algorithms exist and specific techniques are chosen accordingly, depending on the specific mission.

Multiple sensor and actuator systems can be used on satellite missions and are

usually thoroughly explored during the design phase. In the following section, a brief description of various types of attitude sensing and actuating hardware is provided.

## 1.4 Attitude Hardware

The combination of attitude sensing hardware with orientation and angular rate actuation can function in several different configurations. For attitude sensing hardware, there exist two classifications: (1) vector sensors, that can provide magnitude and direction of a specific measurement, and (2) relative sensors that provide changes of attitude orientation or rate relative to a fixed reference frame. Some common methods for satellite control include: propulsion systems, momentum exchange devices, and magnetic torqrods. All descriptions of attitude hardware presented have been adopted from [5], [6] and [1].

### 1.4.1 Attitude Sensing

**Star Sensors:** Star sensors are an optical attitude sensing system that detect light emitted from stars and can calculate the orientation of the satellite based on the known fixed inertial frame of the stars. A satellite computer contains star catalogues and provides star characteristics, such as visual magnitude and spectral type, that allow the sensor to differentiate between stars. There are three common types of star sensors that are used for attitude measurements: fixed-head star trackers, gimbaled star trackers, and star scanners. The fixed-head star trackers use electronics to scan the sky that is within the sensor's field of view to acquire and track selected stars. This type of attitude measurement is typically used in three axis stabilized satellites. The gimbaled star tracker is similar to the fixed-head star tracker, except that rather then electronically scanning the sensor field of view it mechanically scans the sky which allows for a large quantity of stars that can be used for tracking. The sim-

plest of star sensors is the star scanner, which is used for spin stabilized satellites in which the attitude of the spin axis must be known and does not require knowledge of all three body axes. The advantage of these types of sensors is their accuracy which is typically on the order of arc-seconds (one of the most accurate attitude sensors). The disadvantage of star sensors is that they require high amounts power and computational resources and can be effected by background celestial light.

**Sun Sensors:** Sun sensors are the most commonly used attitude sensing device on satellites when one or two axis determination is needed. As opposed to using stars as references for attitude determination, the Sun is optimal because of its large size and high luminosity. The Sun's luminosity makes a sensor less susceptible to inaccurate readings due to background celestial light. The two main types of sun sensors that exist are analog and digital sensors. Analog sun sensors work by generating a current that is proportional to the incident of the sun angle $\alpha$. Although analog sensors are not as accurate as digital sensors, they are cheaper, take up less payload and are mechanically and electrically simple. Digital sun sensors, however, have a higher accuracy then analog sensors $(0.017^o)$ with a higher field of view, providing more versatility in attitude determination.

**Infrared Earth Sensors:** Infrared Earth (IRE) sensors use two different methods to determine the attitude of a satellite with respect to the Earth. Horizon sensors and static determination are both designed to detect temperature gradients between space and the Earth's atmosphere. IRE sensors are useful for any satellite application in which the orientation of the Earth is important (i.e. weather observation, navigation, communications). An advantage to IRE sensors is their reference is the second brightest celestial object, aside from the Sun. The most obvious disadvantage to IRE sensors is their proximity to Earth restricts the sensors' field of view and will sometimes require the sensor to mechanically scan space, involving complex mechanical

components.

**Magnetometers:** Magnetometers are a vector sensing device that uses a combination of sensor outputs and mathematical models of the Earth's magnetosphere to determine attitude. The magnetometers output a magnitude and direction with respect to the magnetic field. The advantage of these types of sensors is that they are lightweight and have low power requirements with effectiveness over large temperature ranges. These capabilities make these sensors desirable at low Earth orbits. However, because the sensor outputs must be combined with mathematical predictions, many problems can occur. Substantial errors in satellite position magnitude can occur because of inaccuracies in magnetic field models. Also, as satellite orbits increase with altitude, magnetic field strength decreases, making magnetometers less effective in determining attitude.

**Gyroscopes:** A gyroscope or gyro is a sensor used for satellite rate determination. In all gyros, a rotating mass is used to sense changes in the orientation of the spin axis. Rate integrating gyros are used to measure angular displacements of the satellites spin axis, while rate gyros directly measure spacecraft angular rates. These types of instruments have many advantages and disadvantages in attitude determination and control. They are highly effective in situations where it is essential to maintain constant satellite spin when attitude position measurements are not able to be differentiated. Disadvantages with gyros include cost, significant measurement noise, and (most importantly), drift. Drift occurs typically in rate integrating gyros at a rate of $0.03^{\circ}/hr$ to $1^{\circ}/hr$ and can have negative effects on satellite attitude determination. As discussed below, gyros are also used in satellite attitude control in the form of a momentum exchange actuator.

## 1.4.2 Satellite Actuators

**Propulsion Systems:** Propulsion systems use jets or thrusters to produce forces and torques on a spacecraft body. The advantage to propulsion systems is the versatility of the forces and torques they produce. Thrusters and jets are used for orbital transfers, attitude control, spin control, and nutation control. There are two main categories of thrusters: chemical, and cold gas. Chemical thrusters are the most powerful of the propulsion systems and use either a solid or liquid as the propellent. Solid fueled thrusters can deliver thrusts up to hundreds of thousands of Newtons (typically used when large changes in velocity are needed to escape Earth's gravitational force or to change orbits). The drawback of solid propellant thrusters is that once ignited, they continue to burn until the propellant is completely used. The cold gas propulsion systems use a compressed gas to produce a force or torque on a spacecraft. These types of thrusters can deliver about 5 Newtons of force and have impulses of approximately 50-70 seconds. Cold gas thrusters require pressure vessels that can withstand high amounts of pressure, which adds weight to the overall payload and is the main disadvantage of cold gas propulsion.

**Momentum Exchange Devices:** Momentum exchange actuators use a rotating flywheel to impart a momentum change on the spacecraft body, thus creating a torque. These types of actuators are used for multiple purposes, including rejection of disturbance torques, attitude actuation, and spacecraft spin control. The flywheel is rotated by an electrical motor and thus, requires no fuel and does not significantly change spacecraft parameters (such as mass and moments of inertia) throughout the mission. A common type of momentum exchange device is the control moment gyro (CMG) which works by changing the momentum vector of the flywheel inside of the spacecraft body, producing a control torque about the spin axis. Momentum exchange devices typically deliver a control torque ranging from .01-1 N-m [7] and are

designed to operate on missions lasting 5-12 years. The major drawback of momentum exchange devices is the need for lubrication of mechanical bearings in a space environment to prevent excessive frictional damage.

**Magnetic Torqrods:** Torqrods are capable of generating a magnetic moment on a spacecraft by energizing a magnetic core and coil while in the Earth's magnetic field. They are used in multiple attitude applications and, like momentum exchange devices, do not require consumable fuel to be effective, thus eliminating weight, fuel slosh, and constantly changing spacecraft parameters. The major drawback of torqrods is their ineffectiveness at high orbits due to a weak magnetic field, and corruption of attitude measurements if used with magnetometer senors.

## 1.5 Attitude Determination and Control Methods

Attitude determination and control has become a highly researched topic in the last 50 years since the need for efficient and cheap satellites has risen for communications, scientific and defense applications. In nearly all spacecraft applications, the control law is said to be a feedback control system, in which measured or estimated data is fed back to the controller to update the implemented control algorithm. One of the first applications of this kind of control law was developed in 1620 by Cornelis Drebbel to control the temperature of a furnace in an incubator. Another benchmark application of feedback control came in 1788 as a means of controlling shaft speed in steam engines developed by James Watt. The fly-ball governor, as it became to be known as, used centrifugal force to maintain a constant shaft speed when engine loads were applied. The next breakthrough in feedback control came in 1936 from Callender, who developed the proportional-integral-derivative (PID) control. The PID control law worked off linearized approximations of nonlinear systems and, at the same time, allowed for the development and research of guiding and controlling aircraft. It was

also about this time that sensors were being developed to measure aircraft altitude and speed to be used in feedback control laws. With sensor development, there was much measurement noise that corrupted data and, thus, led to the development of statistically optimal filters by Wiener in 1940. These foundations which came to be known as classical control and signal processing lead to modern control theory and estimation. It was R. Bellman and R.E. Kalman who first began looking at differential equations as the model to base control design. This advance, was driven by the need to control Earth orbiting satellites with the newly available technology of digital computers. Work done by Grasshoff [8] and Lin [9] explore nutation control through accelerometer measurements and thruster actuation. However neither offer a comprehensive comparison of nonlinear and linear observer based control systems. Wilson [10] also presents a bang-bang control method for spin reduction and stabilization of space vehicles using gas jets. This prior research serves as a reference in the development and comparison of an observer based controller for the NASA MMS mission.

The Kalman filter is a recursive estimation technique that uses sensor measurements and state space system models, which are linearized equations about an operating point, to estimate desired states. Application of Kalman filters to spacecraft estimation was first introduced by E.J. Lefferts [11] in 1982 to use attitude measurement vectors combined with gyro outputs to estimate satellite attitude. It is also not uncommon to find that linear Kalman filters are not sufficient in estimating states of highly nonlinear systems, which is the case for many spacecraft applications. A nonlinear extension to the Kalman filter linearizes the system equations about each estimated state, rather than a predetermined operating point (as with the Kalman filter), and is referred to as the Extended Kalman Filter (EKF). Using this state estimation technique, many researches have proposed algorithms that use one set of

sensor data to obtain a full understanding of states and torques. Psiaki [12] used magnetomentor vector measurements to determine attitude, angular rates, and external torques while Gai [13] used star sensor measurements to determine attitude and angular rates. In another application of nonlinear filters, Markley and Crassidis [14] used a feed-forward predictive estimator to determine attitude, rate and model error trajectories without gyroscopic sensors.

A nonlinear variable structure technique for state estimation is called the Sliding Mode Observer (SMO). In the standard SMO, two sets of fixed gains (the Luenberger gains and switching gains) are used, unlike the EKF which uses time-varying gains, resulting in high computational demand of onboard spacecraft computer systems. A drawback of the SMO is its use of saturation or signum functions in the sliding surface formulation which tend to cause chattering of state estimates. The SMO is noted for robustness to modeling uncertainty and unknown disturbances. The SMO is an extension of the Sliding Mode Controller, where the estimation error trajectory, rather then the control error trajectory, is made to converge to zero. Applications of variable structure estimation and control include Luk'yanov [15] who used an SMO to control a spacecraft while excluding rate estimates. Misawa has done extensive research in the field of nonlinear estimation and sliding mode observers [16], [17].

Significant amounts of research has also been performed in the area of flexible structure control. Gale [18] investigated the influence of flexible appendages on dynamic behavior and control response for spacecraft using gas jets. Also, Wei [19] investigated nonlinear dynamics and stability of a gas jet, spin-stabilized flexible spacecraft. An optimal control method for damping flexible spacecraft through the use of momentum wheels was presented by Meirovitch [20]. Finally, a variable structure controller for a spin-stabilized spacecraft by [21] is one of many examples of flexible structure control.

Although these studies offer insight into the application of sliding mode control and estimation, they do not implement an observer-based attitude control system for flexible structures sufficient for specific application to the NASA MMS mission.

The goal of this thesis is to explore two nonlinear state estimation techniques to be used in an observer-based control system specifically for use in the NASA MMS mission. Each system is evaluated on its effectiveness to reject satellite nutation, while maintaining a desired satellite orientation and desired body rates. The state estimate techniques (EKF and SMO) are developed separately from the feedback controllers (linear and SMC). The various state estimate techniques are then implemented in the closed-loop feedback controller, where the entire observer-based control system is analyzed through simulation. Also, flexible boom dynamics are investigated through finite element techniques. This part of the research is useful in developing mathematical models that account for flexible dynamics as well as provide an understanding of these influences on estimation and control effectiveness and will be used in future work.

## 1.6   Thesis Outline

The following chapters are organized as follows:

- Chapter 2, Spacecraft Attitude Models - An overview of coordinate systems used in orbital and attitude dynamics are introduced. Next, Euler angle representations of spacecraft attitude kinematics, Euler moment equations for spacecraft rotational rigid-body dynamics, and flexible spacecraft dynamics are discussed.

- Chapter 3, Spacecraft Attitude Estimation and Control Techniques - Linear and nonlinear estimation and control methods are discussed and mathematically introduced for application to nutation rejection via body rate estimates.

- Chapter 4, Finite Element Methods for Dynamic Modeling - Finite element analysis is introduced followed by numerical techniques for dynamic response resulting from flexible modes and modal extraction for vibrating systems.

- Chapter 5, Finite Element Results for Dynamic Responses - Satellite flexible boom modes of vibration are extracted using finite element methods. The foundation for this flexible model approach to satellite estimation and control design is presented.

- Chapter 6 , Attitude Estimation Results - A comparative study is performed using the Extended Kalman Filter and Sliding Mode Observer techniques to determine the most effective method of state estimation without gyroscopic measurements. Simulation results are investigated for steady state error, measurement noise and unknown disturbance torque robustness.

- Chapter 7, Attitude Control of Perfect Measurements - Control techniques are designed for attitude and rate control assuming that perfect state measurements are available. Linear and nonlinear methods are explored and simulation results are presented.

- Chapter 8, Observer-Based Control - Both estimation techniques explored in Chapter 6 are used to update feedback control algorithms. Results are presented and analyzed to determine the optimal estimation and control system as it applies to the MMS mission.

- Chapter 9, Conclusions and Future Work - Contributions of this thesis to the MMS mission are summarized and, future research is itemized.

# CHAPTER 2

# SPACECRAFT ATTITUDE MODELS

Attitude is defined as the orientation of a body in space. One method in which the orientation is described is through a series of rotations that transform the body-fixed coordinate system of the spacecraft to an inertial fixed reference frame. An introduction to coordinate systems, the kinematics of parameters used to define an orientation, and the dynamics of these attitude parameters under applied forces are all necessary to fully understand a spacecraft attitude model.

Section 2.1 introduces coordinate reference frames that are used as the foundation to relate spacecraft orientation to fixed bodies such as the Earth, Sun, or other stars. Once an understanding of coordinate systems is established, the relative motion (or kinematics) of a spacecraft with respect to a reference frame is discussed in Section 2.2. To finish the attitude mathematical model, rigid body dynamics of a rotating spacecraft are introduced in Section 2.3. Finally, flexible dynamics of a spacecraft are discussed in Section 2.4 to establish a fundamental understanding of elastic structural effects on the overall system and system model. This material has been adopted from [5], and [1] as well as [7], and the reader should refer to this material for further detail.

## 2.1 Coordinate Systems

Spacecraft centered and non-spacecraft centered systems are the two common forms of coordinate systems used in describing the dynamics of a spacecraft. Typ-

ically, non-spacecraft centered systems are used in orbital dynamic models, while spacecraft centered systems are utilized in attitude dynamic models. In instances where orbital and attitude dynamics are being formulated, a clear understanding of coordinate systems coordinate transformations is essential. The scope of this research focuses on dynamic models that utilize spacecraft centered coordinate systems for attitude dynamic formulations. The main spacecraft-centered systems are described below.

### 2.1.1 Spacecraft-Centered Coordinate Systems

**Spacecraft Inertial (SCI) Coordinates**: This is the most common coordinate system when describing spacecraft motion. The origin of this reference frame translates with the spacecraft and is defined relative to the rotation axis of the Earth. The axes of this frame are fixed in inertial space and are parallel to the Earth-centered inertial frame. The Earth centered inertial frame is a common non-spacecraft centered coordinate system and is fixed at the Earth's center. This frame, as with the spacecraft frame, is allowed to translate with Earth, but does not rotate about its spin axis.

**Spacecraft Fixed (SCF) Coordinates**: Since all attitude measurements are made with respect to the spacecraft fixed coordinates, this reference frame is ideal for attitude determination and control applications. SCF are fixed to the center of mass of the spacecraft and are allowed to rotate and translate with the spacecraft. In most cases, the axes of this reference frame are selected based on the principle axes of inertia of the spacecraft.

**Orbit Defined Coordinate Systems**: The axes of the orbit coordinate system are defined based on the orbit of the spacecraft. For this type of reference frame, the spacecraft x-axis is defined in the direction of orbital velocity, while the z-axis is the
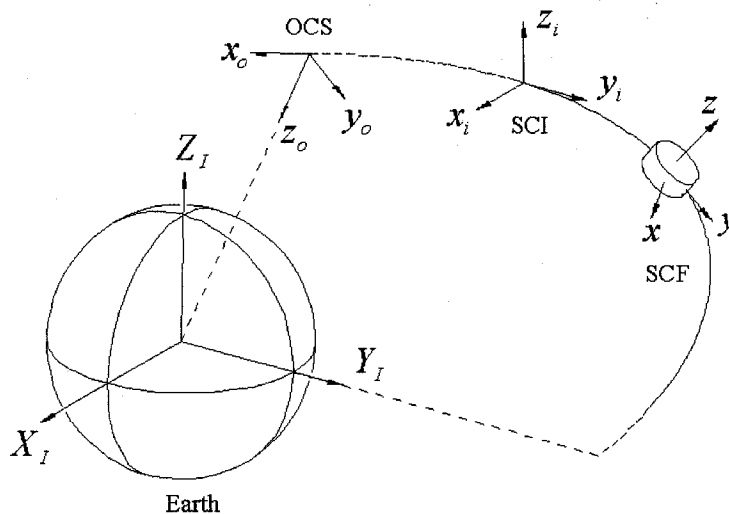
Figure 2-1: Spacecraft centered coordinate systems with respect to the Earth [1]

nadir vector, and the final y-axis is defined by completing dextral triad (right-hand rule). The origin of this reference frame, as with all spacecraft-centered coordinate systems, is fixed at the spacecraft center of mass.

Figure 2-1 shows the relationship of each of the three spacecraft-centered coordinate systems with respect to the Earth.

## 2.2 Attitude Parameterizations

The most basic representation of the orientation of a body in space is the attitude matrix. This matrix transforms a reference frame into a body-fixed frame of a spacecraft. There are several parameterizations that satisfy the attitude matrix, which is determined through successive rotations in space. The direction cosine matrix, and the Euler Angle rotation sequence are two common parameterizations that are used to determine an attitude matrix through rotations. A problem with these types of parameterizations is the occurrence of singularities and discontinuities that arise when inverse trigonometric functions appear in the transformation matrix. The
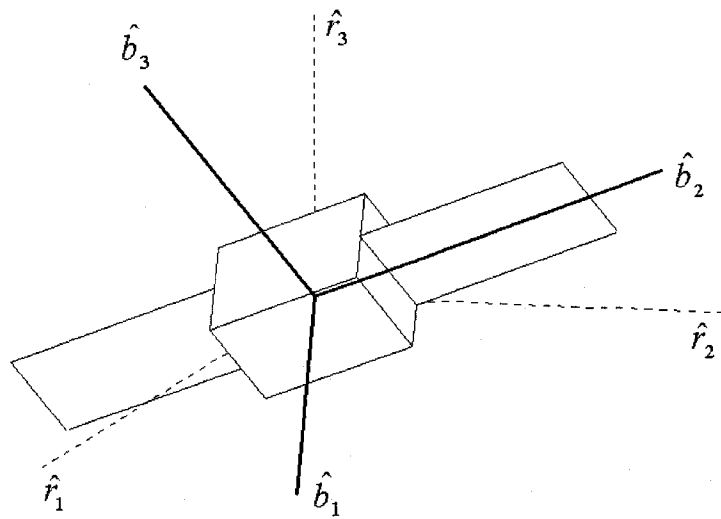
Figure 2-2: A reference frame and body fixed frame of a spacecraft in orbit [1]

Gibbs vector and Quaternion are two methods that use vectors and rotation angles to determine the attitude matrix of a spacecraft. In this research, the Euler Angle sequence is implemented in the dynamic model formulation.

## 2.2.1 Direction Cosine Matrix

A direction cosine matrix is simply the matrix which describes the cosine of the angle between two unit vectors in different reference frames. The direction cosine matrix (also called the attitude matrix or transformation matrix) is a $3 \times 3$ orthogonal matrix that represents the orientation of one reference frame with respect to another. For example, let $(\hat{r}_1, \hat{r}_2, \hat{r}_3)^T$ and $(\hat{b}_1, \hat{b}_2, \hat{b}_3)^T$ represent the unit vectors of a inertial reference frame and body-fixed frame respectively, as illustrated in Figure 2-2.

The direction cosine matrix that describes the orientation of the body fixed frame

with respect to the reference frame is:

$$\begin{bmatrix} \hat{r_1} \\ \hat{r_2} \\ \hat{r_3} \end{bmatrix} = \begin{bmatrix} C_{11} & C_{12} & C_{13} \\ C_{21} & C_{22} & C_{23} \\ C_{31} & C_{32} & C_{33} \end{bmatrix} \begin{bmatrix} \hat{b_1} \\ \hat{b_2} \\ \hat{b_3} \end{bmatrix} \tag{2.1}$$

where $C_{ij} = \hat{r_i} \cdot \hat{b_j} = cos(\hat{r_i}, \hat{b_j})$ and $(i,j=1,2,3)$ are the elements of the direction cosine matrix.

The direction cosine matrix in an orthonormal matrix, as the following properties hold true for all cases:

$$\mathbf{C^T} = \mathbf{C^{-1}} \tag{2.2}$$

which is equivalent to:

$$\mathbf{C^T C} = \mathbf{I} = \mathbf{CC^T} \tag{2.3}$$

Another important relationship of the direction cosine matrix is the ability to change the direction of transformation. For example, in Eq.(2.1), the relation shows the transformation from the body-fixed axis to an inertial reference frame, which can be shown as: $\mathbf{A} \rightarrow \mathbf{B}$ in which the direction cosine matrix can be defined as $\mathbf{C^{A/B}}$. To determine the direction cosine matrix $\mathbf{C^{B/A}}$ the following relationship holds true:

$$\mathbf{C^{B/A}} = \left[\mathbf{C^{A/B}}\right]^{-1} \tag{2.4}$$

The direction cosine matrix is the most basic form or representing spacecraft orientation. Since there are parameters of the transformation matrix that are redundant, the direction cosine matrix less desirable for application and simulation due to its high computational requirements. The Euler Angle approach offers an alternative to attitude matrix determination and is based on the same mathematical principals as the direction cosine matrix without parameter redundancy.
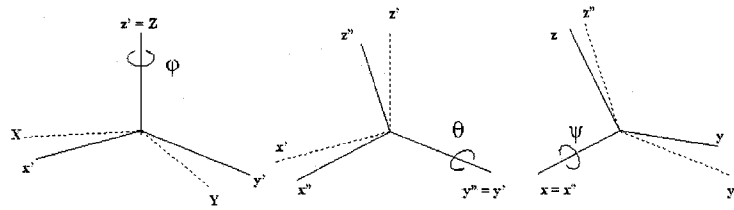
Figure 2-3: The 3-2-1 Euler rotation sequence [1]

## 2.2.2 Euler Angles

As with the direction cosine matrix, the Euler Angle approach to attitude representation involves an orthogonal transformation between the body fixed axis of a spacecraft and another reference frame. Euler angles accomplish this transformation through a series of pure rotations about the body-fixed reference frame. There are 12 possible rotations that can produce the attitude matrix of a spacecraft. Figure 2-3 shows the three possible rotations about the body-fixed reference frame for the 3-2-1 Euler angle rotation sequence which occurs about the $Z - y' - x''$ axes of the body frame respectively. The transformation to the final orientation $(x, y, z)$ is as follows:

1. A rotation about the $Z$ axis through angle $\phi$ to transform $X, Y, Z \rightarrow x', y', z'$

2. A rotation about the $y'$ axis through angle $\theta$ to transform $x', y', z' \rightarrow x'', y'', z''$

3. A rotation about the $x''$ axis through angle $\psi$ to transform $x'', y'', z'' \rightarrow x, y, z$

There are three possible orthogonal matrices that are used in each of the rotations which are functions of the angle they pass through. By multiplying these three matrices in the order of their transformation, the overall attitude matrix that relates

$X, Y, X$ to $x, y, z$ is as follows:

$$C = \begin{bmatrix} \cos\theta\,\cos\phi & \cos\theta\,\sin\phi & -\sin\theta \\ -\cos\psi\,\sin\phi + \sin\psi\,\sin\theta\,\cos\phi & \cos\psi\,\cos\phi + \sin\psi\,\sin\theta\,\sin\phi & \sin\psi\,\cos\theta \\ \sin\psi\,\sin\phi + \cos\psi\,\sin\theta\,\cos\phi & -\sin\psi\,\cos\phi + \cos\psi\,\sin\theta\,\sin\phi & \cos\psi\,\cos\theta \end{bmatrix}$$
$$(2.5)$$

This transformation is one of many Euler angle sequences that is used to describe the orientation of an object in space. The most noted disadvantage of this type of attitude representation is the singularities that arise from inverse trigonometric functions. Also, there is a high computational cost associated with Euler angle transformation matrices, especially when inverting matrices to obtain the reverse of the transformation. The rate of change of these Euler parameters $(\psi, \theta, \phi)$ is also important in understanding attitude dynamics and is presented in the following section. Other representations may be used that are more computationally efficient (e.g quaternions and Gibb's vector notation). However, Euler angle rotation is used because it is more physically understood more easily interpreted.

## 2.3  Attitude Kinematics

Attitude kinematics is a set of nonlinear differential equations that describe the rotational motion of a spacecraft about its center of mass. It is similar to that of the attitude matrix formulation, except the transformation between two reference frames is now time dependent. These equations are all functions of the time rate of change of attitude parameters. As with spacecraft attitude, attitude kinematics can be derived by several parameterizations. Since this research focuses on the Euler angle approach to attitude definition, the formulation of the kinematic equations remains consistent with that methodology. The derivation of the following equations is based on the 3-2-1 Euler angle sequence and is adopted from [1]. The major disadvantage of using

the Euler angle approach lies in the singularity that occurs at $\theta = 90^o$ that is refereed to as "gimbal lock". To avoid this singularity, it is assumed that all angular motion about the body axis is less then $90^o$.

### 2.3.1 Euler Angle Kinematics

The time dependency of Euler angles of the 3-2-1 sequence derived above will be formulated below.

The angular velocity of the spacecraft body fixed axis with respect to a fixed reference frame is defined as:

$$\boldsymbol{\omega}_{b/i} = \boldsymbol{\omega}_{b/o} + \boldsymbol{\omega}_{o/i} \tag{2.6}$$

where the angular velocity of the orbital reference frame with respect to the fixed reference frame is:

$$\boldsymbol{\omega}_{o/i} = -\omega_o \hat{\boldsymbol{j}}_o \tag{2.7}$$

and the spacecraft body-fixed frame with respect to the orbital reference frame is defined as:

$$\boldsymbol{\omega}_{b/o} = \dot{\phi}\hat{\boldsymbol{K}} + \dot{\theta}\hat{\boldsymbol{j}}' + \dot{\psi}\hat{\boldsymbol{i}}'' \tag{2.8}$$

The unit vectors correspond to the axis formed after each rotation during the Euler angle sequence. When all coordinates are transformed to the final reference frame $(\hat{\boldsymbol{i}}, \hat{\boldsymbol{j}}, \hat{\boldsymbol{k}})$ the angular velocity of the spacecraft with respect to a fixed reference frame can be defined as:

$$\boldsymbol{\omega}_{b/o} = \omega_{b/o_1}\hat{\boldsymbol{i}} + \omega_{b/o_2}\hat{\boldsymbol{j}} + \omega_{b/o_3}\hat{\boldsymbol{k}} \tag{2.9}$$

where the components of the angular velocity can be defined as:

$$\omega_{b/o_1} = -\sin\theta\,\dot{\phi} + \dot{\psi} \tag{2.10a}$$

$$\omega_{b/o_2} = \sin\phi\,\cos\theta\,\dot{\phi} + \cos\psi\,\dot{\theta} \tag{2.10b}$$

$$\omega_{b/o_3} = \cos\psi \, \cos\theta \, \dot{\phi} - \sin\psi \, \dot{\theta} \qquad (2.10\text{c})$$

To determine the Euler angle rates $(\dot{\phi}, \dot{\theta}, \dot{\phi})$ Eq.(2.10) can be arranged as follows:

$$\dot{\phi} = (\omega_{b/o_3} \, \cos\psi + \omega_{b/o_2} \, \sin\psi) \, sec\theta \qquad (2.11\text{a})$$

$$\dot{\theta} = \omega_{b/o_2} \, \cos\psi - \omega_{b/o_3} \, \sin\psi \qquad (2.11\text{b})$$

$$\dot{\psi} = \omega_{b/o_1} + (\omega_{b/o_3} \, \cos\psi + \omega_{b/o_2} \, \sin\psi) \, \tan\theta \qquad (2.11\text{c})$$

Eq. (2.11) is used to describe the first three states $(\dot{\phi}, \dot{\theta}, \dot{\psi})$ in the formulation of the spacecraft attitude dynamic equations of motion. The following section introduces spacecraft rigid-body dynamics, which is used in the derivation of the final three equations of motion for spacecraft attitude.

## 2.4 Rigid-Body Attitude Dynamics

Attitude dynamics describes the motion of an object due to applied moments, while orbital dynamics are concerned with the translating motion of a spacecraft center of mass due to external forces. This section focuses on the rotational motion of a spacecraft about its center of mass. The rigid body assumption for analyzing dynamic motion disregards internal energy dissipation due to structural elasticity. Although it may be necessary to analyze flexible structure dynamics for analytical completeness, when implementing estimation and control, these equations tend to be extremely complex and nonlinear, where as a rigid-body dynamic model is proven to be sufficient [6]. Later in this chapter, flexible structure dynamics are considered in order to analyze the corresponding effects on attitude control. Presently, however, rigid-body assumption is used for state equation formulations.

## 2.4.1 Rotational Dynamics

The fundamental equations governing rigid-body motion due to applied forces stem from the conservation of angular momentum principle. If there are no momentum exchange devices, then the angular momentum of a spacecraft can be defined as:

$$\mathbf{H} = \mathbf{I}\,\boldsymbol{\omega} = \begin{bmatrix} I_{xx} & -I_{xy} & -I_{xz} \\ -I_{yx} & I_{yy} & -I_{yz} \\ -I_{zx} & -I_{zy} & I_{zz} \end{bmatrix} \begin{bmatrix} \omega_x \\ \omega_y \\ \omega_z \end{bmatrix} \tag{2.12}$$

where $\mathbf{I}$ is the symmetric inertia matrix of the spacecraft about the body-fixed reference frame. The diagonal terms of the inertia matrix are the principle moments of inertia of the spacecraft, while the off-diagonal terms are referred to as the cross products of inertia and arise when the body-fixed axis frame does not coincide with the principle axes of the spacecraft.

The rate of change of angular momentum is also important in dynamic model formulation. If there are external moments ($\mathbf{M}$) acting about the center of mass of the spacecraft, then the angular momentum rate of change with respect to a fixed reference frame ($o$) can be defined as:

$$\left[ \frac{d\mathbf{H}}{dt} \right]_o = \sum \mathbf{M_o} \tag{2.13}$$

This relationship along, with Eq.(2.11), is necessary to define the attitudinal motion of a spacecraft under applied moments.

## 2.4.2 Euler Moment Equations

The Euler moment equations are based on the law of conservation of angular momentum and used in the formulation of attitude motion. Eq.(2.14) may be expanded as follows:

$$\sum \mathbf{M_b} = \left[ \frac{d\mathbf{H}}{dt} \right]_b + \boldsymbol{\omega} \times \mathbf{H} \tag{2.14}$$

where the subscript $b$ refers to the body fixed axes of the spacecraft. By evaluating Eq.(2.14), the Euler moment equations for body rate dynamics may be defined as:

$$M_x = \dot{h}_x + \omega_x h_z - \omega_z h_y \qquad (2.15a)$$

$$M_y = \dot{h}_y + \omega_z h_x - \omega_x h_z \qquad (2.15b)$$

$$M_z = \dot{h}_z + \omega_x h_y - \omega_y h_x \qquad (2.15c)$$

Eqs.(2.15) assume that cross products of inertia exist in the inertia matrix. It should also be noted that the Euler moment equations are directly coupled with Eqs.(2.11) and that the last three states used in the dynamic equations of motion $(\dot{\omega}_x, \dot{\omega}_y, \dot{\omega}_z)$ arise in the differentiation of the angular momentum.

Simplifications of the Euler moment equations are often used in special situations in which valid assumptions can be made. By assuming that the principle axes of the spacecraft coincide with the body fixed reference frame, cross products of inertia are eliminated such that the Euler moment equations reduce to:

$$M_1 = I_1 \dot{\omega}_x + \omega_y \omega_z (I_3 - I_2) \qquad (2.16a)$$

$$M_2 = I_2 \dot{\omega}_y + \omega_x \omega_z (I_1 - I_3) \qquad (2.16b)$$

$$M_3 = I_3 \dot{\omega}_z + \omega_x \omega_y (I_2 - I_1) \qquad (2.16c)$$

Furthermore, by assuming that the spacecraft is axisymmetric ($I_1 = I_2$) and that there are no external torques acting on the system ($\mathbf{M} = 0$) the equations additionally reduce to:

$$\dot{\omega}_x + \lambda \omega_y = 0 \qquad (2.17a)$$

$$\dot{\omega}_y - \lambda \omega_x = 0 \qquad (2.17b)$$

where $\omega_z$ is a constant spin rate ($n$ rads/s) and $\lambda$ is a parameter defined as:

$$\lambda = (\frac{I_3 - I_1}{I_1})n \qquad (2.18)$$

Eq.(2.17) is used as a linear approximation of the Euler moment equations and simplifies analysis. It is shown later, that this approximation is usually insufficient in describing highly nonlinear spacecraft attitude dynamics for control and estimation design.

## 2.5 Flexible Spacecraft Dynamics

Flexible spacecraft dynamics must be considered when highly flexible spacecraft components have a significant effect on the overall response of the system under applied loads. To ensure that flexible dynamics do not affect the overall system response, it is usually desired that flexible modes of vibration be an order of magnitude greater then rigid body modes [5]. Highly flexible spacecraft components can effect sensor data, control commands, and physical characteristics such as moments of inertia and center of mass, all of which can cause a spacecraft to go unstable. Especially in applications that require deployment of instrumentation booms, flexibility effects and frequency modes can change drastically, requiring a more comprehensive dynamic analysis. Modeling and control of highly flexible structures is a popular area of research in the aerospace and structural field. However, this is beyond the scope of this research. Below, the simple methods of modal analysis are presented as they apply to this research.

## 2.6 Nutation

Nutation is an undesirable spacecraft effect that can cause inaccuracies in experimental measurements, excessive spacecraft oscillations or, in worse case scenarios, instability. Although the mathematical representation of nutation is not included in attitude models for this research, it is necessary to understand the physical nature of the effect in order to develop control and estimation techniques that are used to re-

ject nutation. For more a more comprehensive mathematical background in nutation dynamics the reader should reference [6] and [5].

Nutation is a rotational motion effect in which the spin axis is not aligned with the principle axis of the spacecraft, thus causing the principle axis to rotate about the angular momentum axis that is fixed in space. This resulting induced rotation about the remaining two spacecraft fixed axes is refereed to as nutation and can be induced by multiple physical effects such as fuel sloshing, mass imbalances, or cyclical external torques.

# CHAPTER 3

# FINITE ELEMENT ANALYSIS AND NUMERICAL METHODS

The finite element method has been used in the engineering field for the last 40 years. Since the development of the digital computer, much larger systems of equations involving high order matrix operations, once thought to be impractical to solve, were evaluated in minutes. With the digital computer, a new field of research in digital computation and numerical methods spawned. These new methods allow for highly complicated, nonlinear structures to be evaluated simply by user specification of material properties, boundary conditions and finite element properties.

R. W. Clough first introduced the phrase "Finite Element" in his 1960 paper "Finite Element Method in Plane Stress Analysis" [22]. The mathematical principals of finite element modeling can be traced back to the early 20th century with research done by famous mathematicians such as Lord Rayleigh and Walter Ritz [23]. Their research in particular provided a foundation upon which numerical methods were developed for eigenvalue analysis. It was in the 1940's when extensions of Rayleigh and Ritz's research in approximation of continuous differential equations were introduced by Richard Courant in his paper "Variational Methods for the Solution of Problems of Equilibrium and Vibrations". The Russian scientist Boris Galerkin was also pivotal in the early developments of FEA in his 1915 paper "Series Solution of Some Problems of Elastic Equilibrium of Rods and Plates". Since the recognition of the finite element method for structural dynamic problems in the 1960's, it has seen applica-

tions ranging from thermal analysis to providing a three dimensional understanding of electromagnetic fields.

The most common form of FEA is called the displacement-based finite element method. Spatial discretization results in a system of differential equations of motion adopted from [24] and defined as:

$$R = M\ddot{U} + C\dot{U} + KU \tag{3.1}$$

where the state variables $U = [U, V, W]^T$ represent nodal displacements in x,y,z directions of the body-fixed axes respectively. $M$, $C$, and $K$ are the element specific mass, damping and stiffness matrices, respectively, and $R$ is the time-dependent load vector. A more comprehensive mathematical description of the displacement-based finite element method can be found in [24] and [22]. From inspection of these equations it can be seen that in steady-state or statics applications, only stiffness effects are considered while dynamic problems include inertia and energy dissipation effects. In many situations it is difficult to quantify energy dissipation effects due to its dependence on frequency, and it is, thus, excluded from the system equations and constructed from experimental data when it is to be considered [24].

The following sections offer an introduction into the basic mathematics of the finite element method. Most of what is developed below is adapted from Bathe [24] and offers a very respected and comprehensive reference on finite element analysis and its applications. The reader should reference this source for a more in-depth and advanced understanding of finite element mathematics.

## 3.1   Discrete Systems

A fundamental problem that faces engineers in the analysis of complex systems is the highly nonlinear and complicated continuous differential equations that are

used to describe the physical response of a system. From a mathematical view, they offer a pure understanding of the physical system. However, in the analysis of these equations for engineering purposes, it can be a tedious and unmanageable task. It is only in very simple situations where exact solutions to differential equations can be obtained. For complex systems, it is necessary to reduce the continuous equations to a finite dimensional system of algebraic equations. In the analysis of these discrete equations, four steps can be followed in all instances as proposed in [24]:

**system idealization** - the continuous system is subdivided into a finite number of elements

**element equilibrium** - the equilibrium of each element is determined

**element assemblage** - the mathematical relationship is established between each element and then augmented into a set of algebraic equations that describe the state variables

**solution of response** - the set of simultaneous equations is solved for state variables and the response of each element is determined to gain an understanding of overall system

Three main situations in which discrete systems are analyzed involve steady-state problems, propagation problems and eigenvalue problems. Steady-state problems involve the determination of state variables that are not dependent on time. This is the most common application of FEA and can be utilized in the evaluation of deflection and bending stress gradients in structures under static loads, or steady-state temperature gradients in thermal systems. The scope of this research focuses on the application of finite element methods to dynamic systems.

The following sections will give a more in depth introduction to propagation and eigenvalue problems, and the procedures in which they are numerically solved.

## 3.2 Analysis of Dynamic Systems

Dynamic extensions of FEA, or propagation problems, arise from the need to understand how systems responsed under time variant loads. Unlike in steady-state or static problems, time dependent loads, such as a body's inertia, are included in the analysis. State variables are time dependent and their response under loads is determined through FEA of propagating systems. The numerical solution of these problems involves determining state variables at each time increment. The length of the time steps is defined by the analyst and can greatly effect the predicted overall response of the system. Several numerical techniques have been developed for solving these types of problems and are introduced in following sections.

The main assumption in steady-state and propagation problems is that the system responds in a unique manner under static or time-variant loads. The eigenvalue analysis computes various possible responses of a system under applied loads. Eigenvalue problems can be extended to both steady-state and dynamic problems. Under steady-state conditions, eigenvalue analysis is used to determine the stability of a system if it is perturbed about its equilibrium position. For dynamic systems, eigenvalue analysis (also referred to as modal analysis in dynamic instances) is utilized to determine the natural modes at which a system will oscillate. Natural modes are defined by the frequency at which they oscillate and their shape of vibration. The number of natural modes a system has is equal to the system's degree of freedom. In other words, if a continuous system is discretized and has $N$ degrees of freedom, the system will have $N$ natural modes [23]. This can be mathematically cumbersome in complicated systems and since the higher order modes of vibration converge to zero quickly, it is only the first modes of vibration that are of interest.

The mathematical basis of eigenvalue analysis is introduced as it applies to uniform beams.

### 3.2.1 Modal Analysis

The mathematical basis for modal analysis is adopted from Wei [25]. Although, this research focuses on a finite element approach to modal extraction, the assumption of a uniform bar with longitudinal vibration and control input being applied to $x = 0$ is used in the mathematical formulation of modal analysis. For an infinite number of vibrational modes, the transfer function relating control input $(u)$ to beam deflection $(y(x))$ in the Laplace domain is given as:

$$\frac{y(x,s)}{u(s)} = \frac{a_o}{s^2} + \sum_{i=1}^{\infty} \frac{a_i(x)}{s^2 + 2\zeta_i\omega_i s + \omega_i^2} \tag{3.2}$$

where $a_i(x) = 2\cos(i\pi x)$ for all modes of vibration $i = 1, ..., \infty$ and $\zeta_i$ is the modal damping parameter responsible for energy loss during oscillation from material elastic deformation.

Modal truncation is a process of reducing the infinite series expressed in Eq.(3.2) to a finite-dimensional model that can be useful in analyzing flexible structure modes and their overall contribution to the vibrational response. For modal truncation, the system is assumed to have the same damping ratio $\zeta$ for each , as well as an impulse input applied at $x = 0$. The corresponding vibrational response of the first $n$ influential modes is given as:

$$y(x,t) = a_o t + \sum_{i=1}^{n} \frac{a_i(x)}{\omega_i\sqrt{1-\zeta_i^2}} e^{-\zeta_i\omega_i t} \sin\sqrt{1-\zeta_i^2}\,\omega_i t \tag{3.3}$$

The modal gain mathematically describes the amplitude of the $i_{th}$ mode of vibration at time $t$ and location along the structure $x$ and is defined as:

$$g(x,t) = \frac{a_i(x)}{\omega_i\sqrt{1-\zeta_i^2}} e^{-\zeta_i\omega_i t} \tag{3.4}$$

It can be seen in the modal gain equation that higher order modes rapidly converge to zero and this is the reason why only the first $p$ modes are considered when analyzing the vibrational response. The modal gain also offers insight into the influence of each

mode on the overall system response. This can be useful in sensor and actuator placement as well as deciding discretization schemes for flexible modeling [26]. Most importantly, by understanding the dominate modes of a vibrational response, control and observer design can take into consideration these modes, as to not excite them during spacecraft operation.

Next, the numerical methods used for eigenvalue analysis and propagation of complex systems under applied forces will be presented.

## 3.3   Numerical Analysis of Propagating Systems

The following material is adopted from Logan [22] and Bathe [24] and should be referenced for a more in depth understanding of these complex mathematical tools.

As stated above, propagation problems involve dynamic systems in which the selected state variables change with time. Discretization allows for these continuous systems to be solved in reasonable time through numerical integration methods. Numerical methods have been introduced with the advancement of digital computers to discretize Eq.(3.1) and solve the state variables.

Most or all of the following techniques presented are available on commercial finite element software packages. Each technique has its own drawbacks ranging from computational demand to numerical instabilities, that cause inaccurate results. In all cases, each technique should be tested and compared to determine the most appropriate method for a given application.

### 3.3.1   Central Difference Integration

The most common numerical technique used in discrete dynamical systems is called direct integration. Essentially, direct integration conducts a static analysis at each time interval, however, inertia and damping effects are included. The central differ-

ence method is defined as (assuming damping effects are neglected):

$$U_{i-1} = U_i - \Delta t \dot{U}_i + \frac{(\Delta t)^2 \ddot{U}_i}{2} \tag{3.5a}$$

$$\ddot{U}_i = M^{-1}(R_i - K_i U_i) \tag{3.5b}$$

$$M U_{i+1} = (\Delta t)^2 R_i + [2M - (\Delta t)^2 K]U_i - M U_{i-1} \tag{3.5c}$$

where $i$ is the time increment defined for a certain time step $\Delta t$, $U_i = U(t)$ and $U_{i+1} = U(t + \Delta t)$. To begin this routine, initial conditions $U_o$, $\dot{U}_o$ and $\ddot{U}_o$ must be defined. Time steps are selected by the user with smaller steps resulting in greater accuracy. A method of selecting step size that ensures numerical stability is proposed by Bathe [24], which states:

$$\Delta t \leq \frac{3}{2\omega_{max}} \tag{3.6}$$

where $\omega_{max}$ is the structure's highest natural frequency which can be determined from multiple different eigenvalue evaluations. This is also referred to as the critical time step for central difference integration. If the time step for a given application is larger then the critical time step, the numerical analysis might become unstable, yielding worthless results.

### 3.3.2  Houbolt Method

The Houbolt method is similar to the central difference equations presented in Eq.(3.5). The governing equations of the Houbolt method are defined as [24]:

$$\ddot{U}_{t+\Delta t} = \frac{1}{2} \left[ 2U_{t+\Delta t} - 5U_t + 4U_{t-\Delta t} - U_{t-2\Delta t} \right] \tag{3.7a}$$

$$\dot{U}_{t+\Delta t} = \frac{1}{6\Delta t} \left[ 11U_{t+\Delta t} - 18U_t + 9U_{t-\Delta t} - 2U_{t-2Deltat} \right] \tag{3.7b}$$

In order to solve for the state variables at $t + \Delta t$, Eqs.(3.7) must be substituted into Eqs.(3.8).

$$M \ddot{U}_{t+\Delta t} + C \dot{U}_{t+\Delta t} + K U_{t+\Delta t} = R_{t+\Delta t} \tag{3.8}$$

The main disadvantage of the Houbolt method lies with its conditional stability, as with the central difference equation. If the size of the time step of the numerical analysis is not adequately small, the procedure will yield inaccurate results.

### 3.3.3 Newmark's Method

The Newmark, or also called Newmark-Beta, method is another numerical method used to solve dynamic equations. It is an extension of the central difference equations, however, the method is more robust to time step size selections. Although the derivation of Newmarks's equation are not presented below, the governing equations are provided to offer insight into the method by which finite element software packages arrive at solutions. For a complete derivation of Newmark's equations, one should refer to [24]. Newmark's equations are defined as:

$$\dot{\boldsymbol{U}}_{i+1} = \dot{\boldsymbol{U}}_i + (\Delta t) \left[ (1 - \gamma)\ddot{\boldsymbol{U}}_i + \gamma\ddot{\boldsymbol{U}}_{i+1} \right] \tag{3.9a}$$

$$\boldsymbol{U}_{i+1} = \boldsymbol{U}_i + (\Delta t)\dot{\boldsymbol{U}}_i + (\Delta t)^2 \left[ (\frac{1}{2} - \beta)\ddot{\boldsymbol{U}}_i + \beta\ddot{\boldsymbol{U}}_{i+1} \right] \tag{3.9b}$$

where $\beta$ and $\gamma$ are user-defined parameters. Typically, $\beta$ is chosen between 0 and 0.25 while $\gamma$ is usually selected at 0.5. It has been proven by Bathe [24] that if $\beta$ and $\gamma$ are selected at 0.16 and 0.5 respectively, Eqs.(3.9) reduce to the central difference equations. Also, unlike the central difference method where time steps must be chosen sufficiently small to guarantee numerical stability. Newmark's method remains stable for $\beta = 0.5$ and $\gamma = 0.25$. Finally, it has been shown that the numerical method yields the most accurate results when the time step is selected at 0.10 of the lowest natural frequency. It is for these reasons of numerical stability and an easily defined optimal time step that the Newmark method is ideal, especially in commercially available finite element software packages.

### 3.3.4 Numerical Analysis for Eigenvalue Problems

The numerical methods described in this section are adopted from the mathematical principal of these methods presented in Bathe [24]. Eigenvalue analysis, also called modal extraction, is a numerical evaluation that determines natural modes of vibration of a given dynamic system. The most basic eigenvalue problem to be solved in structural dynamics applications is defined as:

$$\boldsymbol{K}\phi = \lambda\boldsymbol{M}\phi \tag{3.10}$$

where the stiffness matrix is defined as $\boldsymbol{K}$ and mass matrix $\boldsymbol{M}$ while the natural modes of vibration are defined by natural frequencies $\lambda_i$ and eigenvectors $\phi_i$. For a system with $N$ degrees of freedom, then $\boldsymbol{K}, \boldsymbol{M} \epsilon \Re^{N \times N}$ and the system will have $N$ frequencies of vibrations and eigenvectors such that:

$$0 \leq \lambda_1 \leq \lambda_2 \leq \lambda_3 \leq ....... \leq \lambda_N \tag{3.11}$$

For a system that has been discretized in to many elements, it can be tedious to calculate all modes of vibration. As stated earlier, many higher order modes of vibration converge to zero quickly. In engineering applications, typically the 10 lowest natural frequencies are of interest. The demand to approximate the important modes of vibration for a large complicated system has lead to the development of several numerical techniques. An important property in modal analysis is that a body is fully constrained during the numerical procedures. In other words, if a mechanical body is allowed to rotate or translate in one or more degrees of freedom, the numerical algorithms are not able to compute all possible modes of vibration. This requirement makes modal extraction of bodies in motion nearly impossible.

There are three main approximation procedures that can be found in commercial software for eigenvalue analysis: static condensation, Rayleigh-Ritz, and Lanczos method. In the static condensation method, degrees of freedom that do not appear in

the global finite element matrices are eliminated. From here, the mass is lumped at specified degrees of freedom to ease the frequency calculations. This makes computation easy from Eq.(3.10), however accuracy is sacrificed. The Rayleigh-Ritz method utilizes basis vectors to determine the approximations of eigenvectors that span the basis vectors. Finally, the Lanczos method uses iteration algorithms that can calculate modes of vibration that have improved accuracy as a result of the iteration. To understand these methods and their complex mathematical development, the reader is referred to [24] for further detail.

# CHAPTER 4

# FINITE ELEMENT ANALYSIS RESULTS

The Finite Element Analysis phase of the MMS research involves multiple stages. In the first stage of the research a modal analysis is performed on the MMS axial booms using the MARC Mentat FEA software package. The goal behind the modal extraction is to confirm NASA boom natural frequencies of the two axial double probe (ADP) booms through two different simulation techniques that are described in the following sections. Along with acquiring natural modes of vibration and mode shapes, a modal gain analysis is conducted to assist NASA in mathematical model development of flexible booms. Equations based on the paper written by Erik Stoneking [26] at the NASA Goddard Research Center are to be developed for implementation into MATLAB simulations in future research. This will allow for an understanding of fully flexible boom dynamics under orbital and attitude maneuvers. Finally, a fully elastic model of the MMS spacecraft with axial booms is developed using finite elements. From this model, stresses at boom joints can be determined from a rotating spacecraft translating through space. Also this will give insight into the dynamic elastic behavior of the spacecraft under thruster forces.

The following chapters will present results of the finite element analysis performed on the NASA MMS.

## 4.1 Modal Analysis

The modal extraction conducted on the ADP booms is evaluated in two different techniques. The first method involves an eigenvalue analysis as presented in Chapter 3 for a fully constrained body. In this analysis the first ten natural frequencies of vibration are calculated along with graphical descriptions of their mode shapes. These results are then compared with natural frequencies obtained from a dynamic analysis. In this type of simulation, booms are attached to a rigid spacecraft body that is acted on by external forces to emulate thrusters. The spacecraft body is allowed to translate through space, and the resulting boom vibrations are analyzed. It is vital in determining the relationship between methods, so that in a fully dynamic case, any frequencies of vibration that are observed are accurate natural modes.

The booms are modeled as a single rigid element with all elasticity stored in a spring at the origin. Figure 4-1 illustrates the rigid boom model. Rotational springs about all three axis are implemented with a specified stiffness provided by NASA engineers. Combined with a constraint on all three translational degrees of freedom, the model is fully constrained and the analysis is able to converge. The rigid boom with elastic spring assumption aided in natural frequency calculation and finite element methods are used in confirmation of these natural frequencies. An accurate knowledge of these frequencies is essential in spacecraft design, especially in orbit and attitude control. If the thrusters, used in actuation, fire at similar frequencies to that of the booms, dominate modes will be excited undesirably.

### 4.1.1 Modal Extraction

The first part of the modal extraction phase involved model development. Table 4.1 illustrates the model parameters that are used to define the ADP boom. All values have been supplied by NASA engineers.
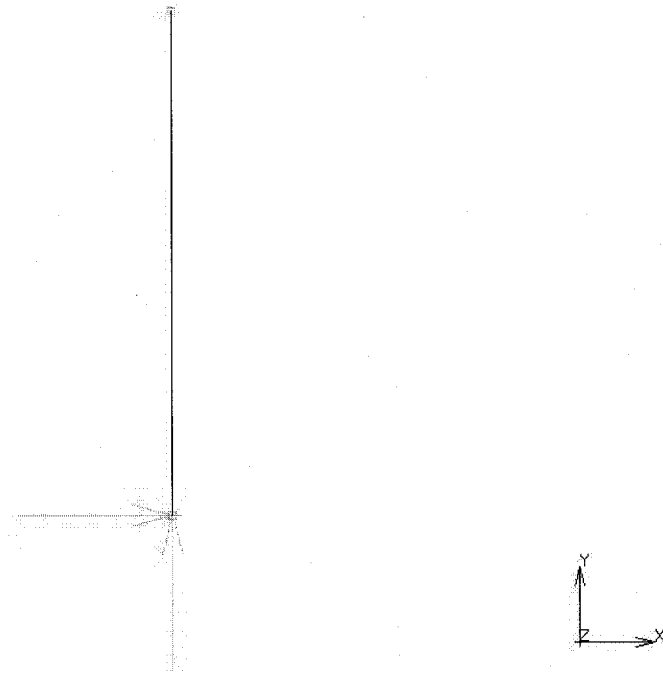
Figure 4-1: Rigid Boom Finite Element Model

| Model Parameters | Values |
|---|---|
| Moments of Inertia $(kg - m^2)$ | $I_x = 0.00014,\ I_y = 13.978$ |
| Cross Sectional Area $(m^2)$ | A=0.0006 |
| Elastic Modulus (Pa) | E=1e+14 |
| Material Density $(kg/m^2)$ | $\rho = 181.57$ |

Table 4.1: Modal Extraction Model Parameters

| $K_p(x,y)(N/m)$ | Modal Extraction $\omega_n$ (x,y) Hz | NASA $\omega_n$ (x,y) Hz |
|---|---|---|
| 49.7432 | 0.151 | 0.15 |
| 22.1081 | 0.1007 | 0.10 |
| 28.2298, 39.4973 | 0.1138, 0.1346 | 0.113, 0.134 |
| 88.4323 | 0.2014 | 0.20 |

Table 4.2: Modal Extraction Results for Rigid Boom

A single beam element is used to create the simplified model, with rotational springs constraining the x and y rotations, while the z rotation as well as x,y and z translations had zero displacement constraints. Multiple different spring stiffness values are simulated. Figure 4-1 illustrates the single beam element used in the modal extraction of a rigid body.

Along with defining a model, many simulation parameters are selected for numerical analysis. Multiple different numerical techniques are available for modal extraction in the MARC Mentat software. The Lanczos method is used for modal shape and frequency determination.

Simulation results are presented in Table 4.2 along with NASA results as comparison. It can be seen that the natural frequency $\omega_n$, of the first natural mode of vibration, is verified through modal extraction techniques for all spring stiffness values.

### 4.1.2 Dynamic Transient

The dynamic transient analysis option in MARC Mentat allows for time dependent simulations. For this type of simulation, forces are applied to the model and the simulation produces time dependent results. This method allows for a full dynamic understanding of stresses and deflections during maneuvers. Thruster loads will be
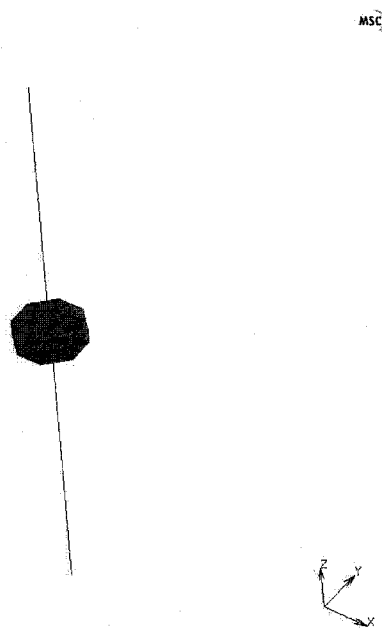
Figure 4-2: Finite Element Model of Satellite with Rigid Booms

applied to the rotating spacecraft with fully elastic booms to simulate orbital transfers.

Before a fully dynamic model is performed, it is necessary to prove that vibration data obtained from these simulations is valid. Ultimately, frequencies of vibration of the axial booms are to be found, and since modal extraction does not allow for vibrational analysis of a partially constrained body, it is in dynamic transient simulations where this data is found.

The simulation model consists of a rigid spacecraft body with attached axial booms. These booms are attached through rotational springs about the x and y axis, and constrained in x, y and z translations relative to the spacecraft body. Figure 4-2 illustrates the spacecraft body and rigid axial booms. The model undergoes translational motion due to four thrusters that exert 10 Newtons of thrust each as shown in Figure 4-3. Since the spacecraft is not rotating about its z-axis, only thrusters acting in the positive x-axis are used to induce translation.

Table 4.3 show the model parameters for the satellite booms. Each boom is 12
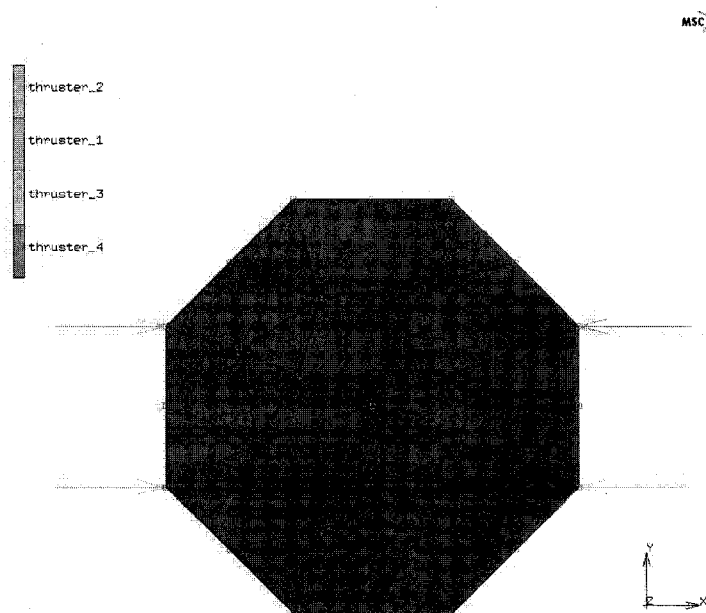
Figure 4-3: Satellite Thruster Locations

meters in length while the spacecraft body is an octagon shape with sides equal to 1 meter and depth of 0.5 meters. For non elastic analysis, booms are constructed of a single elastic beam finite element with a high elastic modulus 1e+14 Pa. In simulations when elastic motion is investigated, each axial boom is subdivided into 12 elastic beam elements. For the spacecraft body, a geometry is constructed using MARC, followed by a mesh generation using tetrahedral elements. Again, the spacecraft body is given a high elastic modulus to make the body rigid and ensure that minimal deformation occurs under thruster loads.

The dynamic transient simulation runs for 100 seconds with 500 time steps ($\Delta t = 0.2s$). A full Newton-Raphson iteration technique is used, and two different integration methods are investigated. In both integration techniques, the large strain option of the finite element software is selected to allow for nonlinear analysis to take place.

The first integration method tested is the Houbolt numerical analysis. From in-

| Model Parameters | Values |
|---|---|
| Moments of Inertia $(kg - m^2)$ | $I_x = 0.00014$, $I_y = 13.978$ |
| Cross Sectional Area $(m^2)$ | A=0.0006 |
| Elastic Modulus (Pa) | E=1e+14 |
| Material Density $(kg/m^2)$ | $\rho = 181.57$ |

Table 4.3: Dynamic Transient Parameters

| $K_p(x,y)(N/m)$ | Modal Extraction $\omega_n$ (x,y) Hz | NASA $\omega_n$ (x,y) Hz |
|---|---|---|
| 49.7432 | 0.1511 | 0.15 |
| 22.1081 | 0.1007 | 0.10 |
| 28.2298, 39.4973 | 0.1139, 0.1345 | 0.113, 0.134 |
| 88.4323 | 0.2013 | 0.20 |

Table 4.4: Dynamic Transient Results for Rigid Boom Vibrations

vestigation of boom tip displacements, it is determined that the Houbolt integration method causes a numerical inaccuracy. There are no damping parameters selected in the analysis, yet tip displacement amplitude results suggests that energy dissipation occurs. Despite increasing numerical increments from 500 to 2000 (decay decreased from 17% to 1.4%) and investigating various iteration techniques, the numerical inaccuracy could not be eliminated.

The implementation of the Newmark-Beta technique through the MSC software indicates that numerical damping is eliminated. Numerical parameters included $\beta = 0.5$ and $\gamma = 0.25$ which are typical values of this type of analysis that guarantee numerical stability according to [24]. Results show that the "numerical damping" inaccuracy that causes unnatural results is eliminated through the use of the Newmark-Beta integration technique. Also, with an x and y rotational spring of stiffness $K_p = 49.7432$

N/m the first natural frequency is consistent with the modal extraction method and NASA results. This leads to the encouraging conclusion that the dynamic transient method of vibration analysis for unconstrained bodies is consistent with other vibration analysis techniques. The drawback of the dynamic transient analysis, is that only the lowest frequency of vibration can be determined and higher order frequencies remain unknown. Table 4.4 lists the remaining frequencies of vibrations for various spring stiffness values.

## 4.2    Satellite Dynamic Response

The final step in the finite element analysis, is a dynamic transient response. Utilizing the Newmark-Beta integration technique, the model illustrated in Figure 4-2 is given an initial rotational velocity about its z-axis, and then thrusters will impart a force to induce translation. Four thruster firing schemes are investigated:

- One pair of thrusters will fire every $180^o$ of rotation (firing frequency of 0.05 Hz) for a length of 1 second

- One pair of thrusters will fire every $180^o$ of rotation (firing frequency of 0.05 Hz) for a length of 2 seconds

- One pair of thrusters will fire every $360^o$ of rotation (firing frequency of 0.10 Hz) for a length of 1 seconds

- One pair of thrusters will fire every $360^o$ of rotation (firing frequency of 0.10 Hz) for a length of 2 seconds

Since it is yet to be determined exactly how the MMS will function during its operational stages, these results will help in determining optimal operation. From

these simulations, reaction forces at beam connections to the spacecraft can be determined, and with the implementation of fully elastic beams, an understanding of flexible dynamics can be obtained.

The implementation of the initial spacecraft rotation is attempted through equal and opposite thruster firings that create a torque about the z-axis of the spacecraft, and thus inducing rotational motion. Also, initial conditions are given to the spacecraft model such that the z-axis would rotate at 0.3 rad/s. In both instances it is immediately determined that numerical instabilities are causing inaccurate results. The software is not effectively performing coordinate transformations at roughly 90 degrees of rotation. If certain simulation parameters are selected to allow for this rotation, the model unnaturally expands at a rapid rate. Much consultation with MSC user support engineers yielded in minimal progress in overcoming this numerical stability. This type of numerical instability can occur in many applications such as collision analysis when rotational motion is induced and coordinate transformation cannot occur. It is my opinion that this topic in itself is of much interest and worthy of future research for its implications on many dynamic transient analysis applications.

# CHAPTER 5

# ATTITUDE ESTIMATION AND CONTROL METHODS

Attitude control is the process by which actuators are used in producing an external force or torque on a spacecraft to maintain a desired attitude or to change the attitude of a spacecraft. Attitude stabilization is the process by which a spacecraft must maintain a desired attitude with respect to a fixed reference frame or inertial reference frame. Attitude maneuvers usually require knowledge of the current spacecraft orientation in order to effectively change attitude. In either case, attitude sensors are used for feedback of state information. The difference between desired and actual orientations are then used in a control process to activate actuators that impart desired torques or forces on the system to acquire and maintain desired spacecraft attitude.

Attitude control systems may be classified into two common types: active control and passive control. Active control uses discrete-time measurements of spacecraft states, such as attitude or body rate information, in order to control a spacecraft's attitude. Actuators such as gas jets, momentum wheels and magnetic torque rods are used to control the spacecraft, so as to maintain the tracking error to within desired limits (usually as close to zero as possible). Passive control, while often used in conjunction with active control, uses the spin of a spacecraft to maintain a constant momentum vector to keep the satellite spinning at a desired attitude. Since there are many unknown disturbance torques that can act on a spacecraft, the use of active control to maintain the orientation of the spin vector is usually necessary. Al-

though the correct selection of actuators and sensors is vital to a successful spacecraft application, it is the control process that must be designed to adequately integrate sensor and actuator systems with the overall spacecraft. Optimal linear and nonlinear algorithms, sliding mode control, adaptive and hybrid algorithms are examples of techniques that are used for attitude control.

Accurate knowledge of real time spacecraft dynamics is a vital component of ensuring that the attitude control system will perform sufficiently. In many spacecraft applications, sensor data is corrupted by significant levels of noise, unknown disturbances, and/or parameter uncertainties. Also, with the need to reduce spacecraft costs and weight, some sensors are excluded altogether, making attitude control even more difficult to satisfy given design requirements. Attitude state observers use nonlinear system dynamics with available sensor data to obtain state estimates. As with control systems, feedback is used to generate an error signal between estimated measurement output and actual sensor data. A dynamic estimation process is used to minimize this output measurement error and, thereby, minimize the state estimate errors. The Extended Kalman Filter (EKF) and Sliding Mode Observer (SMO) are two examples of such nonlinear state estimation techniques.

Control and estimation algorithm selection is mainly a trade off study between different system performance characteristics. In many applications it is desirable to explore multiple techniques to determine the most effective method for given design specifications. In this chapter, a mathematical background of linear and nonlinear control and estimation techniques are briefly introduced for their use in the NASA MMS mission.

## 5.1 Models

For a general representation of spacecraft state dynamics and outputs, the following form is used:

$$\dot{\boldsymbol{x}}(t) = \boldsymbol{f}(\boldsymbol{x}(t), \boldsymbol{u}(t), t) + \boldsymbol{w}(t) \tag{5.1a}$$

$$\boldsymbol{y} = \boldsymbol{h}(\boldsymbol{x}(t)) + \boldsymbol{z}(t) \tag{5.1b}$$

where $\boldsymbol{f}(\boldsymbol{x}(t), \boldsymbol{u}(t), t) \, \epsilon \, \Re^n$ represents the nonlinear equations of motion and $\boldsymbol{h}(\boldsymbol{x}(t)) \, \epsilon \, \Re^m$ is the nonlinear measurement model. The spacecraft dynamics are corrupted by process noise consisting of parameter uncertainty and unknown disturbances which can be embedded in $\boldsymbol{f}(\boldsymbol{x}(t), t)$ and/or lumped in $\boldsymbol{w}(t) \, \epsilon \, \Re^n$. Also, the measurement vector $\boldsymbol{y} \, \epsilon \, \Re^m$ is corrupted by Gaussian white measurement noise $\boldsymbol{z} \, \epsilon \, \Re^m$. The vector of known inputs is shown as $\boldsymbol{u}(t) \, \epsilon \, \Re^p$. The superscripts of $n$, $m$, and $p$ represent the number of states, outputs and inputs, respectively.

When a time-invariant system is linearized, it can be expressed as a set of matrices defined as:

$$\dot{\boldsymbol{x}} = A\boldsymbol{x} + B\boldsymbol{u} \tag{5.2a}$$

$$\boldsymbol{y} = C\boldsymbol{x} \tag{5.2b}$$

where $A$ and $B$ are state matrices and $C$ is the matrix that relates the output $\boldsymbol{y} \, \epsilon \, \Re^m$ to system states. This linear time-invariant (LTI) system is a common representation of systems when nonlinear dynamics are minimal. A common analysis of linear systems is their stability, which is guaranteed in an open-loop system if all eigenvalues have negative real parts. There are $n$ eigenvalues, $\lambda_i$, for a system with $n$ states such that:

$$|A - I\lambda| = 0 \tag{5.3}$$

For linear observers and controllers, eigenvalue determination varies slightly. However, all eigenvalues must always have negative real parts to help avoid instability.

## 5.2 Control Methods

Different control methods are evaluated in this research to determine the most effective and practical control process for the MMS application. Linear control with optimal gain selection is introduced, followed by a Sliding Mode Control (SMC).

### 5.2.1 Linear Optimal Control

Linear control is the simplest form of feedback control design. For an LTI system described in Eqs. (5.2a) a feedback gain is used to adjust the system input such that:

$$u = -Kx \tag{5.4}$$

where $K \epsilon \Re^{mxn}$ is a constant feedback gain matrix. Changing the feedback gain matrix affects the closed loop eigenvalues which all must have negative real parts according to:

$$|(A - GK) - I\lambda| = 0 \tag{5.5}$$

The feedback gains are chosen according to the desired location of eigenvalues to obtain the specified system characteristics. Gain selection and tuning is an iterative process that requires multiple simulations and reevaluation. Although it has proven effective for simplified systems, in higher order systems with multiple inputs and outputs, it can be a daunting and suboptimal approach.

Optimal control attempts to select feedback gains that produce an optimal input to force the system along a desired trajectory while minimizing a performance index on the system response. The most common form of optimal control is the Linear Quadratic Regulator (LQR), based on a LTI system as in Eq. (5.2a) which selects feedback gains while minimizing the performance index defined as:

$$J(t_o, t_f) = \frac{1}{2} \int x^T Q x + u^T R u \, dt + P\left[x\left(t_f\right), t_f\right] \tag{5.6}$$

where matrices $Q \epsilon \Re R^{n \times n}$ and $R \epsilon \Re R^{m \times m}$ are symmetric, positive semi-definite time, invariant performance matrices based on the states and inputs respectively. Eq. (5.6) also contains a penalty on the final time expressed by $P[x(t_f), t_f]$ which is a function of the states at the final time $t_f$. The ultimate goal is to determine an optimal $u$ such that Eq. (5.6) is satisfied. In order to solve this optimization problem, the Hamiltonian is introduced to develop state and costate equations which result in the following equations that define the optimal $u$: (for more background on optimization techniques refer to [27]).

$$u = -Kx \qquad (5.7a)$$

$$K = R^{-1}B^T S \qquad (5.7b)$$

$$-\dot{S} = A^T S + SA - SBR^{-1}B^T S + Q \qquad (5.7c)$$

where $S$ is an unknown function introduced from the state and costate equations during optimization and Eq. (5.7c) is referred to as the Riccati equation. The Ricatti equation is solved in reverse time starting at $t_f$ and can be found from computer routines common to most simulation packages. The optimal gain $K$ is the important outcome of these equations, since Eq. (5.7a) holds true for all linear feedback control systems. By selecting the diagonal terms of $Q$ and $R$ based on system requirements, the optimal gain can be determined through the Ricatti equation. Although this technique requires iterations of weighting factors, simulations, and re-evaluation to acquire a desired system response, for high order systems, the number of design parameters to be selected are considerably reduced compared to gain tuning if only considering diagonal weight elements.

### 5.2.2 Sliding Mode Control

The Sliding Mode Control (SMC) is a variable structure, nonlinear controller that uses sliding surfaces to force control error trajectoies to zero. The SMC is simliar to

the Sliding Mode Observer used in estimation problems and explored in this thesis. The mathematical formulation of the SMC is adopted from multiple sources and for a more comprehensive understanding of sliding mode phenomena the reader is referred to [16] and [1] .

For a given nonlinear system:

$$\dot{x}(t) = f(x(t), t) + Bu(t) \tag{5.8}$$

where for a $n^{th}$ order system the system states are described by $x \epsilon \Re R^n$ through non-linear relationships $f(x, t)$ with inputs $u \epsilon \Re R^m$ and $B \epsilon \Re R^{n \times m}$. The same nonlinear system, with a feedback SMC is defined as:

$$\dot{x} = f(x(t), t) + H\tilde{x} + K\mathbf{1}_s \tag{5.9}$$

where $\tilde{x} = x - x_{des}$, is the control error between actual states and desired states $x_{des}$. The constant feedback gains $H^{n \times m}$ and $K^{n \times p}$, (where $p$ is the number of sliding surfaces) are determined through design iteration. The switching function can be of the saturation or signum form or any such type of function. Throughout this research the saturation function is used to avoid chattering of the error trajectory along the sliding surface such that:

$$\mathbf{1}_s = sat\left(\frac{s}{\rho}\right) \tag{5.10}$$

where $s$ is from 1 to $n$ sliding surfaces. These sliding surfaces are all functions of the control error and, in most cases, involve the derivative, integral and/or summation of the error. The boundary layer, $\rho$, is another design parameter that affects error trajectory chattering as well as convergency of the error to the sliding surface [1].

In designing an SMC, feedback gains, sliding surfaces, and boundary layers must be selected. As with linear feedback control, gain tuning is an iterative and time consuming process that continues to quickly increase in complexity as the system order increases.

## 5.3 Estimation Techniques

As with control techniques, linear and nonlinear methods are available depending on system complexity. In this research, the most basic estimation techniques are first tested for effectiveness, and then more complex nonlinear methods are explored. The following sections introduce linear estimation techniques, followed by the nonlinear EKF and SMO techniques.

### 5.3.1 Linear Observers

For a linear time invariant system, as described in Eq.(5.2a), a linear estimation of all states is defined as follows:

$$\dot{\hat{x}} = A\hat{x} + Bu + L(y - C\hat{x}) \tag{5.11a}$$

$$\hat{y} = C\hat{x} \tag{5.11b}$$

where the estimated state vector is $\hat{x}$ and the feedback observer gain, also called the Luenberger gain, is $L \in \Re R^{nxm}$ where $m$ represents the number of measurements. The Luenberger gain, as with linear control gains, are implemented in order to drive an error signal to zero. In the case of linear observers the error signal is defined as $\tilde{y} = y - \hat{y}$ where $\hat{y}$ is the estimated ouput. The Luenberger gain is designed such that the closed loop eigenvalues have negative real parts (such that $|A - LC| \leq 0$) for system stability [28].

Another similarity with feedback control is the optimal selection of the feedback gains. This is referred to as the Kalman filter, and uses $Q$ and $R$ weight matrices to solve for the optimal gains through an error propagation equation, similar to the Ricatti equation. The $Q$ matrix puts a weight on process noise such as those caused by parametric uncertainty and unknown disturbances, while the $R$ matrix weights the measurements corrupted with noise. The linear time-invariant Kalman filter

equations are adopted from [28] and are defined as follows:

$$\dot{P}(t) = AP(t) + P(t)A^T + BQB^T - LRL^T RL^T \qquad (5.12a)$$

$$L = PC^T R^{-1} \qquad (5.12b)$$

Eq.5.12a is known as the Ricatti equation or error covariance propagation and is solved through iteration techniques.

As the Luenberger gain increases, the bandwidth of the Kalman filter increases, thus placing bias towards the measurements, rather then the model. Inversely, if the Luenberger gain decreases, so does the filter bandwidth, which requires the observer to rely more on system models rather then noisy measurement data.

The Kalman filter has been proven to be highly effective estimation technique, especially when it comes to filtering measurement noise. The nonlinear extensions of the Kalman filter are reviewed below, along with the Sliding Mode Observer, as alternatives to state estimation when systems are too complex to be expressed as LTI models.

## 5.3.2  Extended Kalman Filter

In many applications, system dynamics can be highly nonlinear and in most cases, linear observers are insufficient in estimating nonlinear states.

When using the Kalman filter, nonlinear system equations in the form of Eqs. (5.1) are linearized off-line about a predetermined state vector and the Luenberger gain is then calculated. The Extended Kalman Filter (EKF) involves updating the linearized system and linearized measurement model at each estimation step. These linearizations, or Jacobian matrices, are updated with each state estimate vector, rather then off-line with predetermined equilibrium points as with the linear Kalman filter. This linearized update makes the EKF more effective for systems with highly nonlinear dynamics (for the formulation below, the measurement model is assumed

linear). For a given nonlinear system the state estimation model is defined as (The reader is referred to [28] for further mathematical background on the EKF):

$$\dot{\hat{x}}(t) = \mathbf{f}(\hat{\mathbf{x}}(t), t) + K(t)[y(t) - h(\hat{\mathbf{x}}(t), t)] \tag{5.13}$$

where $y(t) = h(\mathbf{x}(t), t) + z(t)$ is sensor outputs $(h(\mathbf{x}(t), t))$ and measurement noise $(v(t))$.

The gain matrix $(K(t))$ calculation begins with propagating the estimation error covariance matrix equation given by:

$$\dot{\mathbf{P}}(t) = F(\hat{\mathbf{x}}(t), t)P(t) + P(t)F^T(\hat{\mathbf{x}}(t), t) + Q(t) - P(t)H^T R^{-1}(t)HP(t) \tag{5.14}$$

where the linearization of the nonlinear system model about each estimate is given by:

$$F(\hat{\mathbf{x}}(t), t) = \frac{\partial \mathbf{f}(\mathbf{x}(t), t)}{\partial \mathbf{x}(t)} \big|_{\mathbf{x}(t) = \hat{\mathbf{x}}, (t)} \tag{5.15}$$

and $Q(t)$ and $R(t)$ are weight matrices selected based on process noise and measurement noise respectively. The gain matrix is calculated by:

$$K(t) = P(t)H^T R^{-1}(t) \tag{5.16}$$

The error covariance equation, Eq. (5.14), and state matrix are then updated using the gain matrix and measurement error.

The EKF offers exceptional results when it comes to measurement noise rejection for highly nonlinear system models. However, the inability to guarantee closed loop system stability, as with the linear Kalman filter, is one of the drawbacks of the EKF. Also, since the calculation of the gain matrix is dependent upon the Jacobian of the nonlinear system equations, a highly accurate system model is necessary and, thus, makes the EKF less robust to parametric or modeling uncertainties. Finally, the evaluation of complex matrix operations such as inverses in Eq. (5.14) that must be calculated at each time step, make the EKF less desirable for applications with strict computational constraints.

### 5.3.3 Sliding Mode Observer

The Sliding Mode Observer is another nonlinear state estimation technique. Unlike the EKF, the SMO requires no linearization about any operating points during estimation. This makes the technique desirable in that the state equations are not being simplified in order to estimate states.

The SMO is very similar to the SMC presented in Section 4.2.2. Like the SMC, the SMO also utilizes a switching function and sliding surfaces to force the error trajectory to zero. For SMO development the observer dynamics is a function of estimated states, $\hat{x}$, and is defined as:

$$\dot{\hat{x}} = \hat{f}(\hat{x}(t), t) + B\hat{u}(t) + H\tilde{z} + K\mathbf{1}_s \qquad (5.17a)$$

$$\hat{z} = C\hat{x} \qquad (5.17b)$$

where the estimation error signal is defined as $\tilde{z} = z - \hat{z}$. Gain matrices $H \epsilon \Re^{n \times m}$ and $K \epsilon \Re^{n \times p}$ are selected through design iteration where $n$, $m$ and $p$ represent the number of states, measurements and sliding surfaces, respectively. The switching function, as defined in the SMC, is a saturation function such that:

$$\mathbf{1}_s = sat\left(\frac{s}{\rho}\right) \qquad (5.18)$$

As with the SMC, the number of sliding surfaces and how they are defined is part of the development process. The boundary layer and gain matrices are also defined through design and iteration.

For a more complete development of Sliding Mode Observers and Nonlinear Systems the reader is referred to [16] and [17].

# CHAPTER 6

# ATTITUDE ESTIMATION RESULTS

The first step in satellite nutation rejection and attitude control is ensuring that there is accurate real time information of the satellite states. This chapter presents three different designs for satellite body rate estimation assuming that only attitude measurements are available. The design is based on an Euler angle and Euler moment formulation of the dynamic equations of motion, which are then corrupted with parameter uncertainty, measurement noise, and satellite imbalances. In each case, all states are estimated, while the body rates are extracted for nutation control and Euler angles $\psi$ and $\theta$ for attitude control.

Attitude differentiation involves the differentiation and filtering of raw attitude measurement data for obtaining satellite body rate data. Although this is the simplest form of body rate determination, it is highly sensitive to increases in measurement noise as well as time delays due to low-pass filter bandwidth [1]. It is because of these findings that attitude differentiation is not considered in this research. A simple linearized Kalman filter, as introduced in Chapter 5, is first implemented on this highly nonlinear system to determine body rate estimation effectiveness. Upon analysis of the linear estimation results, the Extended Kalman Filter is used. Finally, the Sliding Mode Observer is implemented and compared with the linear Kalman Filter and the EKF in order to chose the most effective estimation technique, which is essential for effective attitude and nutation control.

Previous research on attitude estimation without the use of gyroscopic instruments has already been preformed by [13] and [14] with a recent study focusing on Euler

angle and quaternion representations of attitude, while investigating the effectiveness of the SMO for full state estimation [1]. While all of these studies offer insight into the research presented in this thesis, there is no existing development of a complete observer-based control system for particular use in the NASA MMS mission. It is in the implementation of the estimated states in the feedback control system and the overall system effectiveness to reject spin nutation that the estimation techniques are evaluated. Furthermore, flexible structure consideration and analysis provides the foundation for research in the area of full-state attitude and orbit estimation-based control of flexible structures as it applies to the NASA MMS mission.

## 6.1   Satellite Dynamic Equations of Motion

As stated above, Euler angle kinematics and Euler moment equations are used to formulate dynamics equation of motion to emulate spacecraft attitude motion while in orbit. A 3-2-1 Euler rotation sequence, as presented in Chapter 2, coupled with Euler moment equations, assuming no cross products of inertia is defined as:

$$
\boldsymbol{f}(\boldsymbol{x}(t), t) =
\begin{bmatrix}
\omega_x + (\omega_z \cos \psi + \omega_y \sin \psi) \tan \theta \\
\omega_y \cos \psi - \omega_z \sin \psi \\
(\omega_z \cos \psi + \omega_y \sin \psi) \sec \theta \\
((I_y - I_z)/I_x) \omega_y \omega_z \\
((I_z - I_x)/I_y) \omega_x \omega_z \\
((I_x - I_y)/I_z) \omega_x \omega_y
\end{bmatrix}
\tag{6.1}
$$

where $\dot{\boldsymbol{x}} = \boldsymbol{f}(\boldsymbol{x}(t), t)$ and the vector of states is $\boldsymbol{x}(t) = [\psi, \theta, \phi, \omega_x, \omega_y, \omega_z]^T$. Eq.(6.1) is used for nonlinear estimation models and do not take into account cross products of inertia, unknown disturbances, or external torques. For dynamic equations of motion in which external torques and cross products of inertia are considered, the following

decoupled equations are used to find $\dot{\omega}_x, \dot{\omega}_y, \dot{\omega}_z$ in terms of $\omega_x, \omega_y, \omega_z$ and $h_x, h_y, h_z$:

$$I_x\dot{\omega}_x - I_{xy}\dot{\omega}_y - I_{xz}\dot{\omega}_z = M_x - \omega_y h_z + \omega_z h_y \tag{6.2a}$$

$$-I_{xy}\dot{\omega}_x + I_y\dot{\omega}_y - I_{yz}\dot{\omega}_z = M_y - \omega_z h_x + \omega_x h_z \tag{6.2b}$$

$$-I_{xz}\dot{\omega}_x - I_{yz}\dot{\omega}_y + I_z\dot{\omega}_z = M_z - \omega_x h_y + \omega_y h_x \tag{6.2c}$$

where:

$$\begin{bmatrix} h_x \\ h_y \\ h_z \end{bmatrix} = \begin{bmatrix} I_{xx} & -I_{xy} & -I_{xz} \\ -I_{yx} & I_{yy} & -I_{yz} \\ -I_{zx} & -I_{zy} & I_{zz} \end{bmatrix} \begin{bmatrix} \omega_x \\ \omega_y \\ \omega_z \end{bmatrix} \tag{6.3}$$

as described in Chapter 5. It should be noted that for consideration of cross products of inertia and external torques, the first three state equations of Eq. (6.1) remain the same since Eqs. (6.2) are not dependent on states $\psi, \theta, \phi$

Eqs. (6.1) can be linearized assuming the spacecraft is axisymmetric and has no applied torques. These assumptions allow for a reduction of the state vector to $\dot{x} = [\omega_x, \omega_y, \omega_z]^T$ [6]. The linearized equations are expressed in state-space form as follows:

$$\begin{bmatrix} \dot{\omega}_x \\ \dot{\omega}_y \end{bmatrix} = \begin{bmatrix} 0 & (\frac{I_y - I_z}{I_x})n \\ -(\frac{I_z - I_x}{I_y})n & 0 \end{bmatrix} \begin{bmatrix} \omega_x \\ \omega_y \end{bmatrix} + \begin{bmatrix} 1 & 0 \\ 0 & 1 \end{bmatrix} \begin{bmatrix} u_1 \\ u_2 \end{bmatrix} \tag{6.4}$$

where $\omega_z$ spins at a constant rate $n$ and $u_1, u_2$ are thrust inputs.

## 6.2 Linearized Observer

A linear observer is designed based on the dynamics of Eq.(6.4) to estimate body rates $\omega_x, \omega_y$ of the nonlinear Eqs.(6.1). The linear observer is used to investigate the effectiveness of using a simplified observer model, to estimate states of a highly nonlinear system. It should be noted that the actual dynamics of the system remain nonlinear (although they ignore cross products of inertia), and it is only the system

|  | Actual System | Observer |
|---|---|---|
| I.C.: $\psi, \theta, \phi$ $(rad)$ | 0, 0, 0 | 0,0,0 |
| I.C.: $\omega_x, \omega_y, \omega_z$ $(rad/s)$ | 0.01, 0.01, 0.3 | 0,0,0 |
| Inertia Matrix $(kg \cdot m^2)$ | $\begin{bmatrix} 8402.64 & 0 & 0 \\ 0 & 8411.97 & 0 \\ 0 & 0 & 16414.66 \end{bmatrix}$ | $\begin{bmatrix} 8402.64 & 0 & 0 \\ 0 & 8411.97 & 0 \\ 0 & 0 & 16414.66 \end{bmatrix}$ |

Table 6.1: Simulation Parameters for Linear Observer

model used for observer design that is linearized such that the Kalman filter approach can be investigated.

The linear observer based on Eqs. (6.4) is assumed to be rotating at a constant spin rate $n = 0.3$ rad/s with system and observer parameters listed in Table 6.1.

The output measurements of the actual system $(\psi, \theta, \phi)$ are corrupted with a zero-mean gaussian white noise of $\pm 0.03$ rad.

The linear Kalman filter is of the following form:

$$\dot{\hat{x}} = A\hat{x} + L(y - \hat{y}) \tag{6.5a}$$

$$\hat{y} = C\hat{x} \tag{6.5b}$$

where the observer state matrix $A$ is defined as:

$$A = \begin{bmatrix} 0 & (\frac{I_y - I_z}{I_x})n \\ -(\frac{I_z - I_x}{I_y})n & 0 \end{bmatrix} \tag{6.6}$$

and the system output matrix $C = [I_{3 \times 3} \quad 0_{3 \times 3}]$. The Kalman gain $L$ is found through minimizing a cost function, by selecting non-zero diagonal weighting matrices $Q \epsilon \Re^{6 \times 6}$ and $R \epsilon \Re^{3 \times 3}$ defined as (it will be assumed in this research that all off diagonal terms of weighting matrices will remain zero):

$$Q = \begin{bmatrix} diag(Q_{\alpha,i}) \\ diag(Q_{\beta,i}) \end{bmatrix} \tag{6.7a}$$

$$R = \left[ \ diag(R_i) \ \right], \quad i = 1, 2, 3 \tag{6.7b}$$

where $\alpha$ is a weight on modeling uncertainty in the states $\psi, \theta, \phi$ and $\beta$ represents the weight of modeling uncertainty in the states $\omega_x, \omega_y, \omega_z$. The matrix $R$ is a weight on the measurement noise in the available outputs $(\psi, \theta, \phi)$. The importance in partitioning the matrix $Q$ between two different weight factors is that measurements are only available for the first three states (weights are significantly different in situations where measurements are not available). Selecting $Q$, along with $R$, is an iterative process, and during the tuning stage, the elements of $Q_{\alpha,i}$ may vary slightly from each other. However, relative to $Q_{\beta,i}$, they may be orders of magnitude apart. The relative magnitude of $Q_{\alpha,i}$ and $Q_{\beta,i}$ is first determined, followed by the tuning of each element within the partitioned matrices. Ultimately, trial and error simulations are conducted until the most acceptable weight matrices are determined. Selection criteria includes filtering effectiveness and tracking ability.

The $Q$ and $R$ matrices selected after weight tuning are as follows:

$$Q = \begin{bmatrix} 0.01 & 0 & 0 & 0 & 0 & 0 \\ 0 & 0.01 & 0 & 0 & 0 & 0 \\ 0 & 0 & 0.01 & 0 & 0 & 0 \\ 0 & 0 & 0 & 20000 & 0 & 0 \\ 0 & 0 & 0 & 0 & 20000 & 0 \\ 0 & 0 & 0 & 0 & 0 & 20000 \end{bmatrix} \tag{6.8a}$$

$$R = \begin{bmatrix} 10000 & 0 & 0 \\ 0 & 10000 & 0 \\ 0 & 0 & 10000 \end{bmatrix} \tag{6.8b}$$

The Kalman gains are obtained using the $Q$ and $R$ matrices and are calculated via a MATLAB routine and defined as:

$$L = \begin{bmatrix} 1.6697 & 0 & 0 \\ 0 & 1.6697 & 0 \\ 0 & 0 & 1.6697 \\ 1.3939 & -0.2388 & 0 \\ 0.2388 & 1.3939 & 0 \\ 0 & 0 & 1.4142 \end{bmatrix}$$

(6.9)

Results for Euler angle and body rate estimation can be found in Figures 6-1 and 6-2, respectively. From inspection of the oscillatory nature of the $\omega_x$ and $\omega_y$ body rates the satellite is experiencing nutation, while the filter attempts to track those states. Estimation error can also be seen in Figures 6-3 and 6-4. Although the error is extremely small, relative to the actual magnitudes of attitude and body rates, estimates produced by the Kalman filter are not expected to be accurate enough when implemented in attitude control systems. Also, the error in body rates about the x and y axes also increase after significant simulation time.

The results illustrate that the Kalman filter is ineffective at filtering measurement noise from attitude estimates as well as accurately tracking all satellite states. The Kalman filter takes a significant amount of time to begin to converge to actual body rate values, especially with respect to $\omega_y$, although it does effectively filter body rate noise that could be a result from attitude measurements. Measured Euler angle parameters ($\psi$, $\theta$, $\phi$) that are corrupted with measurement noise are ineffectively filtered as illustrated in Figure 6-3. The maximum steady state error is equivalent to the measurement noise of $\pm.05$ rad, illustrating that the filter is extremely ineffective, even as the weight matrix $R$ is increased. Also, in instances where there is a high rate of change of these parameters, the Kalman filter has difficulty maintaining accurate estimates.
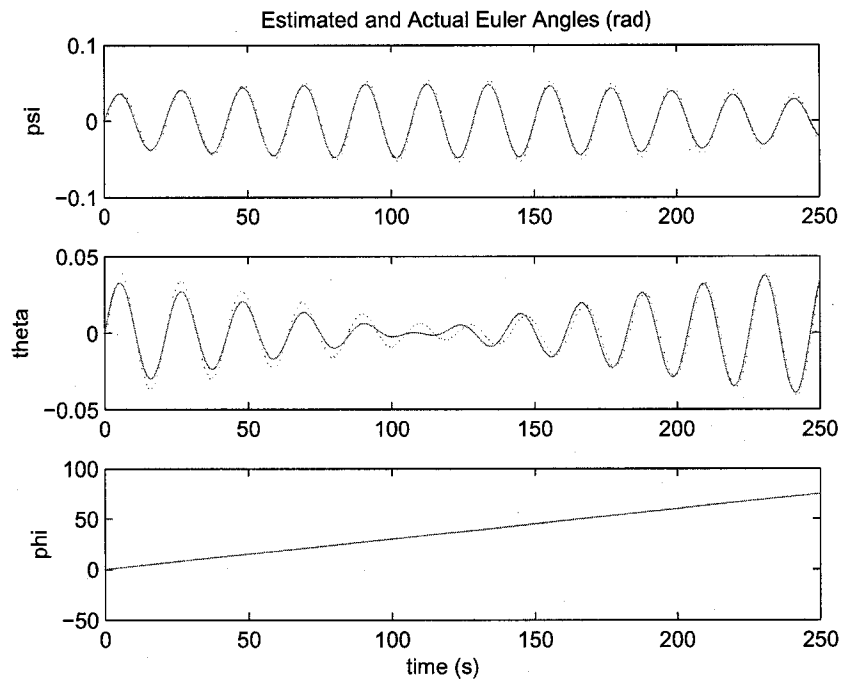
Figure 6-1: Kalman Filter Euler Angle Estimations
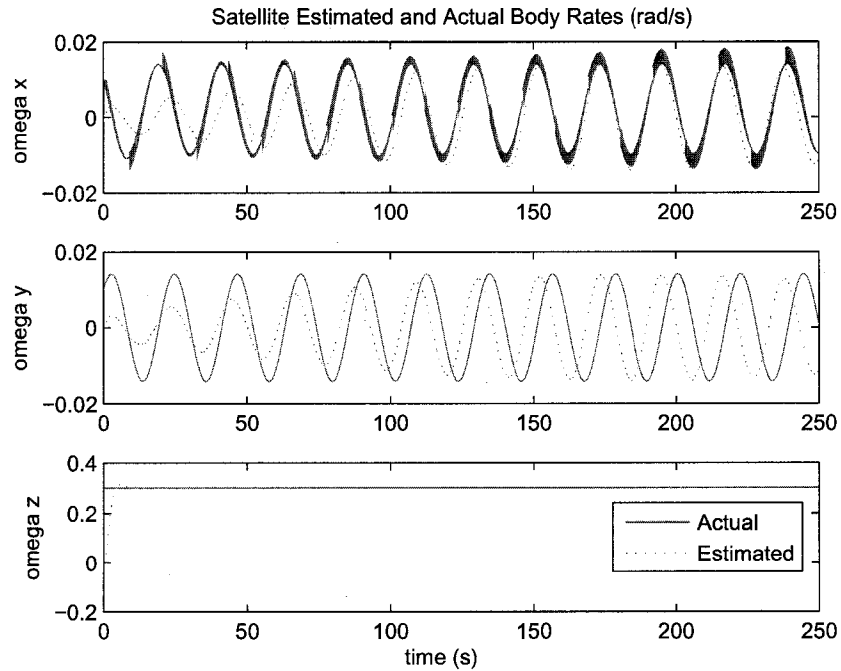


Figure 6-2: Kalman Filter Body Rate Estimations
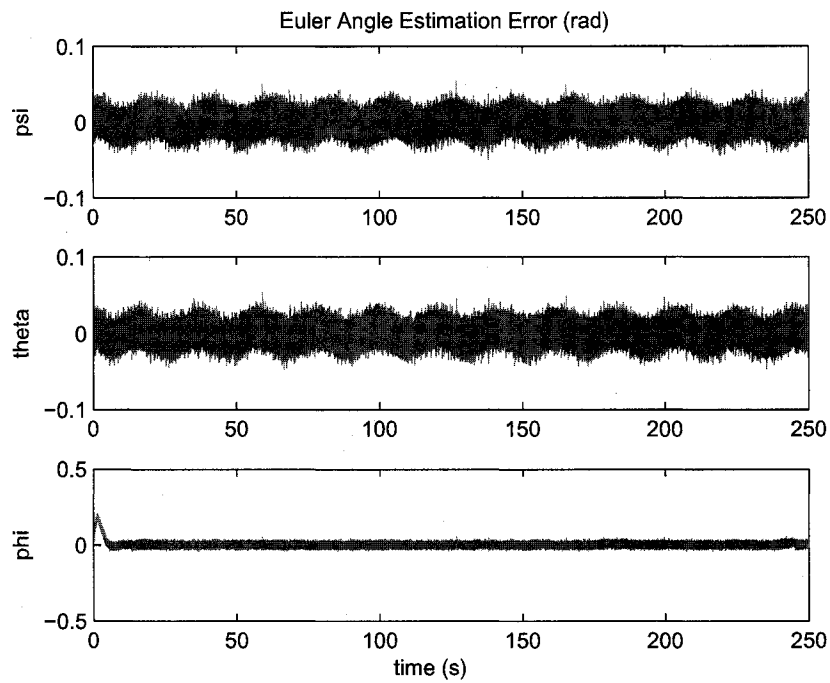
Figure 6-3: Kalman Filter Euler Angle Estimation Error
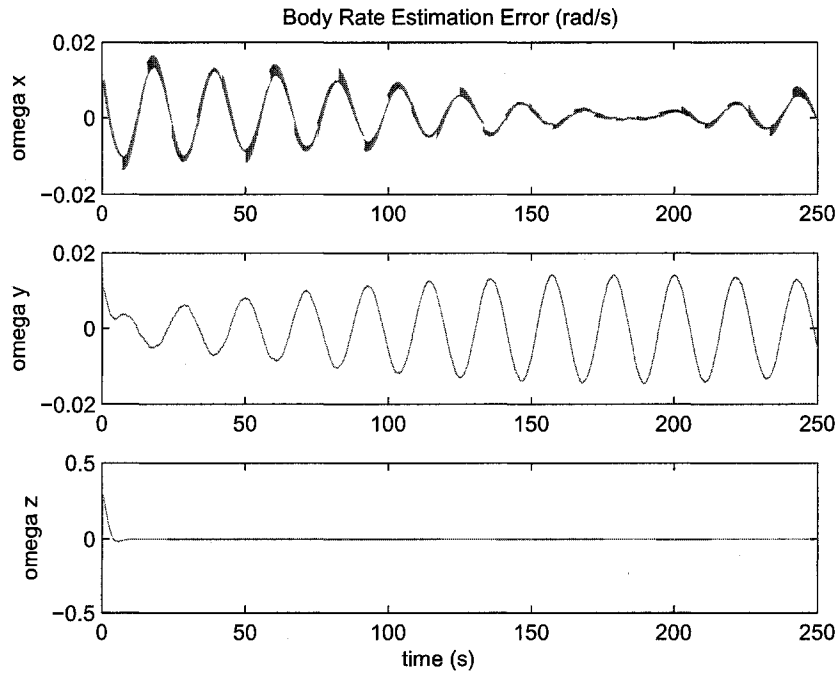


Figure 6-4: Kalman Filter Body Rate Estimation Error

Kalman filter MATLAB simulation code and diagrams may be found in Appendix A.

## 6.3 Extended Kalman Filter

The EKF is investigated for its effectiveness in estimating satellite attitude. For this design and analysis, the following observer dynamics are adopted from Eqs.(6.1):

$$
f(\hat{x}(t), t) = \begin{bmatrix} \hat{\omega}_x + (\hat{\omega}_z \cos\hat{\psi} + \hat{\omega}_y \sin\hat{\psi})\tan\hat{\theta} \\ \hat{\omega}_y \cos\hat{\psi} - \hat{\omega}_z \sin\hat{\psi} \\ (\hat{\omega}_z \cos\hat{\psi} + \hat{\omega}_y \sin\hat{\psi})\sec\hat{\theta} \\ ((I_y - I_z)/I_x)\,\hat{\omega}_y\hat{\omega}_z \\ ((I_z - I_x)/I_y)\,\hat{\omega}_x\hat{\omega}_z \\ ((I_x - I_y)/I_z)\,\hat{\omega}_x\hat{\omega}_y \end{bmatrix} \tag{6.10}
$$

The Jacobian matrix of the observer dynamics in Eq.(6.10) can be found in Appendix A.

Simulation parameters are listed in Table 6.2. An external moment of $M = 0.001\sin(.3t)$ N-m is added to all three axes to simulate unknown uncertanties/disturbances acting on the satellite that oscillate at the same frequency as the satellite rotation. This is to emulate disturbances that could be acting on the spacecraft while spinning at 3 rotations per minute (0.3 rad/s). These disturbance torques act about the $x$, $y$ and $z$ axes of the spacecraft body-fixed reference frame and are consistent in magnitude with external torques acting on orbiting spacecraft at a given altitude of approximately $10^5$ km [5]. Also, a 10 percent error in moment of inertia values are in the observer dynamics to simulate further parametric uncertainty. The EKF's robustness to such common inconsistencies are analyzed.

|  | Actual System | Observer |
|---|---|---|
| I.C.: $\psi, \theta, \phi$ $(rad)$ | 0, 0, 0 | 0, 0, 0 |
| I.C.: $\omega_x, \omega_y, \omega_z$ $(rad/s)$ | 0.01, 0.01, 0.3 | 0,0,0 |
| Inertia Matrix $(kg \cdot m^2)$ | $\begin{bmatrix} 8402.64 & -58.8 & -44.6 \\ -58.8 & 8411.97 & -100 \\ -44.66 & -100 & 16414.66 \end{bmatrix}$ | $\begin{bmatrix} 8000 & 0 & 0 \\ 0 & 8600 & 0 \\ 0 & 0 & 17500 \end{bmatrix}$ |
| Noise bounds $(rad)$ | $\pm 0.03$ | |

Table 6.2: Simulation Parameters for the Extended Kalman Filter

As with the selection of weight matrices in Kalman filter design, EKF matrices are selected through partitioning. It is for this reason of unknown disturbances and parametric uncertainty that the Euler moment equations describing $\omega_x, \omega_y$ and $\omega_z$ are most negatively affected and, therefore, require $Q_\beta$ to be orders of magnitude higher then $Q_\alpha$. The relative magnitude of the two partitioned matrices that construct $Q$ is determined, followed by the individual tuning of the diagonal elements. Iteration and analysis of each simulation's filtering and tracking effectiveness determine the final matrices. $Q$ and $R$ weight matrices are defined as:

$$Q = \begin{bmatrix} 0.1 & 0 & 0 & 0 & 0 & 0 \\ 0 & 0.1 & 0 & 0 & 0 & 0 \\ 0 & 0 & 0.1 & 0 & 0 & 0 \\ 0 & 0 & 0 & 120000 & 0 & 0 \\ 0 & 0 & 0 & 0 & 100000 & 0 \\ 0 & 0 & 0 & 0 & 0 & 130000 \end{bmatrix} \tag{6.11a}$$

$$R = \begin{bmatrix} 10^6 & 0 & 0 \\ 0 & 10^6 & 0 \\ 0 & 0 & 10^6 \end{bmatrix} \tag{6.11b}$$
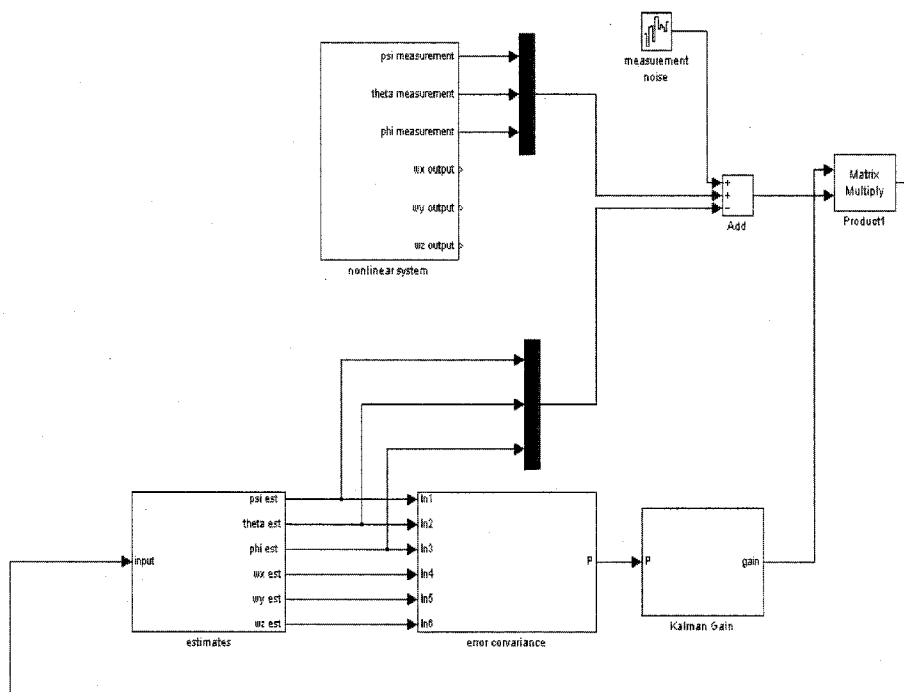
Figure 6-5: Extended Kalman Filter Simulation Diagram

The EKF simulation model is shown in Figure 6-5, where the estimates and non-linear system represent equations of motion for the observer dynamics and actual satellite system, respectively. More detailed simulation diagrams can be found in Appendix A.

To improve estimation results further, body rate estimations in particular, the overall influence of the observer loop on body rate correction terms is investigated. It can be seen through inspection of the closed loop observer simulation diagram that the EKF is updated via Euler angle errors only, since these states are the only ones being measured. The error that is produced, for example, in Figure 6-11 is not observed by the closed loop EKF, and therefore cannot guarantee convergence to zero. By investigating the correction terms that affect the satellite body rates, and independently tuning those, the percentage error and steady state error can greatly be improved. The gains are tuned through iterations starting with the $\omega_x$ correction
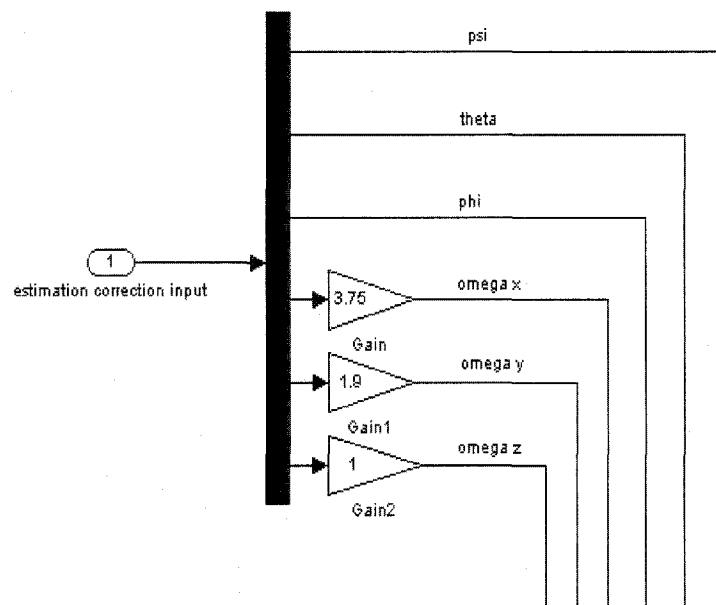
Figure 6-6: Correction Input Tuning
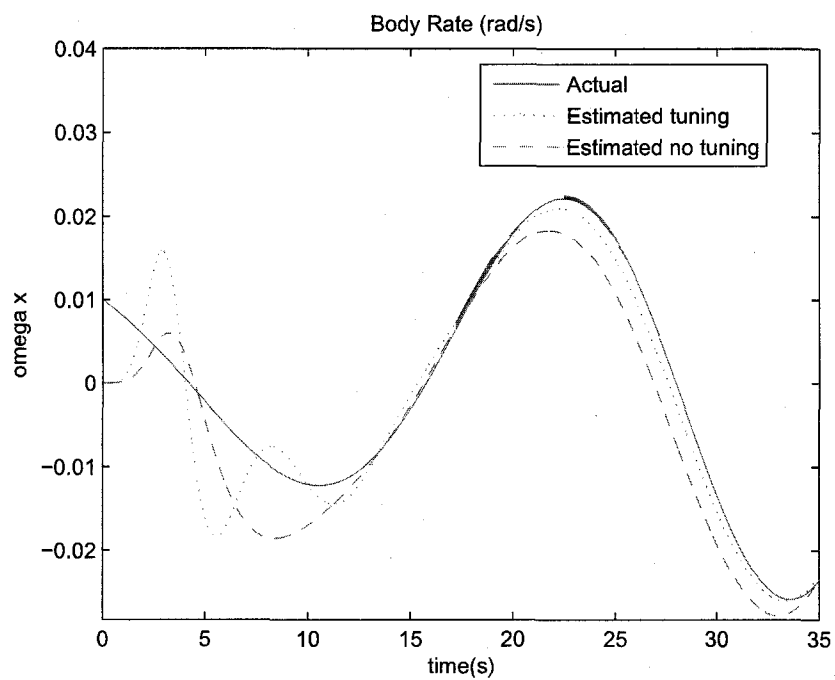


Figure 6-7: EKF Correction Input Tuning Influence on Body Rates $(\omega_x)$

term and then independently tuning for the $\omega_y$ and $\omega_z$ correction terms. Steady-state error is drastically reduced while maintaining effective noise filtering as gains increase. Slowly, as the gains increase, so does the noise that is being amplified by the gains. Figure 6-6 illustrates the final gain selections of 3.75, 1.9 and 1 for $\omega_x$, $\omega_y$ and $\omega_z$, respectively, used to tune body rate correction terms. Figure 6-7 illustrates an example of the improvement in body rate tracking for $\omega_x$ with the additions of correction term tuning. Since this tuning occurs around selected initial conditions, further investigation is needed to be done into the bounds of spacecraft operating conditions in which the presented correction input tuning is effective.
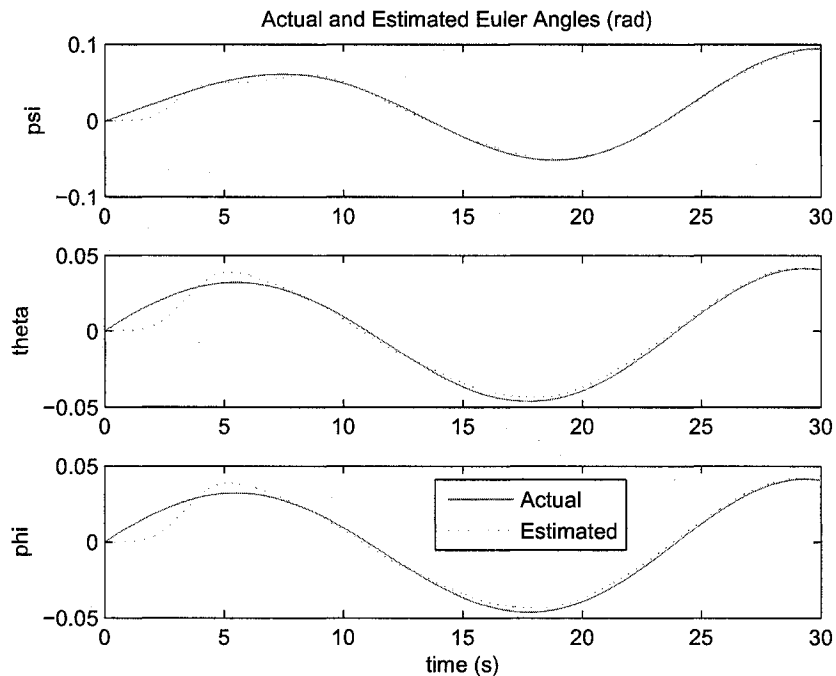


Figure 6-8: Extended Kalman Filter Euler Angle Estimations

Euler Angle Estimation Error (rad)
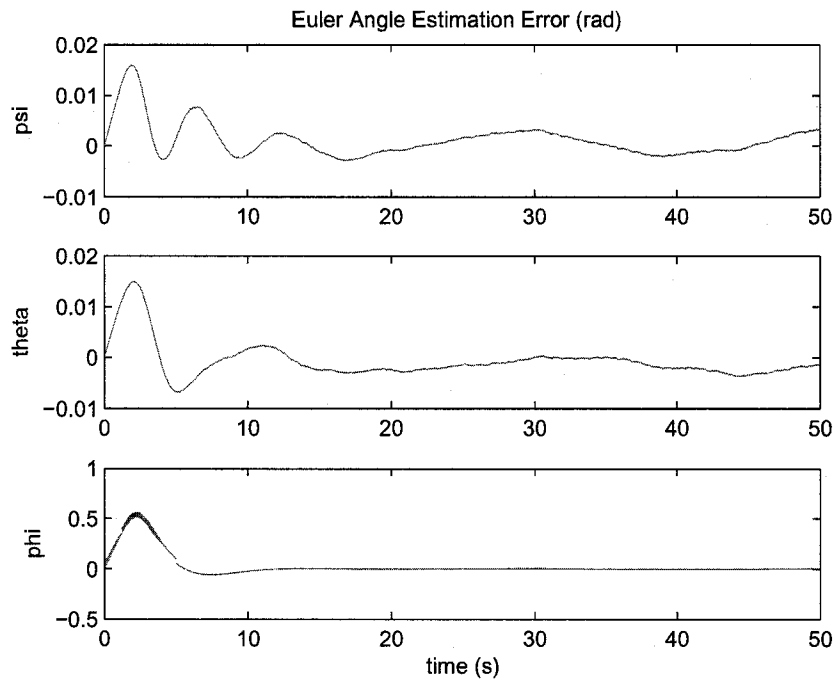
Figure 6-9: Extended Kalman Filter Euler Angle Estimation Error

Actual and Esimated Body Rates (rad/s)
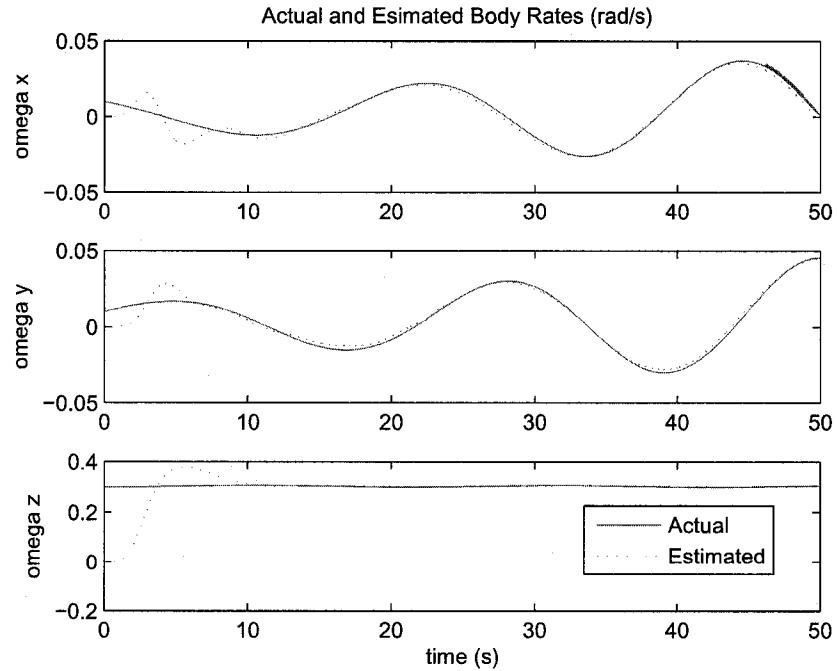
Figure 6-10: Extended Kalman Filter Body Rate Estimations
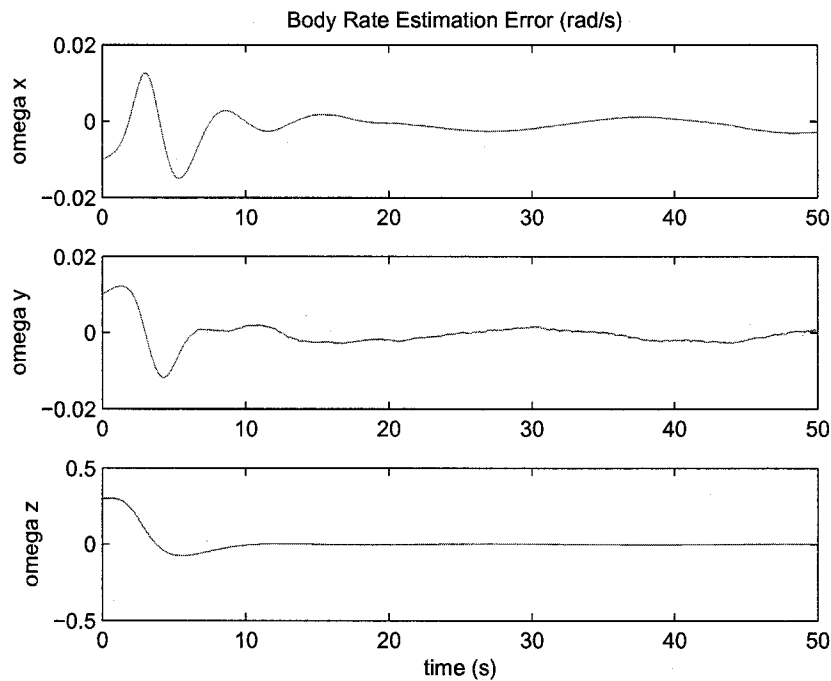
Figure 6-11: Extended Kalman Filter Body Bate Estimation Error

The Extended Kalman Filter offers a much more comprehensive and effective estimation technique, as compared to its linear counterpart. From inspection of the simulation results, it can be seen that noise filtering, and body rate estimation is greatly improved by using a nonlinear estimation technique. Figures 6-8 and 6-9 show the EKF's effectiveness at filtering measurement noise, which is vital to an effective control sequence to maintain a desired satellite attitude. It can also be seen in Figures 6-10 and 6-11 that the EKF estimates body rates effectively, especially given unknown disturbances and modeling uncertainties which typically affect these states the most. Although the error magnitude is small, a percent error is evaluated from the steady-state amplitude of oscillations of all six states and their respective amplitude of stead-state error. Magnified error signals for body rate and Euler angle estimation can be seen in Figures 6-12 and 6-13. These results are tabulated, along with maximum steady-state error for all six states in Tables 6.3 and 6.4.
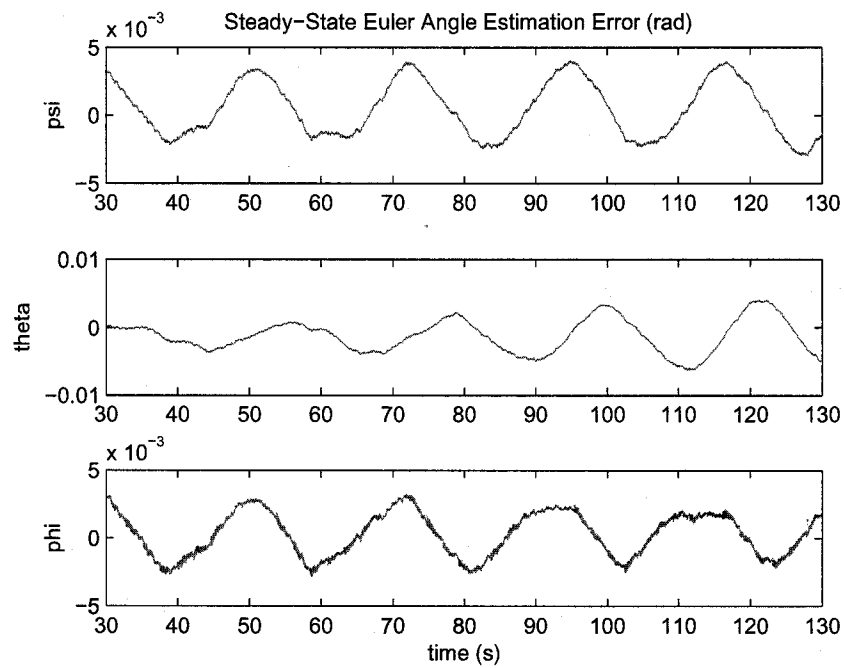
Figure 6-12: Steady-State Extended Kalman Filter Euler Angle Estimation Error
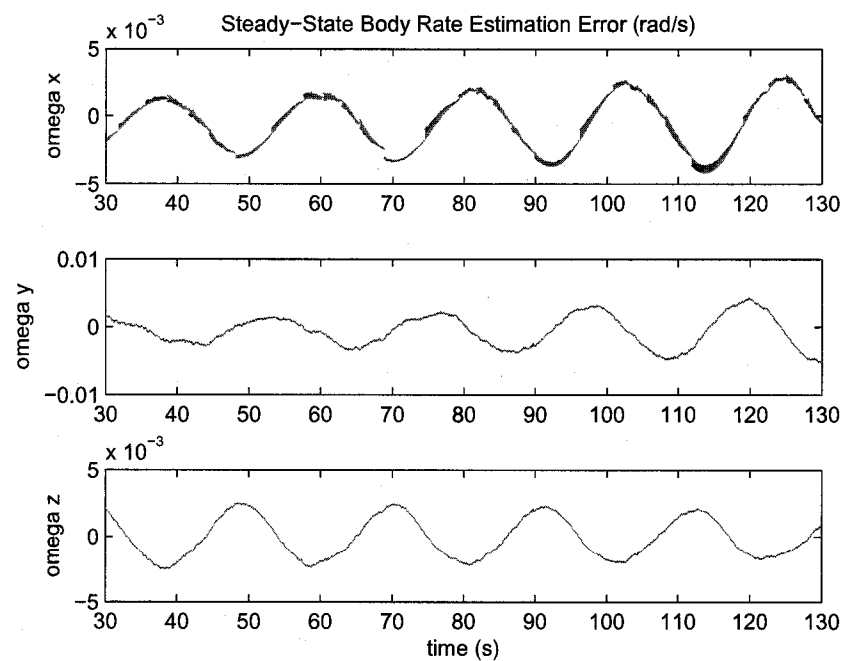


Figure 6-13: Steady-State Extended Kalman Filter Body Rate Estimation Error

|  | $\psi$ | $\theta$ | $\phi$ |
|---|---|---|---|
| Steady-State Error $(rad)$ | $\pm 0.004$ | $\pm 0.006$ | $\pm 0.002$ |
| Percent Error | 2.14 | 4.7 | 0.0079 |

Table 6.3: Extended Kalman Filter Steady-State Euler Angle Estimation Errors

|  | $\omega_x$ | $\omega_y$ | $\omega_z$ |
|---|---|---|---|
| Steady-State Error $(rad/s)$ | $\pm 0.004$ | $\pm 0.005$ | $\pm 0.004$ |
| Percent Error | 1.68 | 1.48 | .66 |

Table 6.4: Extended Kalman Filter Steady-State Body Rate Estimation Errors

From inspection of the results it can be seen that EKF has difficulty in rejecting disturbance torques. Error oscillation of the body rate and Euler angles is an indication that the estimator is not effectively tracking these states, thus, causing an error signal that is of the same magnitude of the disturbance torque acting on all three axes of the satellite. It should be noted that while this design offers promising results for application to the NASA MMS mission, slight improvements in steady-state error and percent error may be achieved upon further tuning of the design parameters. There is a constant tradeoff when trying to filter measurement noise, while still using the available star tracker data, and not relying too heavily on inaccurate mathematical models. As the weights of $R$ increase, more measurement noise is filtered. However, this affects a greater dependency on the accuracy of mathematical models, which increase the effects of unknown disturbances and parametric uncertainty. Also, a full Monte-Carlo analysis, that would test the proposed design for all operating conditions, should be performed to guarantee stability, which cannot be otherwise proven.

## 6.4   Sliding Mode Observer

The Sliding Mode Observer (SMO) is the final estimation technique investigated for full state estimation. The goal of this research is to compare results and closed-loop performance to that of the EKF for estimation of MMS dynamics and kinematics. As with the Kalman Filter and EKF, the vector of state estimates are as follows:

$$\hat{x} = \left[\hat{\psi}, \hat{\theta}, \hat{\phi}, \hat{\omega}_x, \hat{\omega}_y, \hat{\omega}_z\right]^T \tag{6.12}$$

The Sliding Mode Observer dynamics are defined as:

$$\dot{\hat{x}} = \hat{f}(\hat{x}, t) + B\hat{u}(t) + L(Cx - C\hat{x}) + K1_s \hat{y} = C\hat{x}$$

where $C = [I_{3\times3} 0_{3\times3}]$ is the output matrix of measured states. The input torques into the system are represented by $\hat{u}(t)$ that act on states $\omega_x$, $\omega_y$ and $\omega_z$, and $B = \left[0_{3\times3} \ \hat{I}_{3\times3}\right]$. The equations of motion are identical to those used in the Extended Kalman Filter and given in Eq. (6.10). Observer gain matrices are represented by $L$ and $K$ in which $L, K \in \Re^{6x3}$. The Luenberger gain, $L$, is an optimal Kalman gain determined from a linearzied system model and remains constant throughout the simulation. The Sliding Mode correction term ensures that the error trajectory remains on the sliding surface and is selected through design iteration.

Simulation parameters for the sliding mode observer are listed in Table 6.5. As with the EKF, an external moment of $M = 0.001\sin(.3t)$ N-m was added to all three axes to simulate unknown disturbances as well as a 10 percent uncertainty in principle moment of inertia parameters. The SMO simulation diagram is shown in Figure 6-14.

Unlike in EKF design, the SMO offers many more design parameters that affect system performance. In the design of the SMO, the sliding surface selection proves to be the most influential design parameter. Multiple different surfaces are tested through simulations until the most effective surface in state tracking and noise filtering is determined. As the number of sliding surfaces increase, as do the the number of

| | Actual System | Observer |
|---|---|---|
| I.C.: $\psi, \theta, \phi$ $(rad)$ | 0, 0, 0 | 0, 0, 0 |
| I.C.: $\omega_x, \omega_y, \omega_z$ $(rad/s)$ | 0.01, 0.01, 0.3 | 0,0,0 |
| Inertia Matrix $(kg \cdot m^2)$ | $\begin{bmatrix} 8402.64 & -58.8 & -44.6 \\ -58.8 & 8411.97 & -100 \\ -44.66 & -100 & 16414.66 \end{bmatrix}$ | $\begin{bmatrix} 8000 & 0 & 0 \\ 0 & 8600 & 0 \\ 0 & 0 & 17500 \end{bmatrix}$ |
| Noise bounds $(rad)$ | $\pm 0.03$ | |

Table 6.5: Simulation Parameters for the Sliding Mode Observer
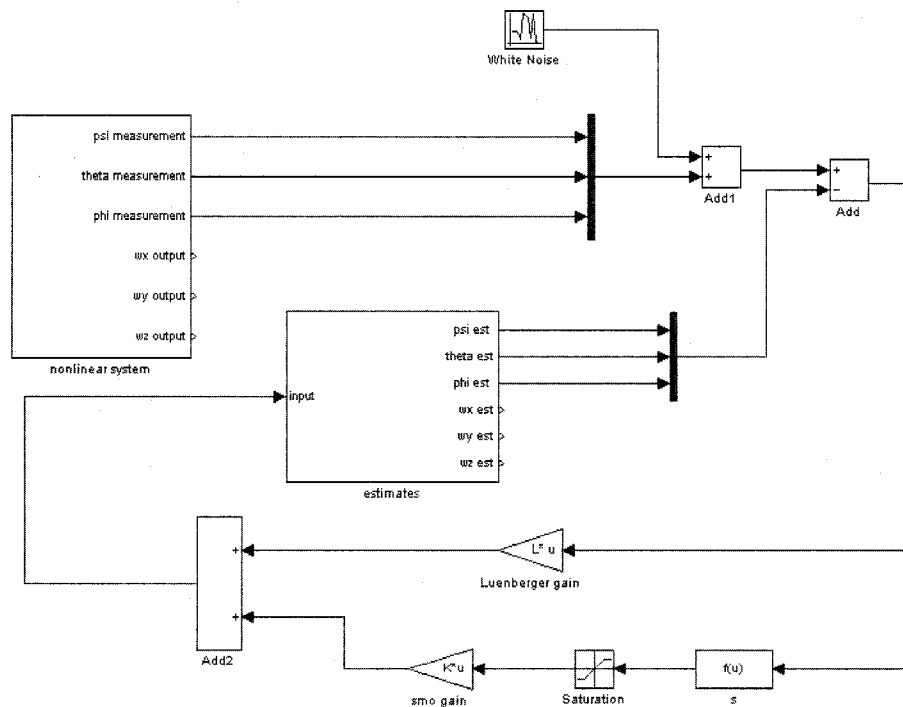


Figure 6-14: Sliding Mode Observer Simulation Diagram

elements that must be selected in the SMO gain $K$. As with the Kalman filter and EKF, the SMO gain matrix $K$ is tuned through trial and error simulations while analyzing estimator performance. The sliding surface $s$ is defined through the switching function $\mathbf{1}_s$ as:

$$\mathbf{1}_s = sat\left(\frac{s}{\rho}\right) = sat\left(\frac{z_\psi + z_\theta + z_\phi}{\rho}\right) \tag{6.13}$$

where $z$ is the error between measured and estimated states, and $\rho$ is another design parameter referred to as the sliding surface boundary layer.

The Luenberger gain is adopted from the the Kalman filter analysis for a linear system while the sliding mode gain is tuned through trial and error and defined as:

$$L = \begin{bmatrix} 1.6697 & 0 & 0 \\ 0 & 1.6697 & 0 \\ 0 & 0 & 1.6818 \\ 1.3939 & -0.2388 & 0 \\ 0.2388 & 1.3939 & 0 \\ 0 & 0 & 1.4142 \end{bmatrix}, \quad K = \begin{bmatrix} 1 \\ 1 \\ 1 \\ 1 \\ 1 \\ 1 \end{bmatrix} * 10^{-3} \tag{6.14}$$

with the boundary layer chosen as $\rho = .0006$. As with the EKF, the correction terms for $\omega_x$, $\omega_y$, and $\omega_z$ are tuned to improve estimates when gain tuning is exhausted as with the EKF design. Figure 6-15 illustrates the gains that are used for correction input tuning.
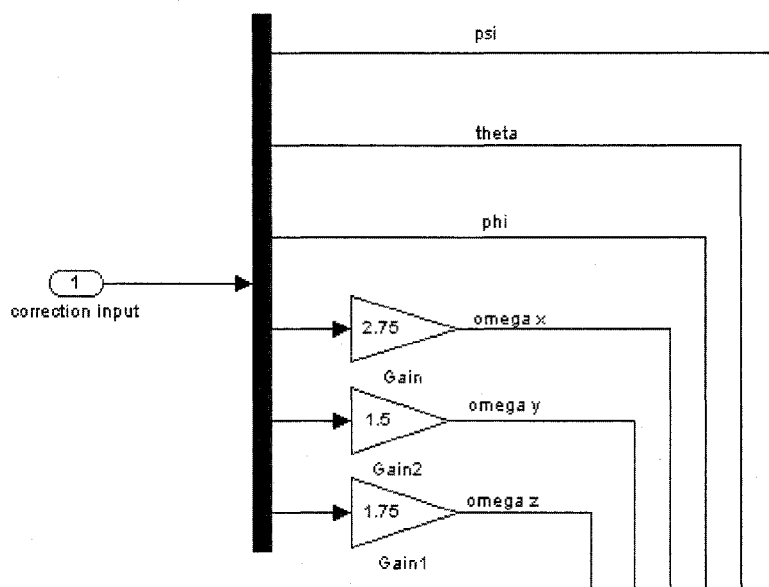
Figure 6-15: Sliding Mode Observer Correction Input Tuning
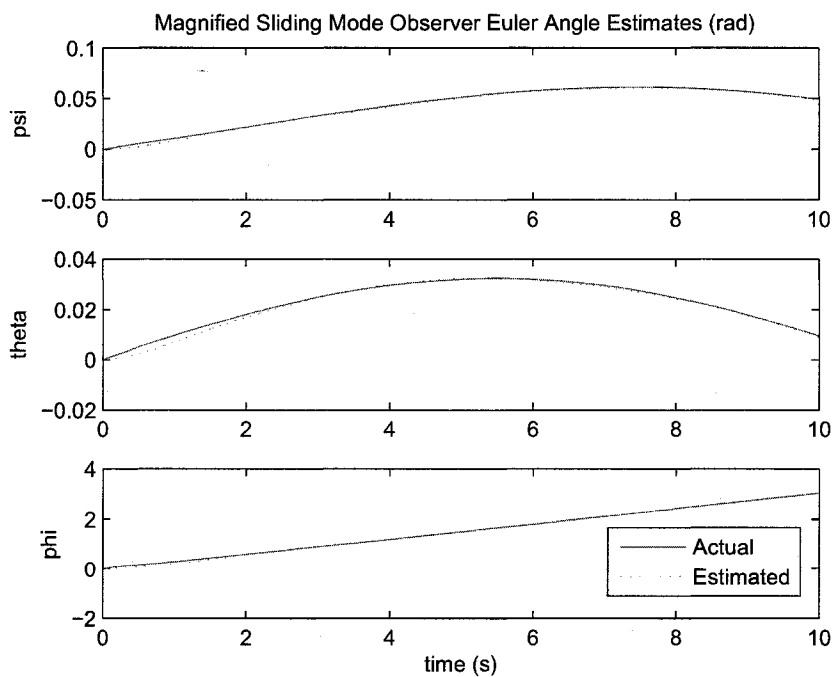


Figure 6-16: Sliding Mode Observer Euler Angle Estimations
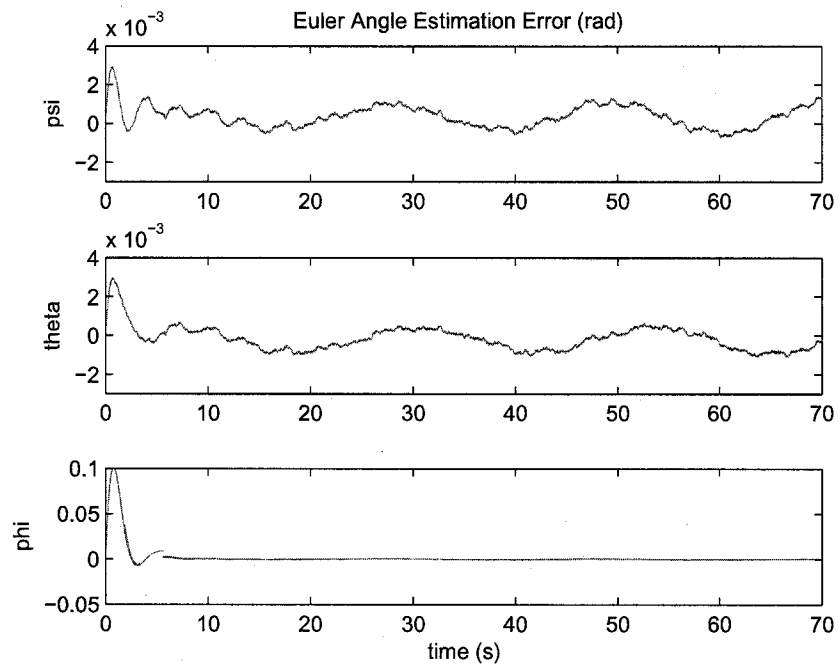
Figure 6-17: Sliding Mode Observer Euler Angle Estimation Error
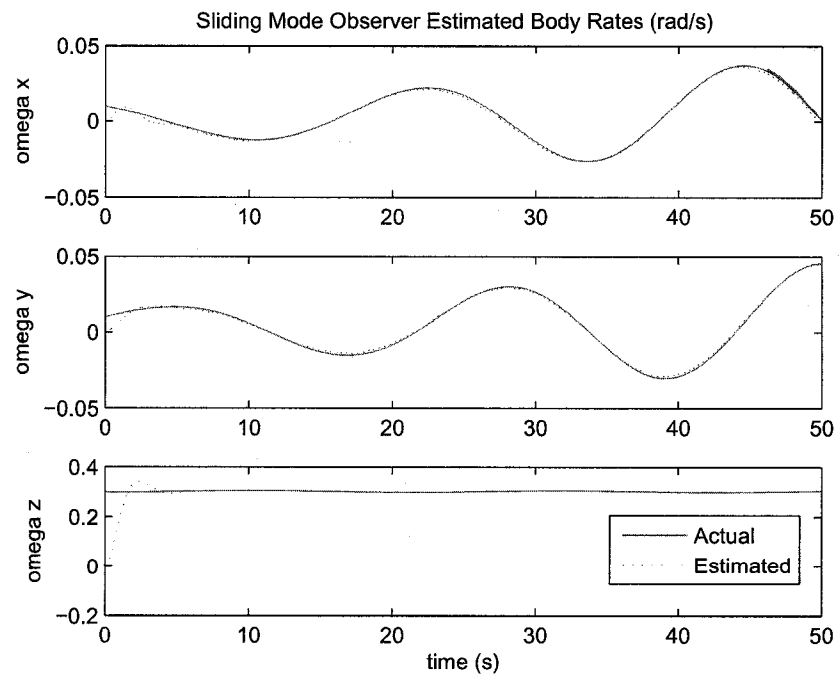


Figure 6-18: Sliding Mode Observer Body Rate Estimations
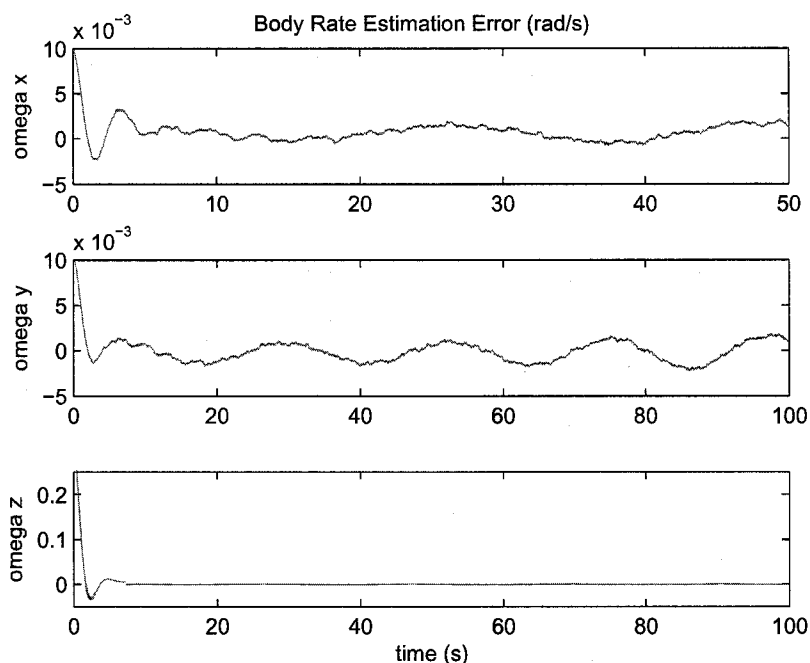
Figure 6-19: Sliding Mode Observer Body Rate Estimation Error

Figures 6-18 and 6-19 show the effectiveness of the SMO at tracking satellite body rates while Table 6.6 shows error results. Once again, it is important in recognizing overall percentage error between estimated and actual states to determine the effectiveness of the observer and usefulness of the observed states. States with large percent errors are ineffective when used to update a control algorithm to maintain constant spin and attitude while rejecting nutation. Compared to the EKF, it can be seen that the tracking error and steady-state percent error are smaller for the SMO. However, the estimates have slightly more measurement noise as seen in Figure 6-17. Euler angle estimation results are shown in Figures 6-16 and 6-17 with tabulated results presented in Table 6.7. Initial errors for both body rates and Euler angles are small for the SMO compared to the EKF estimates. It can also be seen from steady-state error analysis in Figures 6-20 and 6-21 that the SMO is much more effective at tracking satellite states under unknown disturbance torques.
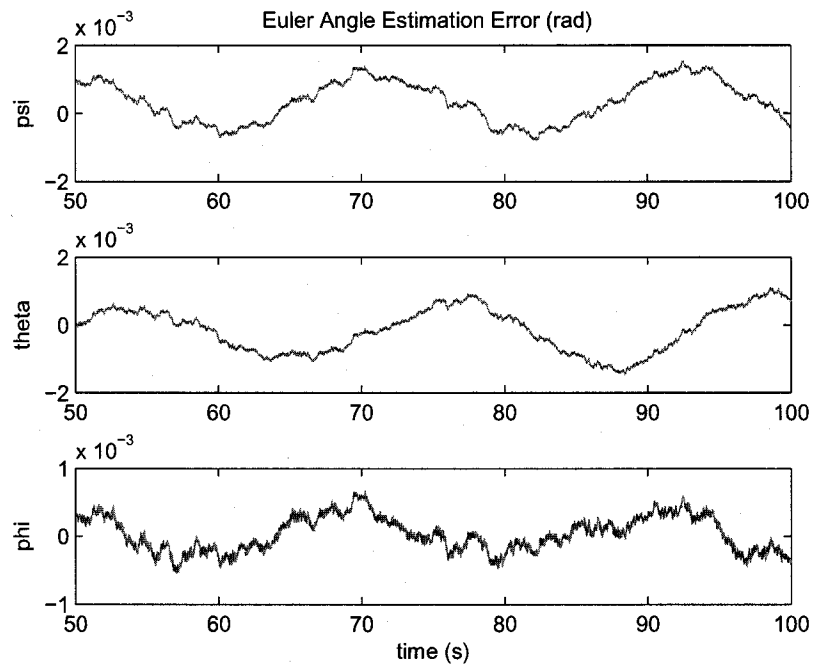
Figure 6-20: Steady-State Sliding Mode Observer Euler Angle Estimation Error
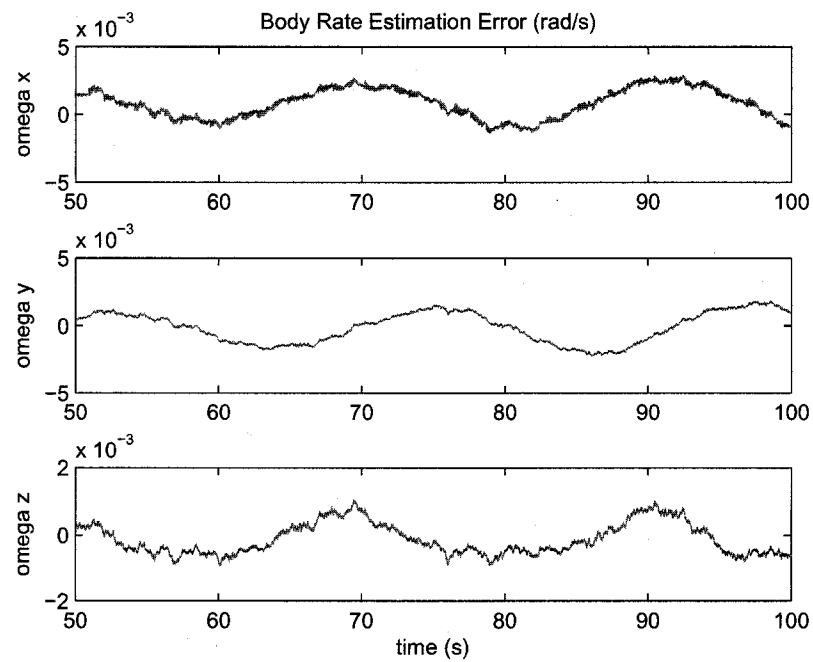


Figure 6-21: Steady-State Sliding Mode Observer Body Rate Estimation Error

|  | $\omega_x$ | $\omega_y$ | $\omega_z$ |
|---|---|---|---|
| Steady-State Error ($rad/s$) | ±0.0025 | ±0.0015 | ±0.0007 |
| Percent Error | 1.81 | 0.633 | 0.23 |

Table 6.6: Sliding Mode Observer Steady-State Body Rate Estimation Errors

|  | $\psi$ | $\theta$ | $\phi$ |
|---|---|---|---|
| Steady-State Error ($rad$) | ±0.001 | ±0.0004 | ±0.0007 |
| Percent Error | 0.55 | 0.50 | 0 |

Table 6.7: Sliding Mode Observer Steady-State Euler Angle Estimation Errors

Again, it should be noted that while these results offer acceptable estimates from inspection of simulation results, it is their implementation into a control sequence that will determine their overall usefulness. The addition of multiple sliding surfaces that involve derivatives and integrals of the estimation error, as well as further gain tuning may result in more accurate results. However, these results are deemed acceptable for control implementation. In the following chapter, estimates produced by the Sliding Mode Observer and Extended Kalman Filter are used in a control algorithm for nutation rejection and attitude control. While the control results are presented, it should be noted that the design iteration involves control implementation, evaluation, and then further observer tuning until the more satisfactory results are obtained.

# CHAPTER 7

# FEEDBACK CONTROL WITH PERFECT

# MEASUREMENTS

Two different control techniques are tested and compared to determine the most effective technique as it applies to the NASA MMS in attitude control with perfect state knowledge. The first step in this process involves the design of a controller assuming perfect state measurements. From this design, an understanding of control accuracy can be obtained without influence of complicated effects such as measurement noise, unknown disturbances and parametric uncertainty. A linear feedback controller consisting of proportional, derivative and integral control is designed first, followed by a variable structure, sliding mode controller. Upon completion of these designs, the feedback controller is updated with state estimates from the observer algorithms developed earlier in the thesis to determine an overall optimal system for the NASA MMS application.

Thrusters are the only form of actuation on the satellite. And, because the satellite is spin-stabilized, the spacecraft is limited in its firing frequency and the duration of each firing. Other design considerations include rapid control peaks, as well as excessive oscillation, both of which can potentially excite unmodeled dynamics and potentially cause instability.

As part of the design process in developing a suitable control system, low pass filters are also developed for desired state signals. When the controller is initiated and reacts to initial errors, large transient errors and actuator signals can result. Sudden

control demands for actuator compensation can result in satellite oscillations that can, in turn, excite vibration modes, especially in the presence of highly flexible appendages. Since spin-stabilized spacecraft are sometimes given hours for reorientation after orbital maneuvers, these low pass filters prove essential for limiting demand that can be placed on thrusters by decreasing the speed of response of the system. The filters allow the controller to track command signals while avoiding sudden command impulses.

In the following sections, a linear and nonlinear feedback control system are designed assuming all states are perfectly known. Using these designs, nonlinear observers developed in Chapter 4 are implemented in the feedback system and overall system characteristics are evaluated and compared. Each controller is tuned for efficiency and to maintain desired satellite body rates and orientation, while meeting NASA design requirements.

## 7.1 Linear Feedback Control

The first control method tested uses linear feedback to control the satellite body rate and orientation. Simulation parameters are given in Table 7.1 and the desired states are defined as follows:

$$
x_{des} = \begin{bmatrix} \psi_{des} \\ \theta_{des} \\ \omega_{xdes} \\ \omega_{ydes} \\ \omega_{zdes} \end{bmatrix} = \begin{bmatrix} 0.052 \\ -0.052 \\ 0 \\ 0 \\ 0.3 \end{bmatrix} (rad, rad/s) \tag{7.1}
$$

Gains applied to the error signal, as well as the integral and derivative of the error signal are tuned to force the spacecraft to converge to desired values. Derivative control is essential to eliminate excessive system overshoot and oscillation, while inte-

| | Actual System |
|---|---|
| I.C.: $\psi, \theta, \phi$ $(rad)$ | 0, 0, 0 |
| I.C.: $\omega_x, \omega_y, \omega_z$ $(rad/s)$ | 0.01, 0.01, 0.5 |
| Inertia Matrix $(kg \cdot m^2)$ | $\begin{bmatrix} 8402.64 & 0 & 0 \\ 0 & 8411.97 & 0 \\ 0 & 0 & 16414.66 \end{bmatrix}$ |

Table 7.1: Simulation Parameters for Feedback Control of Perfect State Measurements

gral control does not significantly affect the overall system response. Linear feedback gains are defined as follows:

$$K_\lambda = [K_\alpha K_\omega], \quad \lambda = p, i, d \tag{7.2}$$

where $K_\alpha \epsilon \Re^{3\times2}$ and $K_\omega \epsilon \Re^{3\times3}$ are gain matrices associated with the Euler angle and body rate state dynamics respectively. Each of these gain matrices are first tuned independently and then augmented during simulation. This allows for a better understanding of how each gain affects the overall system response and, thus, can be tuned more effectively. As with estimator gain tuning, partitioning is utilized in selecting gains. Once diagonal terms are selected, off diagnol elements are selected through trial and error simulations.

The final feedback gains and configuration involve a PD controller. Many combinations of proportional, integral, and derivative control presented in [29] are tested for application. Below are the final gain selections based on simulation iteration and tuning:

$$K_p = \begin{bmatrix} 300 & 50 & 20 & 1 & 0 \\ 50 & 300 & 1 & 20 & 0 \\ 0 & 0 & 0 & 0 & 20 \end{bmatrix}, \quad K_d = K_p * 0.1 \tag{7.3}$$

These gains are implemented in the simulation of Figure 7-1. Also implemented in the feedback control system is a third order input command filter to limit any sudden
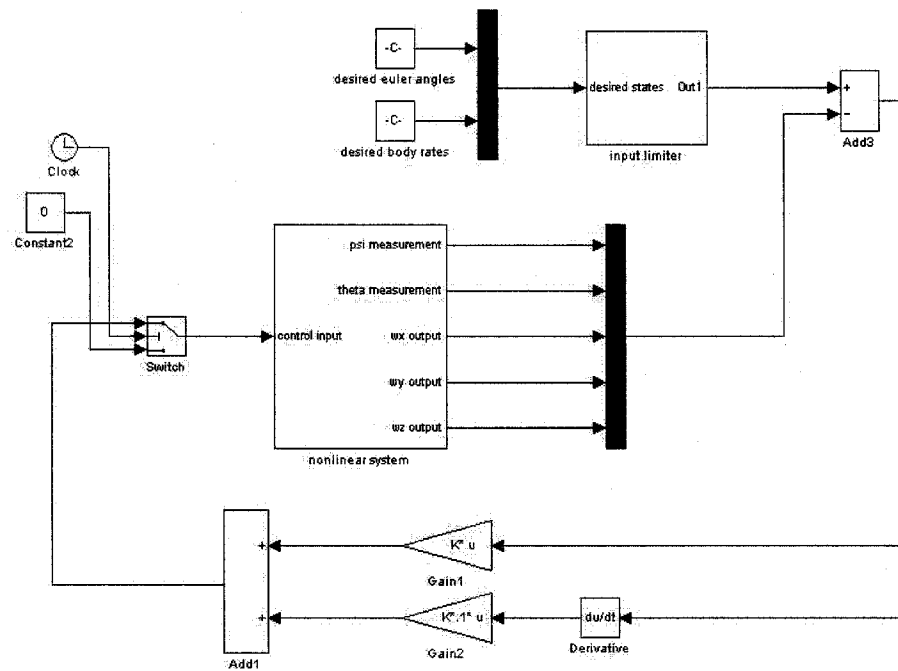
Figure 7-1: Simulation Diagram for Feedback Control of Perfect State Measurements

changes in error signals. The effects of the third order filters used to limit attitude commands can be seen in Figure 7-2 and are defined as follows:

$$\Gamma_i = \frac{1}{512s^3 + 192s^2 + 24s + 1}, \quad i = \psi, \theta, \omega_z \qquad (7.4)$$

Figure 7-3 and 7-4 show the system response of the satellite Euler angles and Euler angle estimation error while body rate estimates and error signals can be seen in Figure 7-5 and Figure 7-6. States converge to their desired trajectories, however, a steady-state nutation error exists. The $\omega_x$ and $\omega_y$ states show a steady-state error of approximately 0.016 rad/s as can be seen in Figure 7-7. Although the steady-state error still lies within NASA design requirements, multiple different control combinations are implemented to try and eliminate this steady-state error. Integral control is able to eliminate steady-state error with respect to $\omega_x$ and $\omega_y$ body rates. However, it creates steady-state error in the remaining states and drastically slows system re-
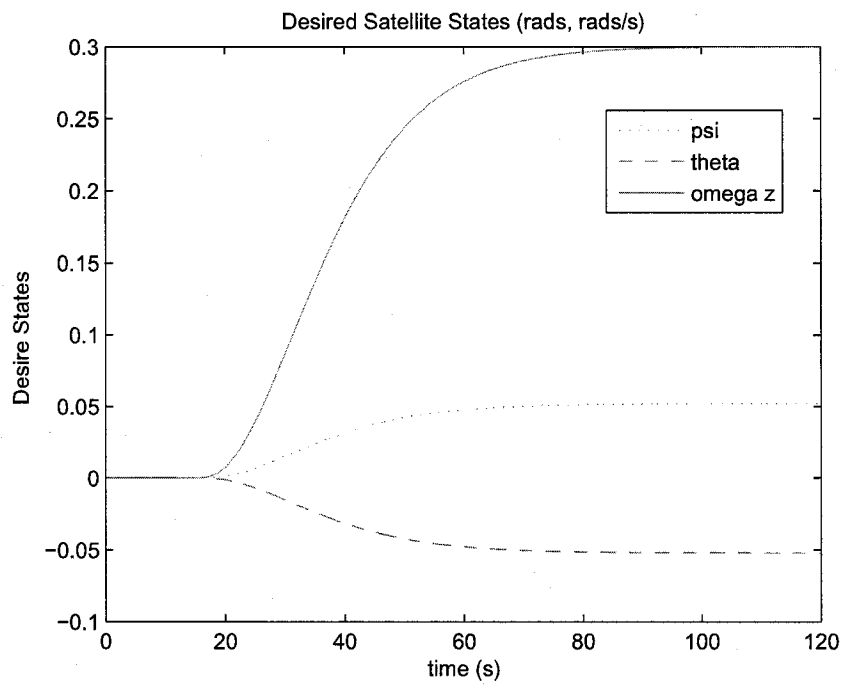
Figure 7-2: Satellite Desired States
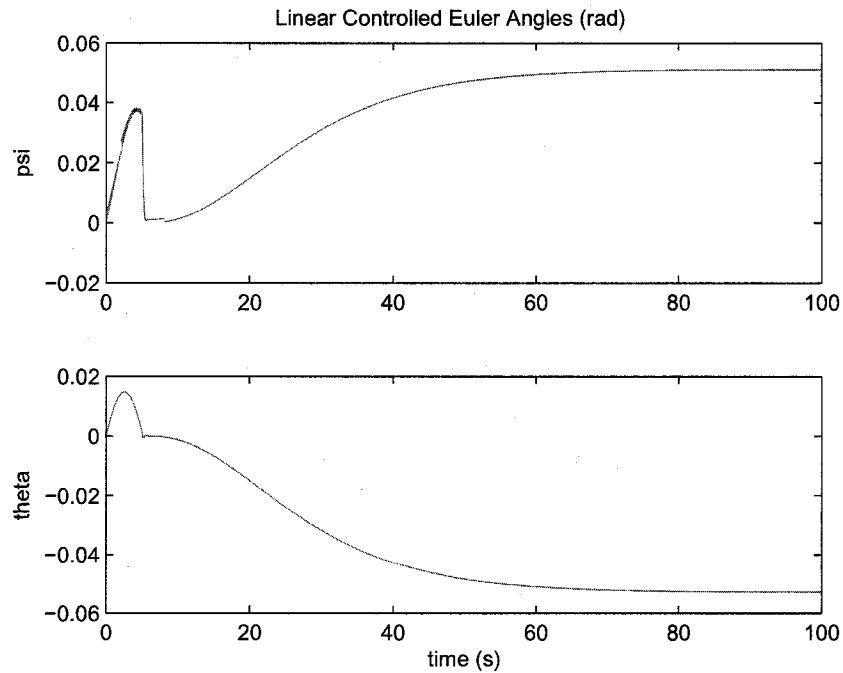


Figure 7-3: Linear Controlled Euler Angles
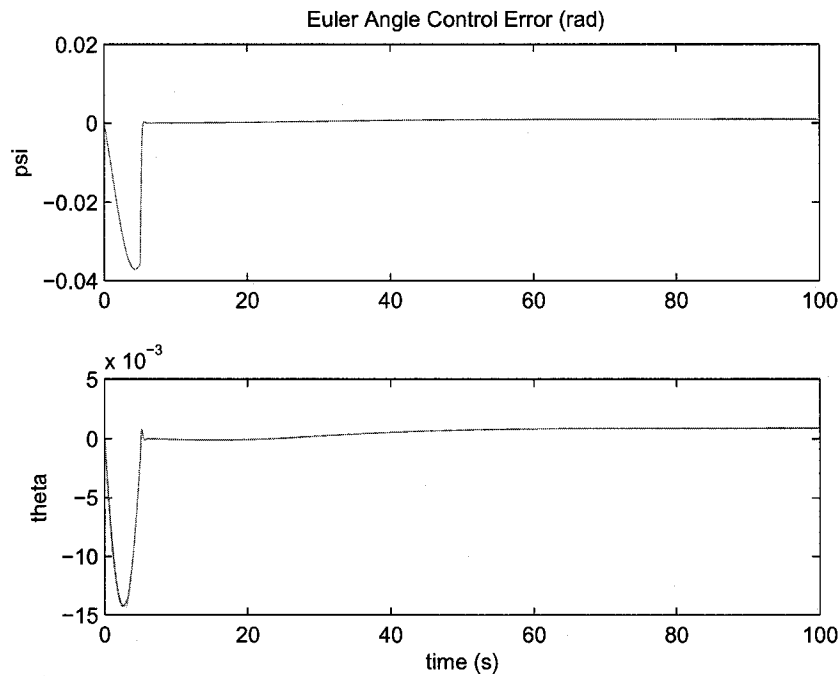
Figure 7-4: Euler Angle Error Using Linear Control

action. Integral control also increases the sharp transient response that can be seen especially in the $\omega_x$ and $\omega_y$ states. Control effort shown in Figure 7-8 has a high transient response but still fails to saturate the thrusters.

Ultimately, the tradeoff between a small steady-state nutation error and overall system response results in a proportional and derivative control that offers acceptable results for tracking control commands while eliminating excessive oscillations. Further control techniques, such as the Sliding Mode Control, must be investigated to determine if steady-state errors, particularly regarding nutation and transient errors can be improved.
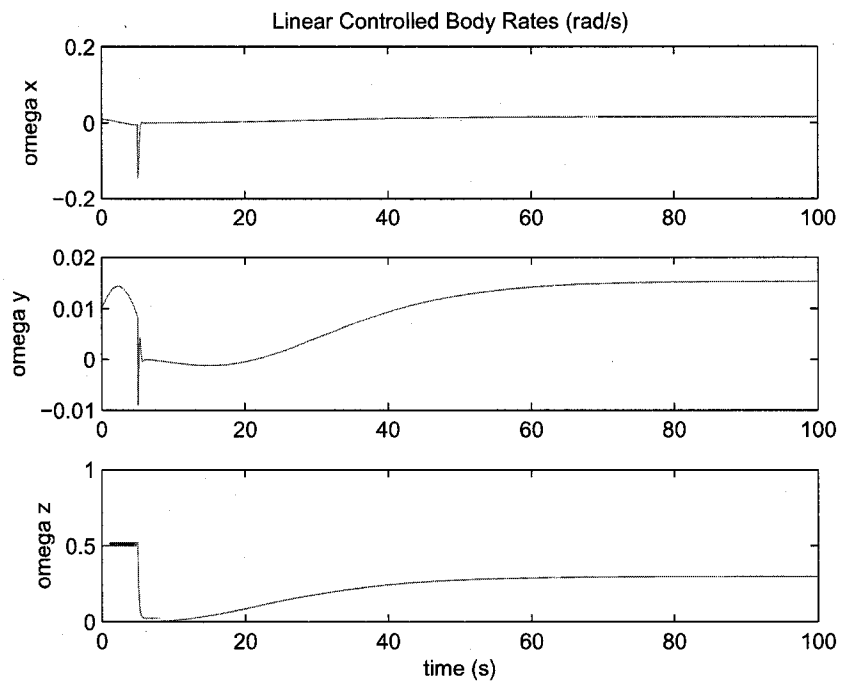
Figure 7-5: Linear Controlled Body Rates
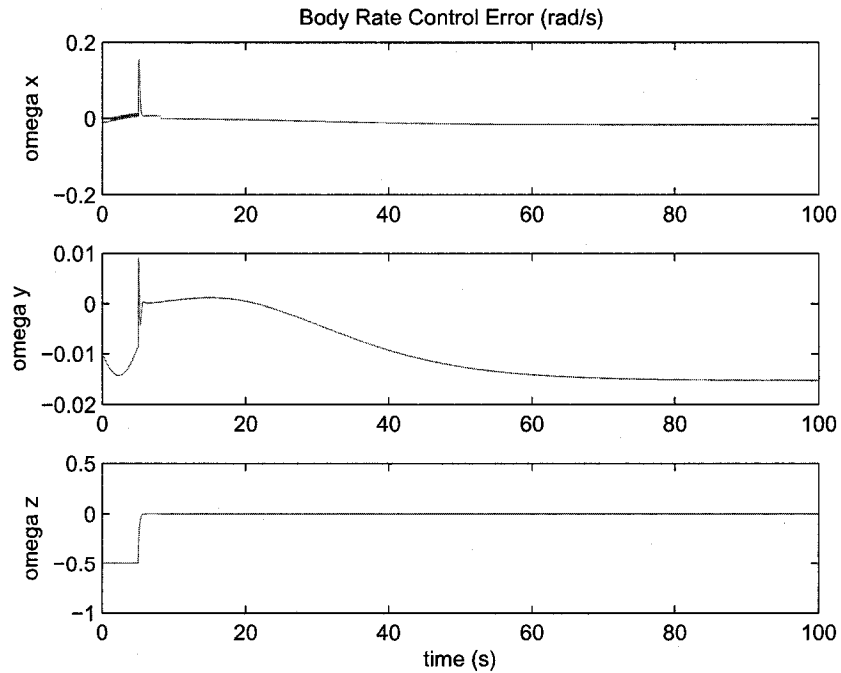


Figure 7-6: Body Rate Error Using Linear Control
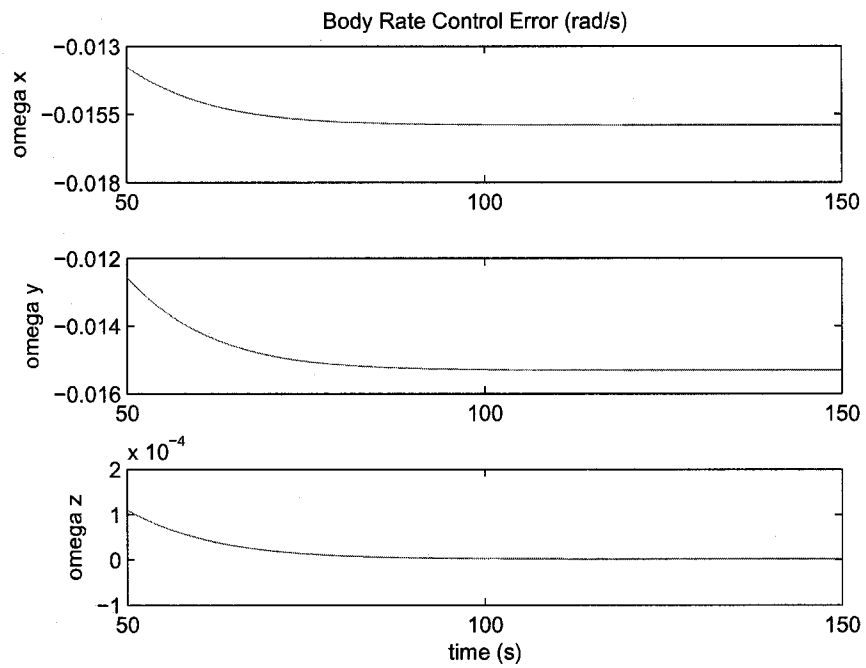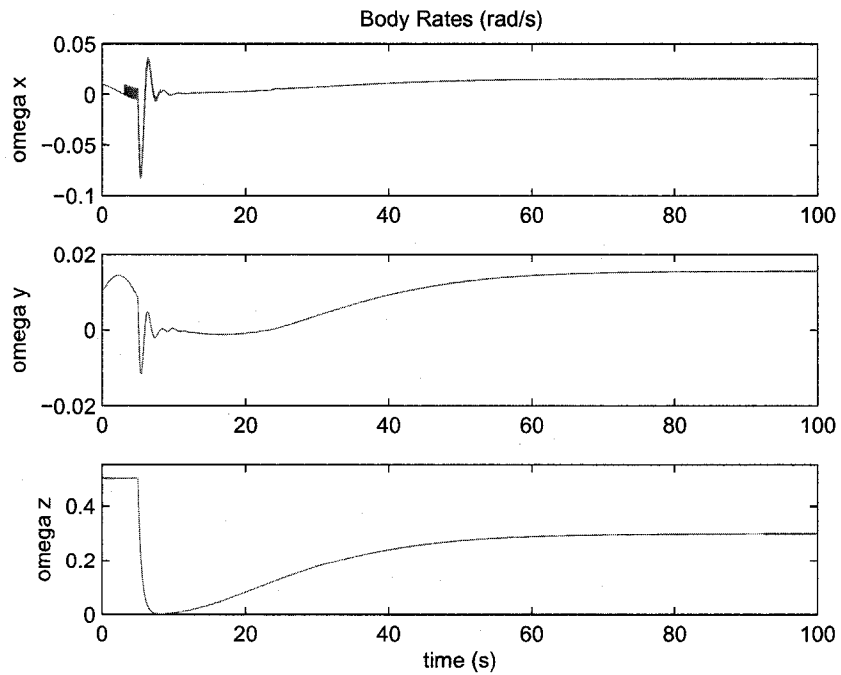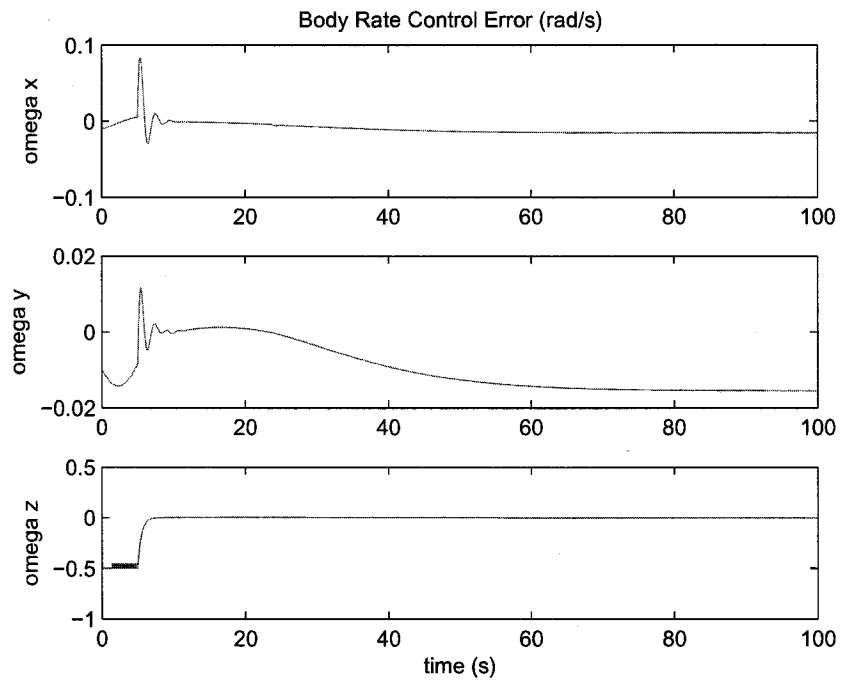
Figure 7-7: Magnified Body Rate Error Using Linear Control
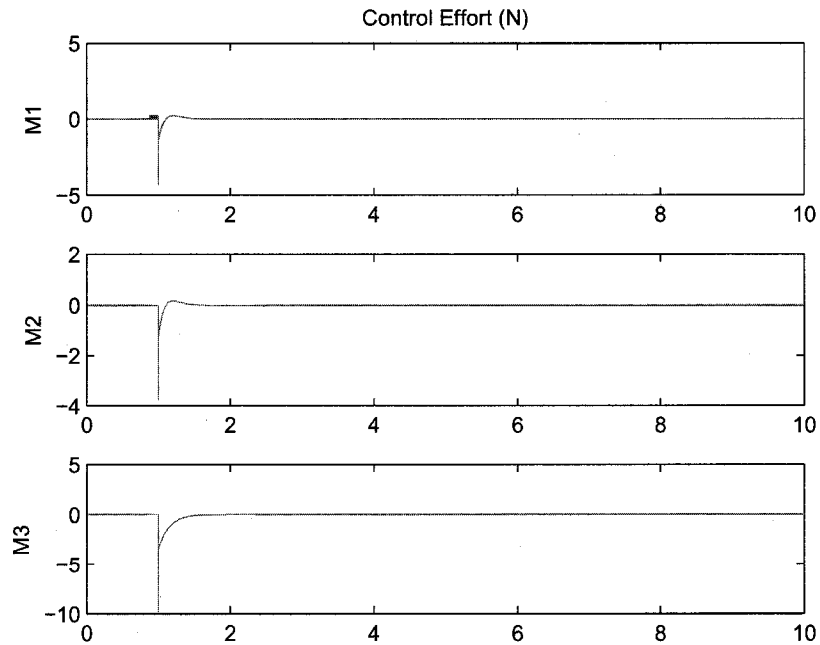
Figure 7-8: Linear Control Effort for Perfect Measurements

## 7.2 Sliding Mode Control

The second control technique investigated is the Sliding Mode Controller (SMC). SMC is a nonlinear control technique similar to the SMO developed in Chapter 6 in that it uses a sliding surface and feedback gains to ensure that the error trajectory converges to zero. Multiple different sliding surfaces can be utilized in a SMC, as well as the type of nonlinear switching function used. The SMC design process involves selecting the type of sliding surface, the switching function, feedback gains, and a sliding surface boundary layer. As with linear feedback control, SMC involves multiple design iterations and simulations to tune feedback gains and sliding surfaces to acquire an effective feedback control system.

The Sliding Mode Controller introduced in Chapter 3 is again defined as:

$$\dot{x} = f(x,t) + Bu(t) + H_{smc}\tilde{z} + K_{smc}\mathbf{1}_s \tag{7.5}$$

where the nonlinear equations of motion $f(x,t)$ are defined in Eq. (6.1) and the switching function is dependent upon the boundary layer $\rho$ and is defined as $\mathbf{1}_s = sat(s/\rho)$.

The desired states are defined in Eq. (7.1) and simulation parameters are defined in Table 7.1.

In designing a SMC, as many as five and as few as one sliding surfaces are investigated for control purposes. These sliding surfaces include combinations of error summations, derivatives and integrals to determine the most effective form of variable structure control. The selection of the sliding surfaces influenced the performance of the observer more then other design parameters. Five sliding surfaces are selected and defined as:

$$s_i = \lambda_1 \tilde{z}_i + \lambda_2 \int \tilde{z}_i dt, \qquad i = 1,2,3,4,5 \tag{7.6}$$

where $\tilde{z}_i$ is the error between actual and desired states. During the sliding surface
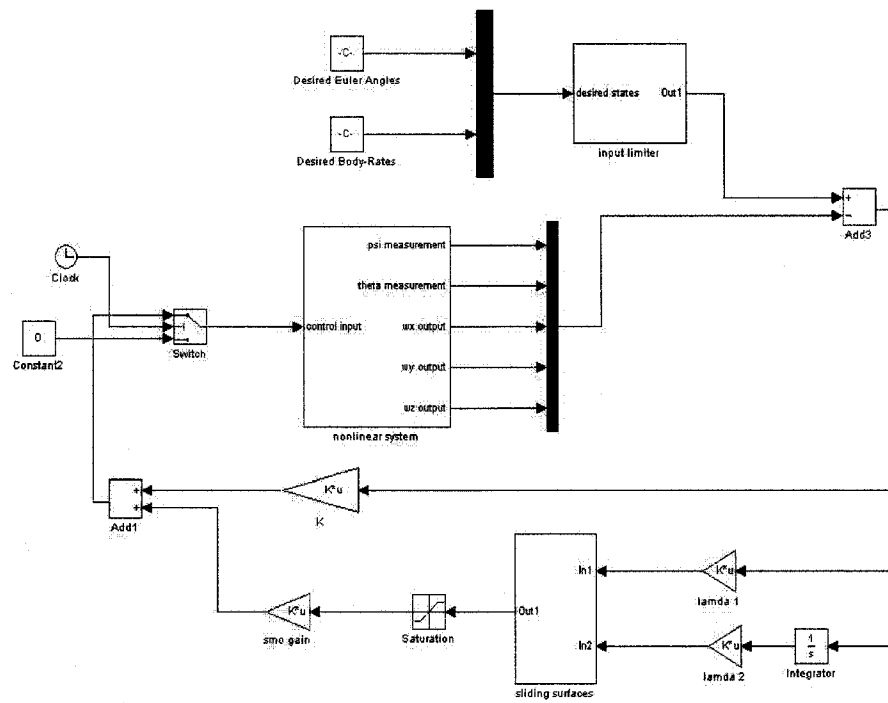
Figure 7-9: Sliding Mode Control Simulation Diagram

selection process, weighting factors $\lambda_1 = 1$ and $\lambda_2 = 0.5$ are also determined to affect the overall influence of these error signals on the control signal. As the number of sliding surfaces increase, as does the size of the gain matrix $K$. To ease in the selection of matrix elements, matrices are partitioned and to assist in gain selection and then tuned through trial and error as with estimator and control gain tuning. Design criteria for control gain selection involved control effort, transient response, and steady-state tracking ability of desired commands. The two gain matrices and boundary layer are defined as:

$$H_{smc} = \begin{bmatrix} 10 & 0 & 2 & 0 & 0 \\ 0 & 10 & 0 & 2 & 0 \\ 0 & 0 & 0 & 0 & 2 \end{bmatrix}, \quad K_{smc} = \begin{bmatrix} 0.05 & 0 & 0.001 & 0 & 0 \\ 0 & 0.05 & 0 & 0.001 & 0 \\ 0 & 0 & 0 & 0 & 0.001 \end{bmatrix}, \quad \rho = 0.01$$

$$(7.7)$$
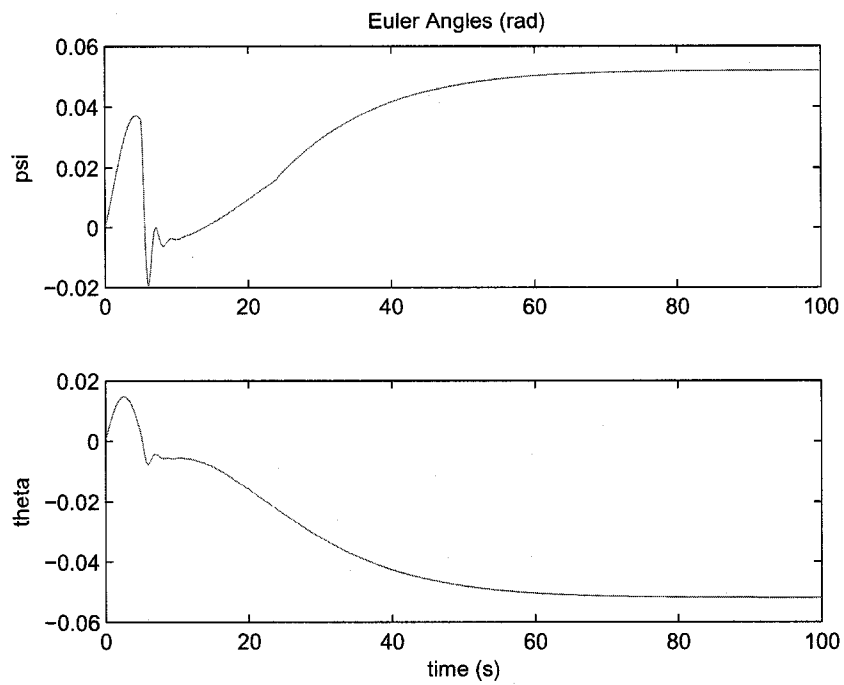
Figure 7-10: Sliding Mode Control Euler Angles

The simulation diagram for Sliding Mode Control with perfect state measurements can be seen in Figure 7-9.

Euler Angle Control Error (rad)
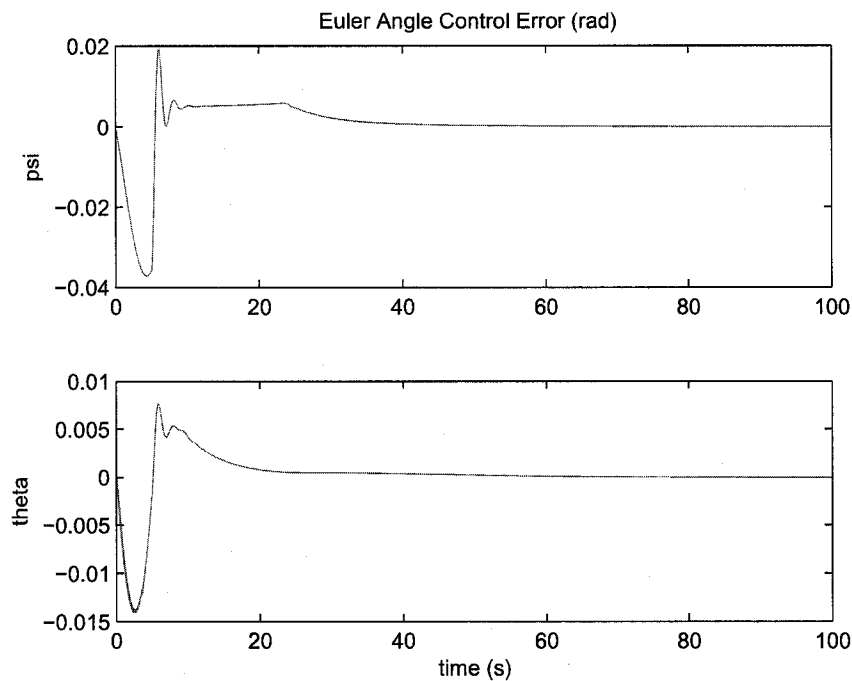


Figure 7-11: Euler Angle Error Using Sliding Mode Control

Euler angle control results are presented in Figures 7-10 and 7-11. It can be seen that the steady state error is essentially zero, which cannot be said for linear control results. There is however a slight overshoot and oscillation before the controller begins to track the command signals. Results for body rate control are presented in Figures 7-13 and 7-15. The transient response shows increased oscillation but a reduction in initial response of the system. The steady-state error could not be reduced and remains similar to that of the linear control. Control effort shown in Figure 7-16 is significantly reduced when compared to linear feedback control. All simulation diagrams and code can be found in Appendix B.

Both linear and sliding mode controllers produce results that meet NASA design requirements for attitude and nutation control. In the next chapter these controllers are updated with nonlinear observers to obtain an effective observer based control system as it applies to the NASA MMS satellite.
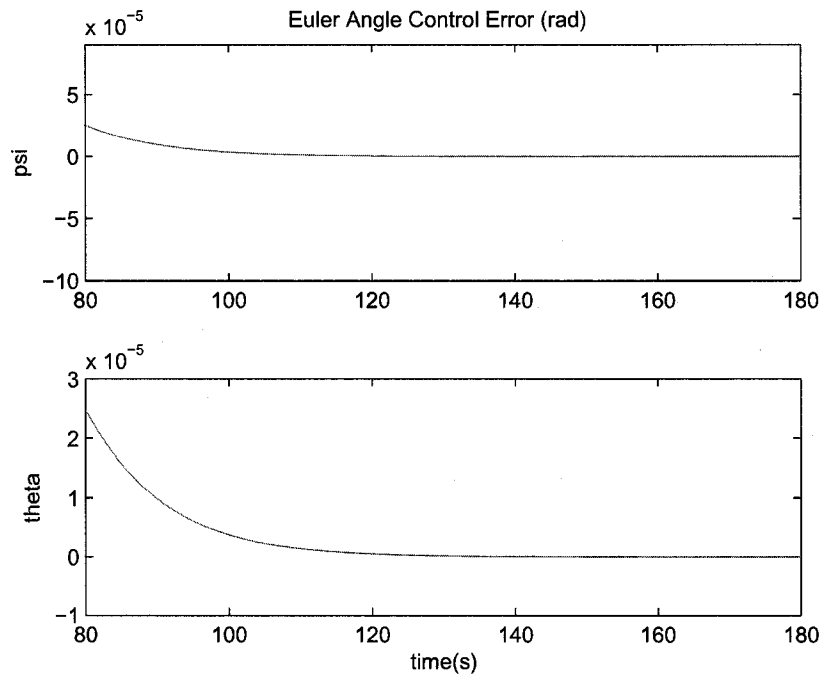
Figure 7-12: Magnified Euler Angle Error Using Sliding Mode Control



Figure 7-13: Sliding Mode Control Body Rates

Figure 7-14: Body Rate Error Using Sliding Mode Control
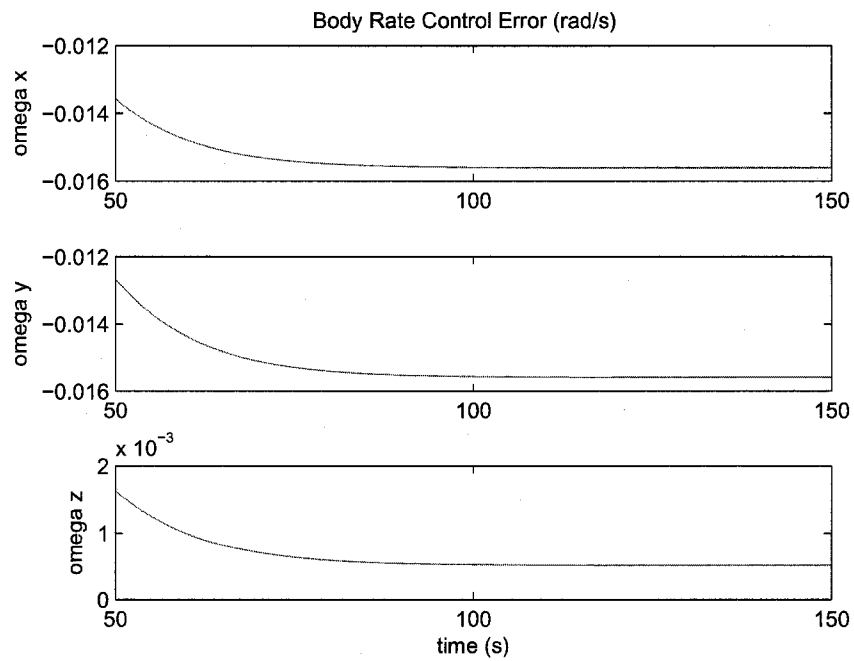


Figure 7-15: Magnified Body Rate Error Using Sliding Mode Control
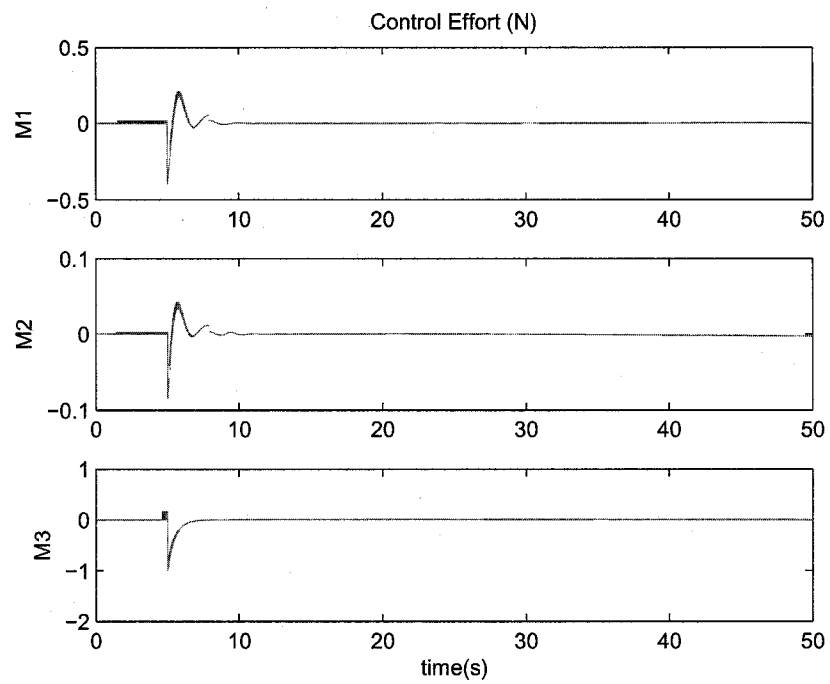
Figure 7-16: Sliding Mode Control Effort for Perfect Measurements

# CHAPTER 8

# OBSERVER BASED CONTROL RESULTS

The next step in attitude control is augmentation of the nonlinear and linear control systems with estimation algorithms. First, the sliding mode observer is tested with the linear feedback controller, as well with the Sliding Mode Controller, to determine observer effectiveness as it applies to attitude control. It is in this step, that the practicality and effectiveness of the overall observer-based control systems is determined as it applies to attitude and nutation control without the use of rate sensors. For all simulations, the control sequence is initialized only after the observer state estimates are allowed to converge to actual state values. Otherwise, the controller would be updated using inaccurate state estimates, possibly causing spacecraft instability.

Since estimates are used in the feedback control system, exact measurements are not available and the desired trajectories for the control system are defined as:

$$\hat{x}_{des} = \begin{bmatrix} \hat{\psi}_{des} \\ \hat{\theta}_{des} \\ \hat{\omega}_{xdes} \\ \hat{\omega}_{ydes} \\ \hat{\omega}_{zdes} \end{bmatrix} = \begin{bmatrix} 0.052 \\ 0.052 \\ 0 \\ 0 \\ 0.03 \end{bmatrix} (rad, rad/s) \tag{8.1}$$

The following sections present analysis on the Sliding Mode Observer and Extended Kalman Filter that are implemented with linear and nonlinear feedback control techniques.

## 8.1 Sliding Mode Observer

The Sliding Mode Observer designed in Chapter 6 is first augmented with the linear feedback controller, followed by the Sliding Mode Control technique. The control sequence commences after 15 seconds of simulation time to allow the SMO to effectively acquire accurate state estimates. Table 8.1 shows the estimation and control simulation parameters used for feedback control design and analysis.

A zero mean Gaussian white noise is used to corrupt Euler Angle measurements of $\pm 1.5$ $rad$ and a disturbance torque of $M_{x,y,z} = 0.001 sin(0.3t)$ $Nm$ was used to simulate unknown moments acting on the spacecraft. Euler angle measurement noise particularly diminishes results because the magnitude of the noise used in estimation design is of the same magnitude as that of the desired satellite orientation. This means that the Euler angle estimation signals are completely embedded in measurement noise, making accurate control difficult. Simulations are presented with measurement noise to illustrate system stability and robustness. NASA is to supply measurement models or known measurement noise bounds for control testing in future research.

| | Actual System | Observer |
|---|---|---|
| I.C.: $\psi, \theta, \phi$ $(rad)$ | 0, 0, 0 | 0, 0, 0 |
| I.C.: $\omega_x, \omega_y, \omega_z$ $(rad/s)$ | 0.01, 0.01, 0.5 | 0,0,0 |
| Inertia Matrix $(kg \cdot m^2)$ | $\begin{bmatrix} 8402.64 & -58.8 & -44.6 \\ -58.8 & 8411.97 & -100 \\ -44.66 & -100 & 16414.66 \end{bmatrix}$ | $\begin{bmatrix} 8000 & 0 & 0 \\ 0 & 8600 & 0 \\ 0 & 0 & 17500 \end{bmatrix}$ |
| Noise bounds $(rad)$ | $\pm 0.03$ | |

Table 8.1: Simulation Parameters for the SMO with Feedback Control

Since the overall goal of this system is to use estimates to control actual satellite dynamics, it is the observation of the actual satellite dynamics that are compared to design requirements to determine control effectiveness. Also, the ability of the observer to estimate these states under control influences are evaluated.

### 8.1.1 SMO Based Linear Control

Results for linear control of satellite attitude and nutation using sliding mode estimates are shown in Figures 8-1 and 8-2 while body-rate control results are illustrated in Figures 8-3 and 8-4.

From Figures 8-2 it can be seen that the satellite attitude error is reasonable at only about 0.001 rad and 0.002 rad for the $\psi$ and $\theta$ Euler angles, respectively, as well as the constant z-axis spin error of approximately 0.0001 rad/s. The most obvious problem is the steady-state error and transient control demand that occur mainly in the $x$ and $y$ body rates as seen in Figure 8-3. The steady-state nutation error is approximately 0.016 rads/s on both the $\omega_x$ and $\omega_y$ axis while the transient peak error is -0.05 and -0.02 rads/s respectively.

There is also error oscillation in the Euler Angles that can be seen in Figure 8-5. This error occurs from the disturbance torques that corrupts the x,y and z axis and the inability of the observer to track these very small oscillations. Thus, the control algorithm does not know they exist and is unable to compensate.

Actual and Estimated Euler Angles (rad)
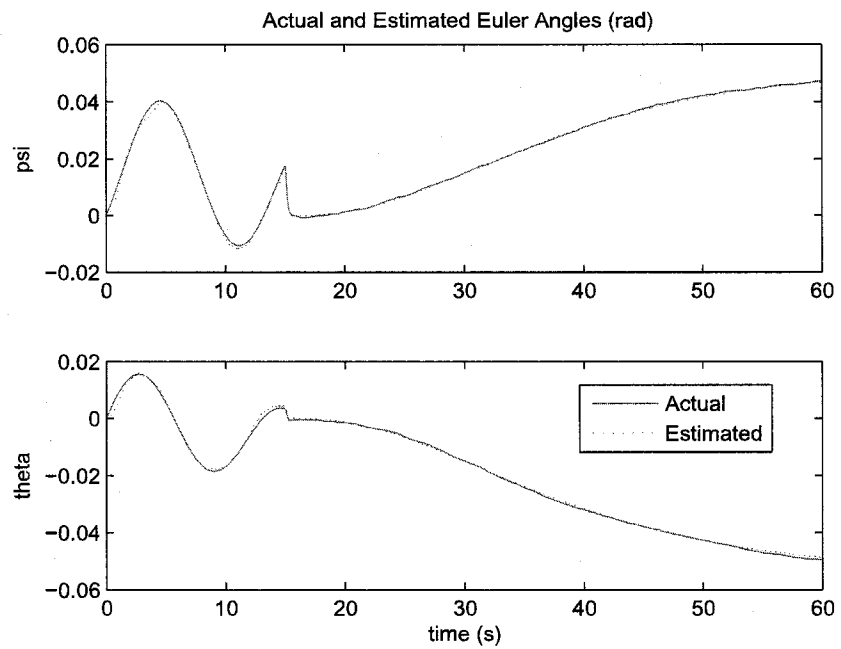


Figure 8-1: SMO-Based Linear Controller: Actual and Estimated Satellite Attitude

Euler Angle Control Error (rad)
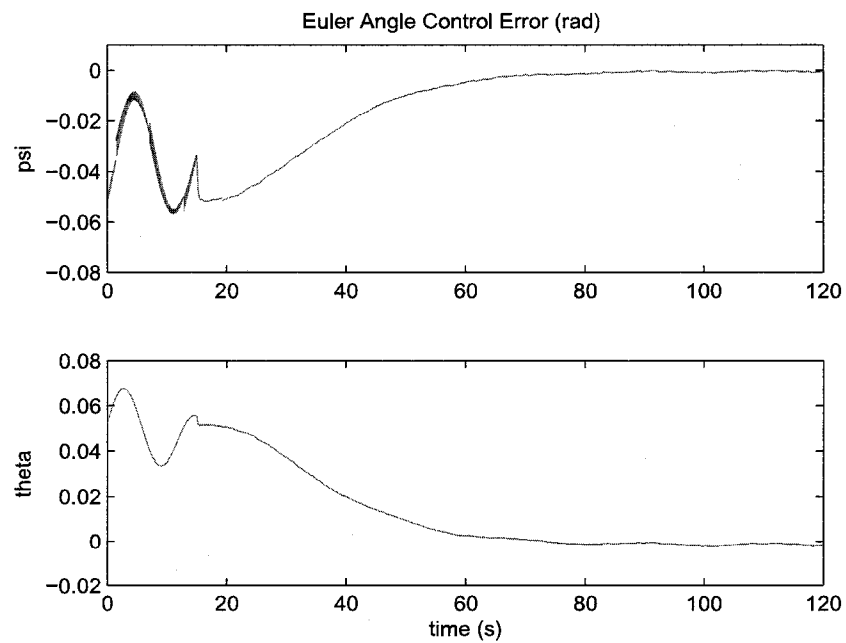


Figure 8-2: SMO-Based Linear Controller: Euler Angle Control Error
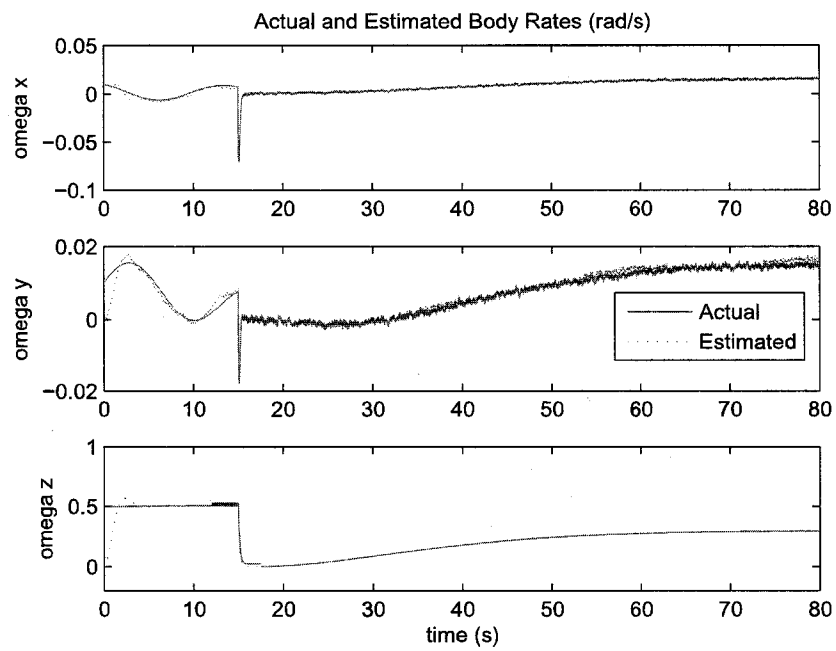
Figure 8-3: SMO-Based Linear Controller: Actual and Estimated Satellite Body Rates
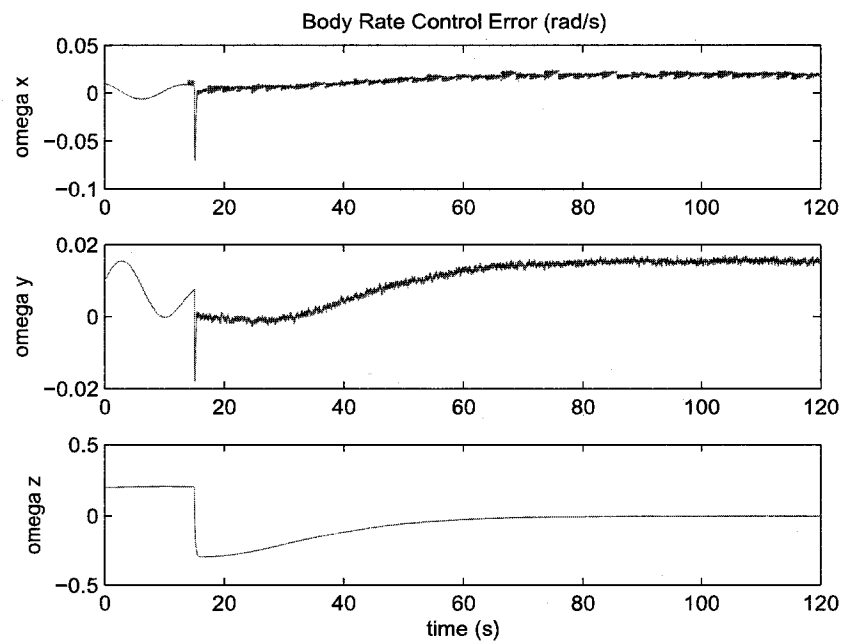


Figure 8-4: SMO-Based Linear Controller: Body Rate Control Error
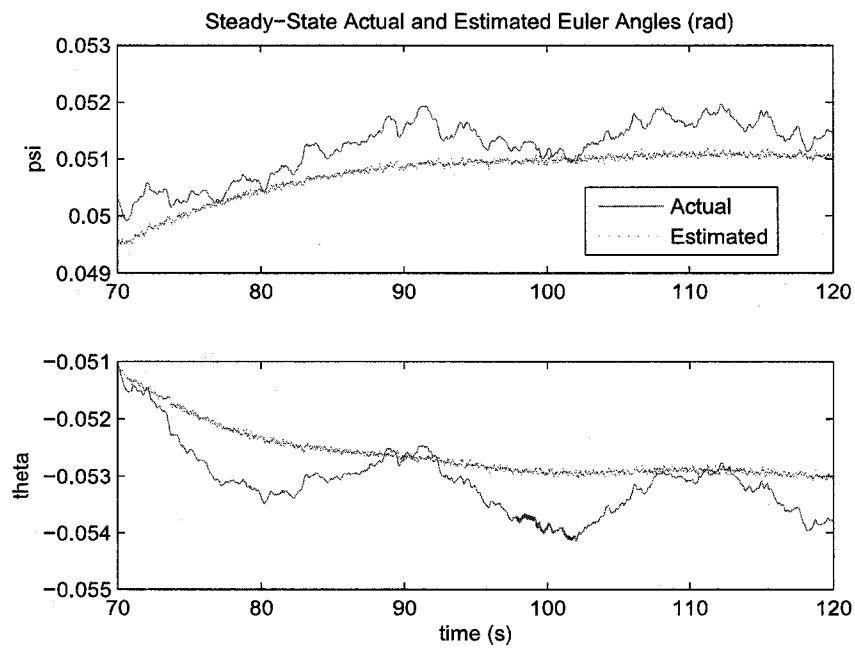
Figure 8-5: SMO-Based Linear Controller: Actual and Estimated Steady-State Euler Angles
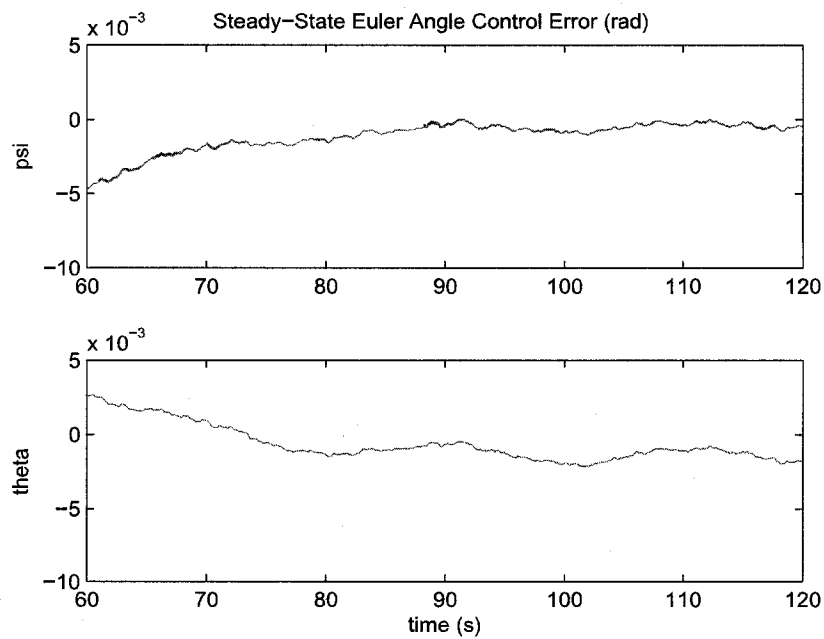


Figure 8-6: SMO-Based Linear Controller: Steady-State Euler Angle Control Error
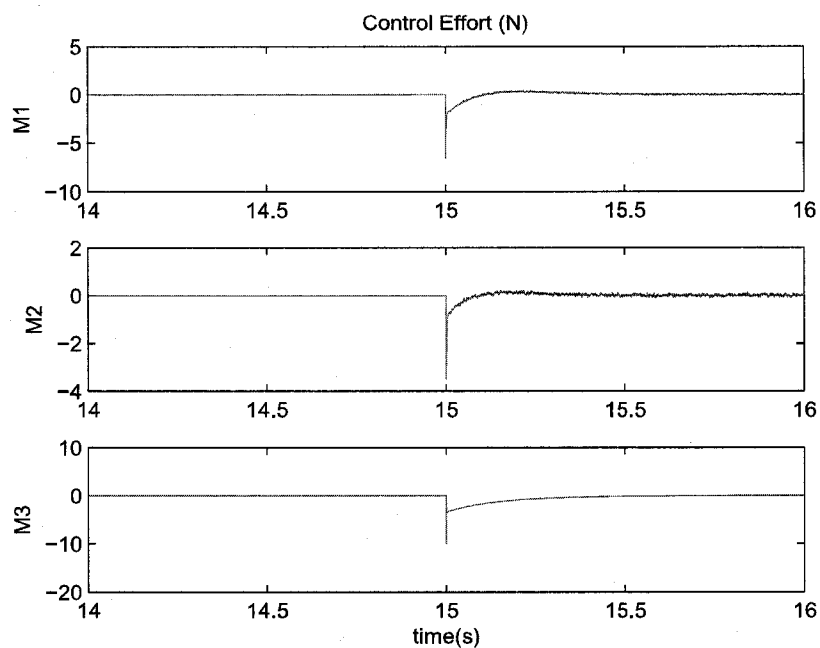
**Control Effort (N)**



Figure 8-7: SMO-Based Linear Control Effort

It can be seen from the results that the nutation control is the limiting factor in this control sequence. Both x and y body rates have a steady state error of 0.015 rad/s (or 0.917 deg/s), which is nearly the same error experienced during control design, assuming perfect Euler angle measurements. This is a strong indication that the system is limited by the controller, rather then the accuracy of the observed states. Despite the steady-state error, it is only during the brief transient error in which design requirements are violated. All states fall well within error requirements, except for the x and y body rates that are only within 0.005 rad/s of acceptable errors. Control effort can be seen in Figure 8-7, in which the control commands have a large transient demand. Although the control command does not saturate the thrusters at 10 Newtons, it is not desirable to have such a large response for the MMS mission.

Tables 8.2 and 8.3 show the steady-state Euler angle and body rate control error respectively. Maximum percent errors between estimated and desired states are also

| | $\psi$ | $\theta$ |
|---|---|---|
| Steady-State Error $(rad)$ | 0.0005 | -0.0005 |
| Percent Error | 1.9 | 3.6 |

Table 8.2: Steady-State SMO-Based Linear Controller: Euler Angle Control Errors

| | $\omega_x$ | $\omega_y$ | $\omega_z$ |
|---|---|---|---|
| Steady-State Error $(rad/s)$ | 0.015 | 0.015 | $\pm0.001$ |
| Percent Error | - | - | 0.36 |

Table 8.3: Steady-State SMO-Based Linear Controller: Body Rate Control Errors

presented to illustrate the effectiveness of the observer-based control system to track desired commands with estimated signals.

## 8.1.2 SMO Based Sliding Mode Control

The Sliding Mode Observer was next implemented with a Sliding Mode Controller. As with the linear feedback control system, the control commands engage the system at 15 seconds of simulation time to allow the SMO to acquire accurate state estimates. The Sliding Mode Controller designed in Chapter 7 assumed perfect measurements. Now the SMO estimates are used to update the SMC to investigate the effectiveness of observer-based attitude and nutation control without rate sensors. Feedback gains, sliding surfaces and boundary layers are defined in Eqs. (7.6) and (7.7) while simulation parameters are listed in Table 8.1.

Euler angle estimation and control results are shown in Figures 8-8 and 8-9. Steady-state control errors for attitude control are listed in Table 8.5. From first inspection it can be seen that although the Sliding Mode Control does not contain derivative control, noise levels are amplified upon control commencement. Figure 8-10 shows that the SMO is effective at tracking the attitude signals despite high levels
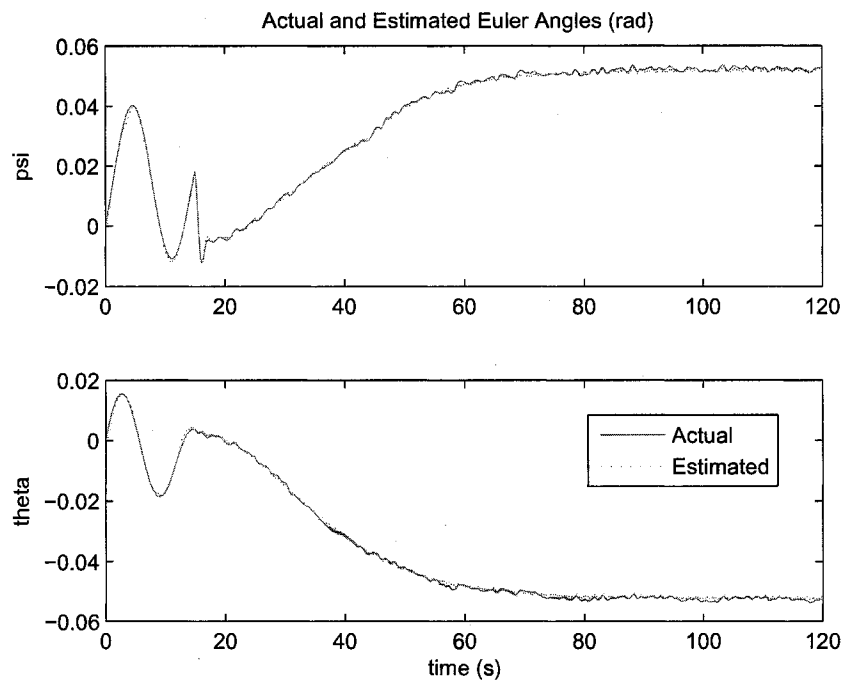
Figure 8-8: SMO-Based SMC: Actual and Estimated Satellite Attitude

of noise and that the mean steady-state orientation is desirable (0.052 rad and -0.052 rad for the $\psi$ and $\theta$ Euler angles, respectively).

Body rate estimation and control results are shown in Figures 8-11 and 8-12 while the steady-state errors are tabulated in Table 8.4. As with the Euler angle signals, body rate noise is amplified upon activation of the control sequence. Steady-state body rate error remains consistent with other estimation and control techniques shown in Figure 8-13. However, noise amplitude is increased as compared with the SMO based linear control system, while maximum transient errors are decreased. Control effort is vastly improved as compared to SMO-based linear control, in particular, the transient response of the control effort. Figure 8-14 illustrates that the transient control effort is an order of magnitude smaller, while the settling time is increased as well to limit flexible boom responses.

The implementation of the same SMC system with EKF estimates are necessary to
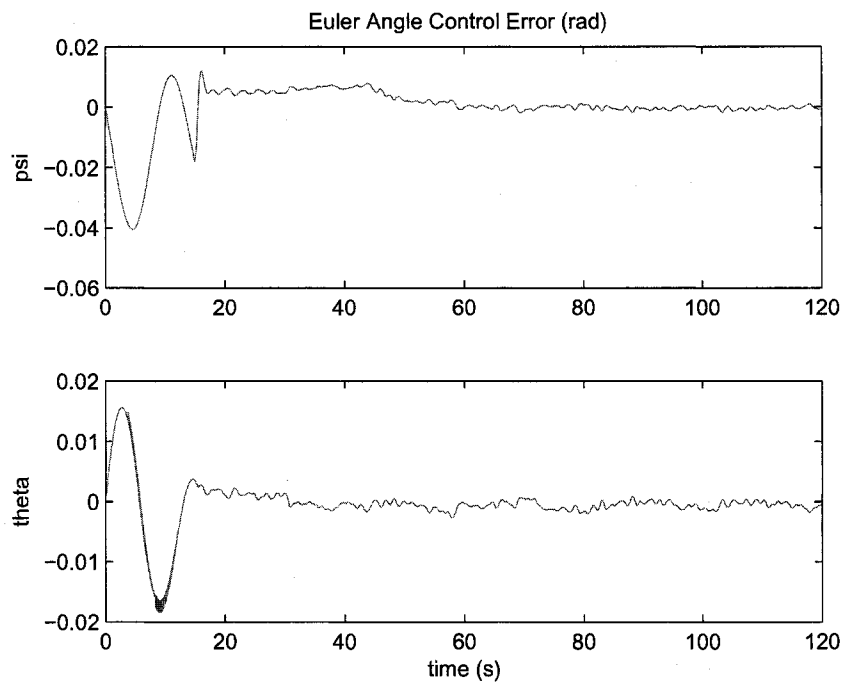
Figure 8-9: SMO-Based SMC: Euler Angle Control Error
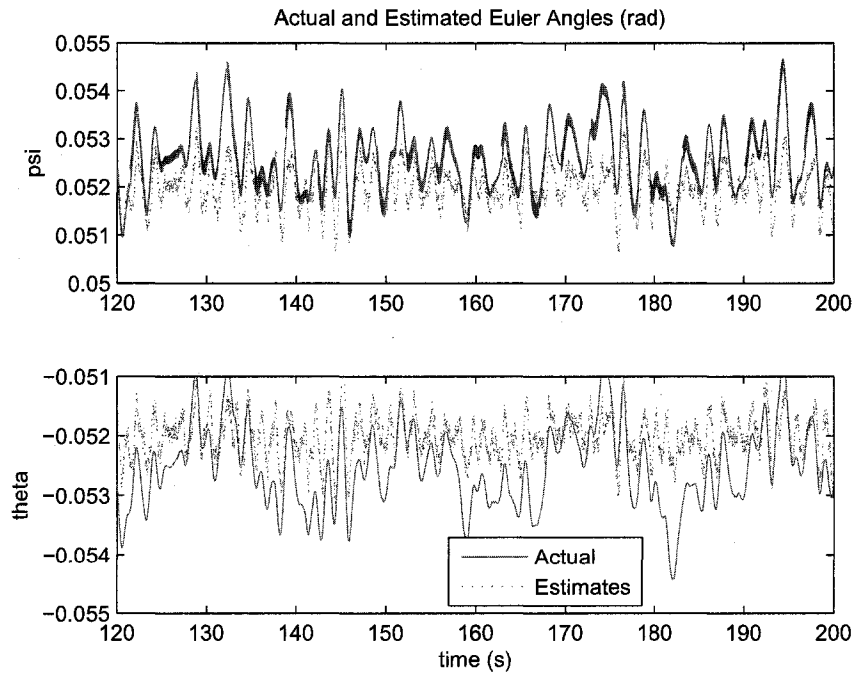


Figure 8-10: SMO-Based SMC: Steady-State Euler Angles
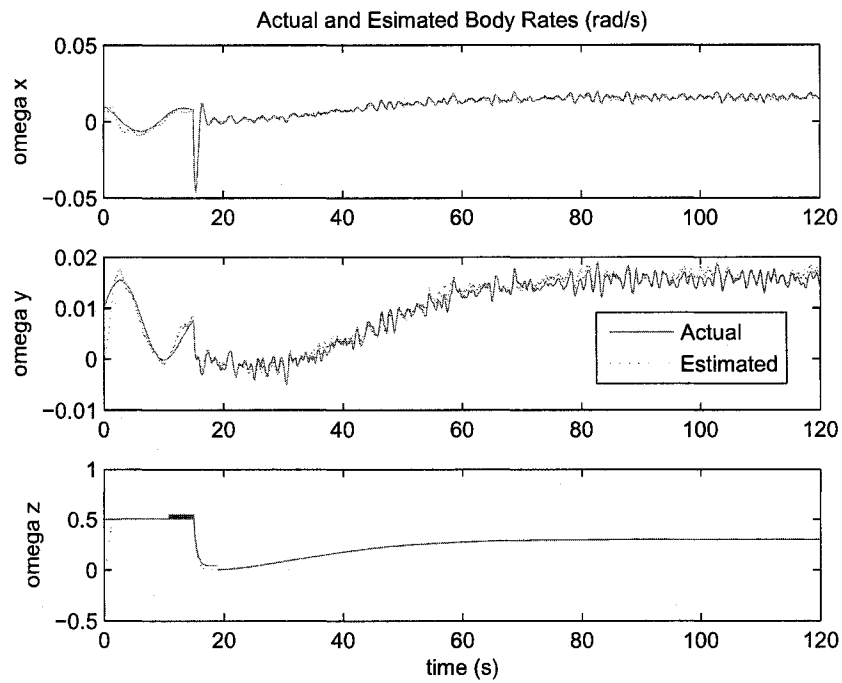
Figure 8-11: SMO-Based SMC: Actual and Estimated Satellite Body Rates
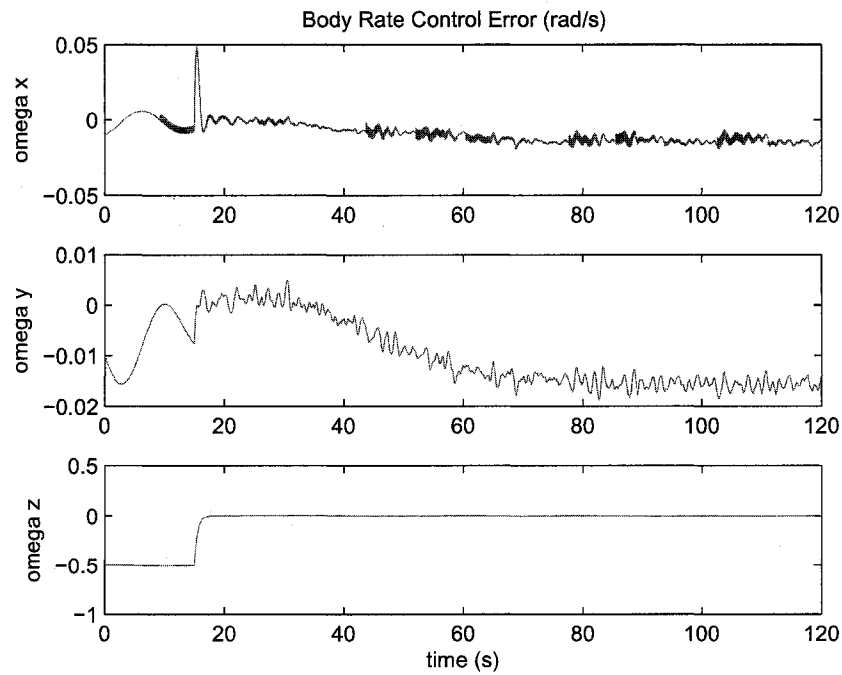


Figure 8-12: SMO-Based SMC: Body Rate Control Error
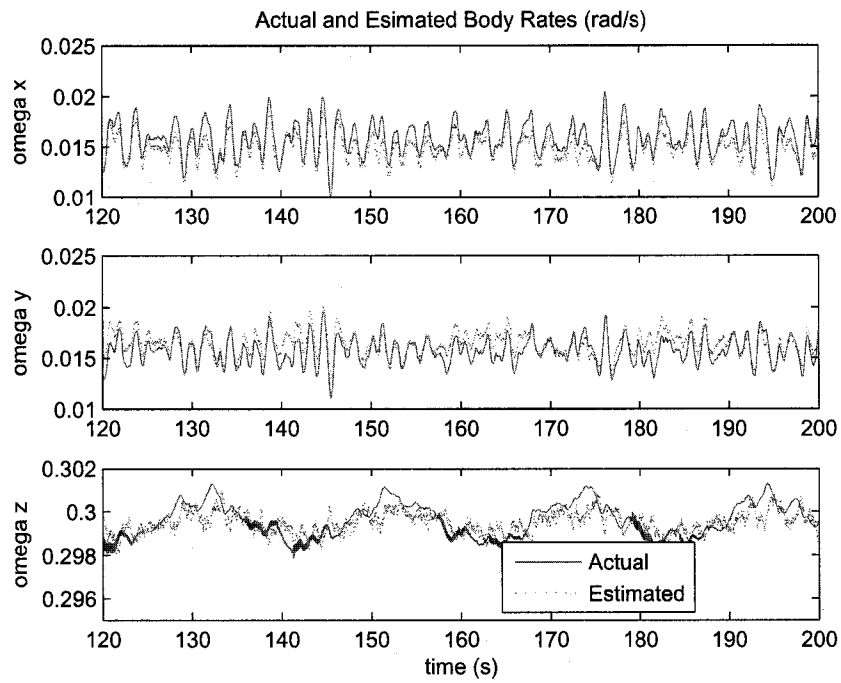
Figure 8-13: SMO-Based SMC: Steady-State Body Rates
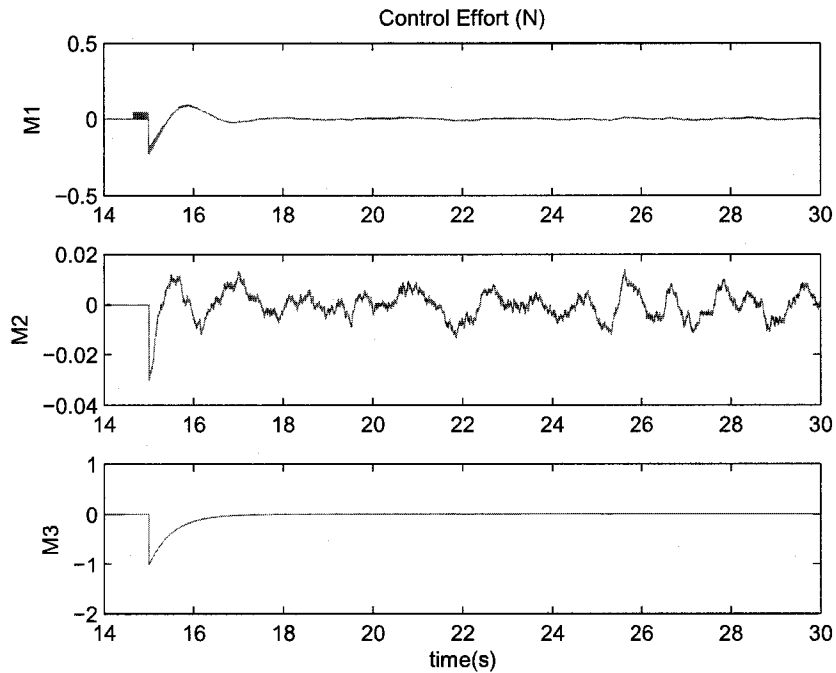


Figure 8-14: SMO-Based SMC Effort

|  | $\omega_x$ | $\omega_y$ | $\omega_z$ |
|---|---|---|---|
| Steady-State Error $(rad/s)$ | 0.015 | 0.015 | ±0.002 |
| Percent Error | - | - | 0.5 |

Table 8.4: Steady-State SMO-Based SMC: Body Rate Control Errors

|  | $\psi$ | $\theta$ |
|---|---|---|
| Steady-State Error $(rads)$ | ± 0.001 | ± 0.0011 |
| Percent Error | 3.2 | 4.3 |

Table 8.5: Steady-State SMO-Based SMC: Euler Angle Control Errors

investigate the performance potential of the Sliding Mode Control. It is necessary to keep noise levels to a minimum while maintaining desired steady-state characteristics, which the SMC effectively provides during perfect measurement design. All MATLAB simulation diagrams and code can be found in Appendix B.

## 8.2 Extended Kalman Filter Estimates

Controllers tested on Sliding Mode Observer estimates are implemented using estimates produced by the EKF. Exact controllers are used on both observers to determine their effectiveness relative to each other before any further gain tuning or signal conditioning occurrs. Simulation parameters for the controller and observers can be seen in Table 8.6

Since the time for the EKF to begin tracking satellite states is slightly longer then that of the SMO, the control sequenced commenced after 40 seconds of simulation time. Also similar to the SMO with feedback control, is the 10 percent parametric uncertainty in inertia values, as well as unknown disturbance torques of $M = 0.001sin(0.3t)$ $Nm$ and measurement noise of ± 0.03 $rad$. The same third

order filter in Eq.(7.4) is also utilized to limit input commands.

The following sections present results of Extended Kalman Filter estimates used in a linear and nonlinear feedback control system. All MATLAB simulation diagrams and code can be found in Appendix B.

| | Actual System | Observer |
|---|---|---|
| I.C.: $\psi, \theta, \phi$ $(rad)$ | 0, 0, 0 | 0, 0, 0 |
| I.C.: $\omega_x, \omega_y, \omega_z$ $(rad/s)$ | 0.01, 0.01, 0.5 | 0,0,0 |
| Inertia Matrix $(kg \cdot m^2)$ | $\begin{bmatrix} 8402.64 & -58.8 & -44.6 \\ -58.8 & 8411.97 & -100 \\ -44.66 & -100 & 16414.66 \end{bmatrix}$ | $\begin{bmatrix} 8000 & 0 & 0 \\ 0 & 8600 & 0 \\ 0 & 0 & 17500 \end{bmatrix}$ |

Table 8.6: Simulation Parameters for the EKF with Feedback Control

## 8.2.1 EKF Based Linear Control

The same linear controller that is designed assuming perfect Euler Angle measurements, is implemented with the EKF designed and presented in Chapter 6. The overall system is evaluated to determine its effectiveness at maintaining satellite orientation and body rates.
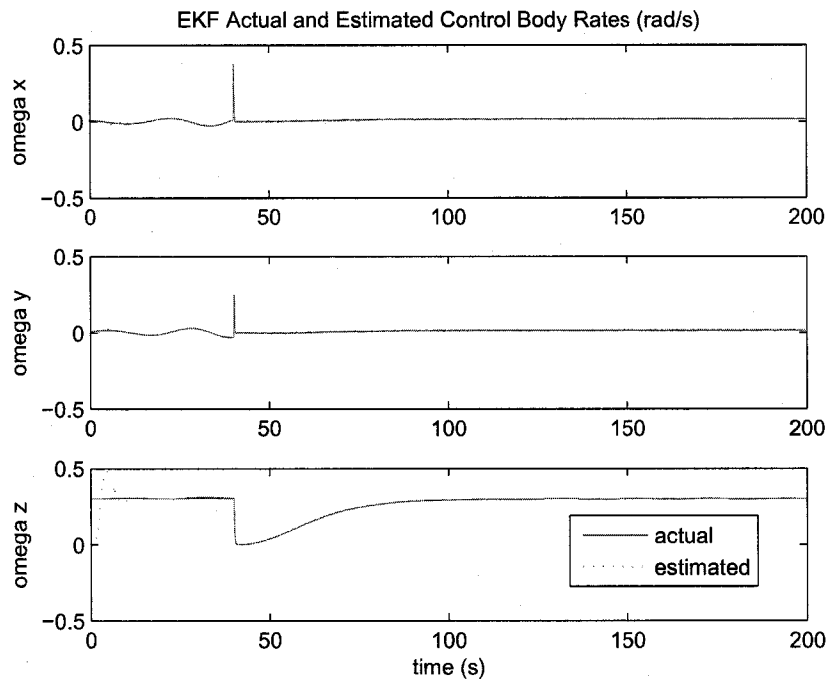
Figure 8-15: EKF-Based Linear Controller: Actual and Estimated Body Rates
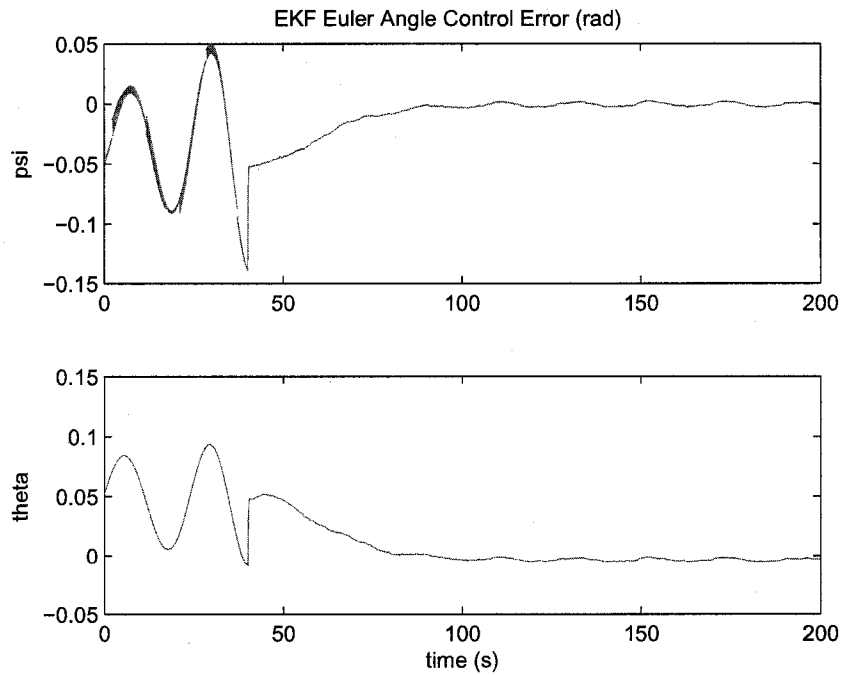


Figure 8-16: EKF-Based Linear Controller: Body-Rate Control Error

EKF Actual and Estimated Control Euler Angles (rad)
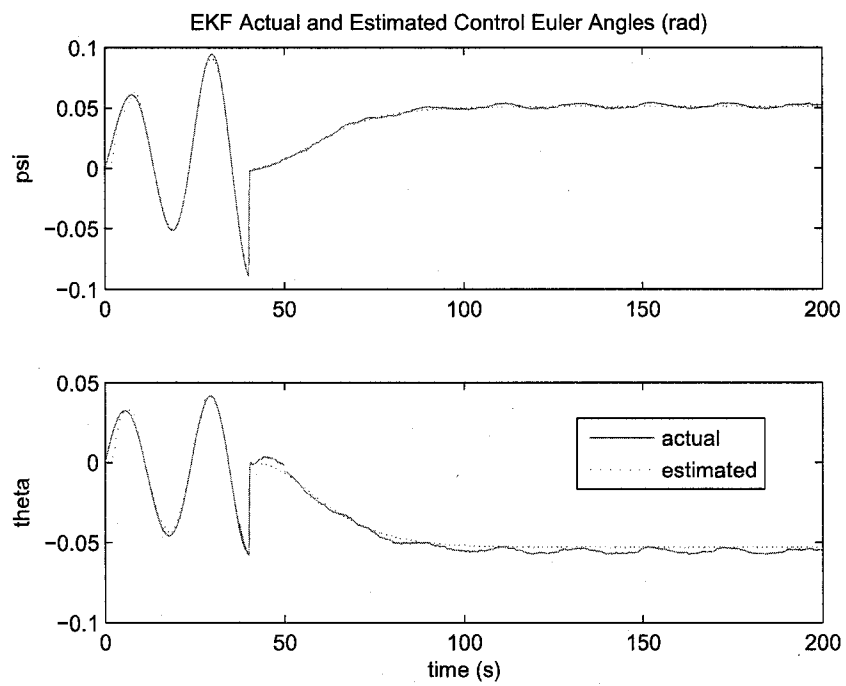
Figure 8-17: EKF-Based Linear Controller: Actual and Estimated Euler Angles

EKF Body Rate Control Error (rad/s)
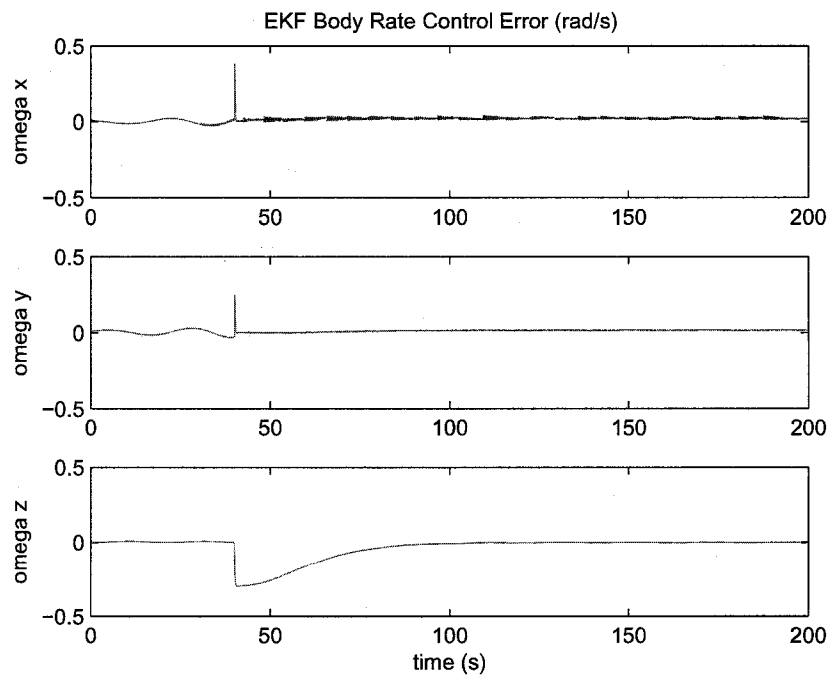
Figure 8-18: EKF-Based Linear Controller: Euler Angle Control Error

**Steady–State EKF Actual and Estimated Control Euler Angles (rad)**
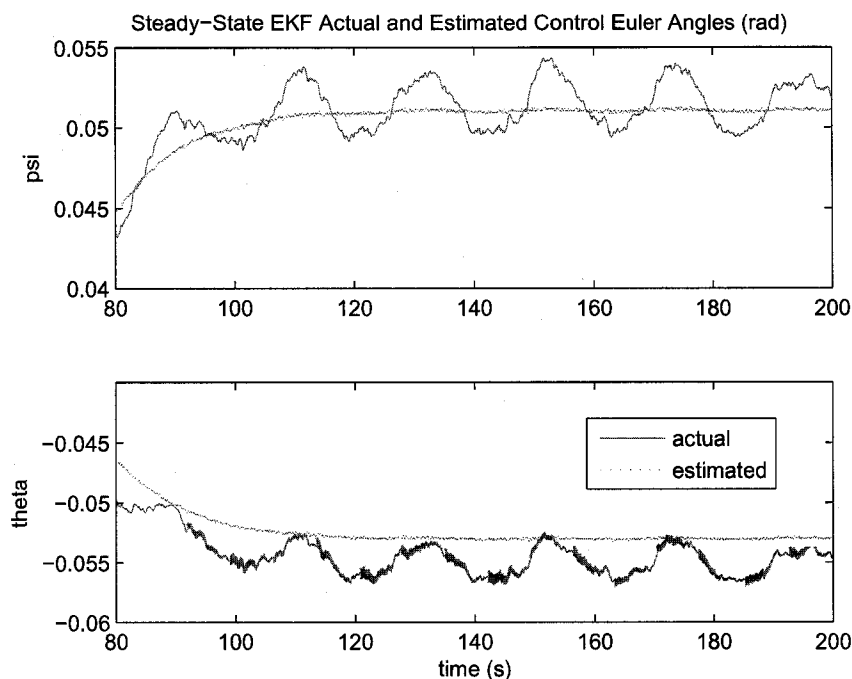
Figure 8-19: EKF-Based Linear Controller: Actual and Estimated Steady-State Euler Angles

Implementation of the proportional and derivative controller immediately shows an obvious problem with using the EKF. Figures 8-15 and 8-16 show a high increase in noise, as a result from the derivative control. The cause for this increase in noise in the EKF, while not present in the SMO despite the fact they have identical noise characteristics, has to do with the how each observer limits the noise. Euler angle control results are presented in Figures 8-17 and 8-18. Similar to the SMO-based linear controller, there is steady-state error, as well as slight Euler angle oscillation. Maximum percent errors and steady-state errors for euler angle and body rate control can be found in Tables 8.7 and 8.8.
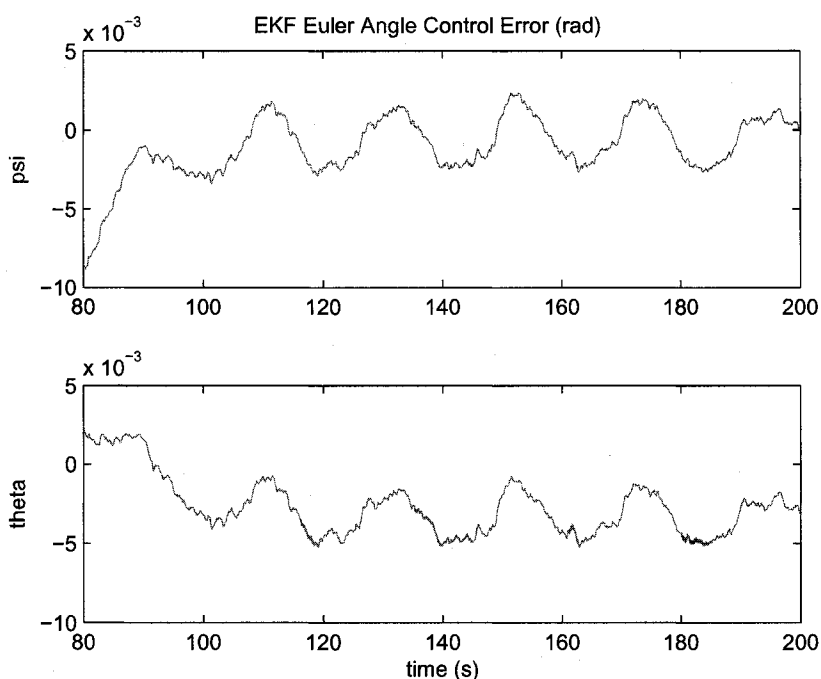
Figure 8-20: EKF-Based Linear Controller: Steady-State Euler Angle Control Error

The main disadvantage of the linear controller using EKF estimates for updates is the derivative control. Differentiation of a signal that contains noise always causes magnification regardless of the estimation or filtering technique, and because the EKF is optimal in the root mean square error sense, it causes even further noise magnification. High transient error and thruster demands is another drawback to using linear feedback control gains. In order to reduce noise that its amplified during the control sequence, low pass filters should be investigated for noise reduction before thruster actuation. Control effort is the major disadvantage of the EKF-based linear control. Figure 8-22 shows that control effort saturates the thrusters, which is unacceptable for MMS application. Related simulation diagrams and code can be found in Appendix B.
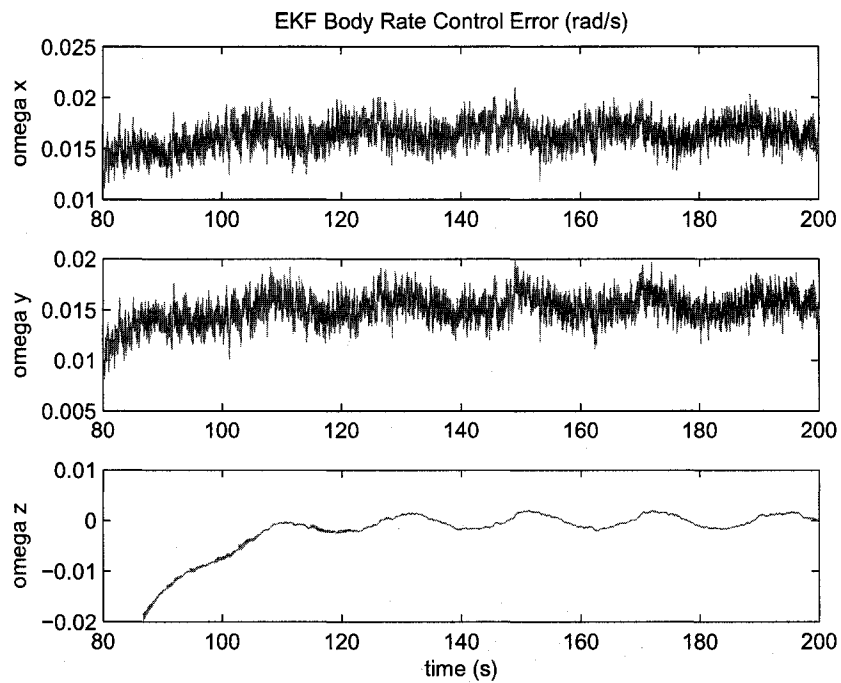
Figure 8-21: EKF-Based Linear Controller: Steady-State Body-Rate Control Error
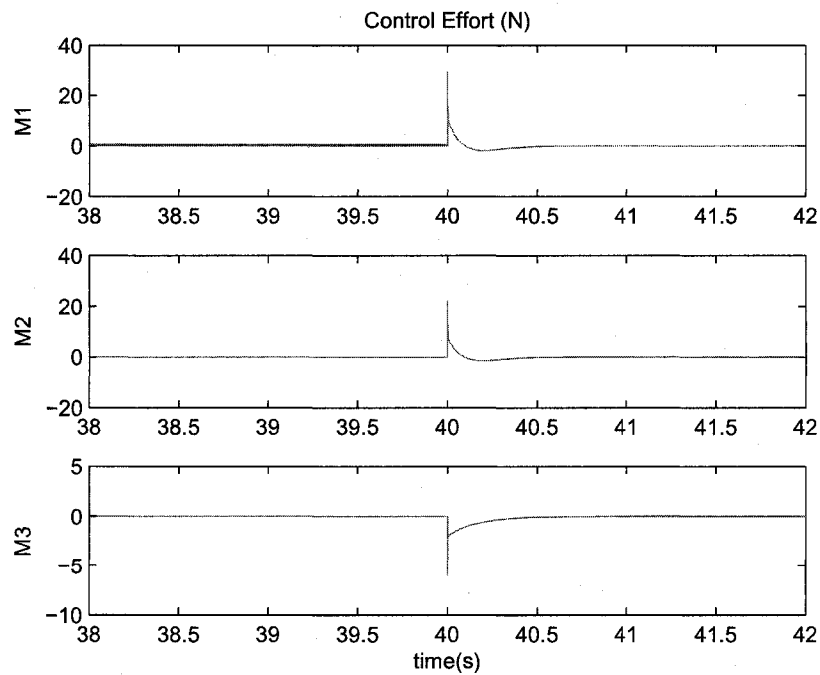


Figure 8-22: EKF-Based Linear Control Effort

| | $\psi$ | $\theta$ |
|---|---|---|
| Steady-State Error $(rad)$ | 0.0009 | 0.004 |
| Percent Error | 1.88 | 7.90 |

Table 8.7: Steady-State EKF-Based Linear Controller: Euler Angles Control Errors

| | $\omega_x$ | $\omega_y$ | $\omega_z$ |
|---|---|---|---|
| Steady-State Error $(rad/s)$ | 0.015 | 0.015 | $\pm$ 0.002 |
| Percent Error | - | - | 0.66 |

Table 8.8: Steady-State EKF-Based Linear Controller: Body Rate Control Errors

## 8.2.2    EKF Based Sliding Mode Control

In this section, the Sliding Mode Control designed assuming perfect measurements are updated with Extended Kalman Filter estimates to attempt to acquire desired attitude and body rate trajectories.

The SMC in consideration takes the form of Eq.7.5 with gains defined in Eq.7.7 and sliding surfaces defined in Eq.7.6. Simulation parameters for the observer and control system can be found in Table 8.6 with the same noise characteristics, unknown disturbances and parametric uncertainties used through-out this research for observer analysis.

Results for Euler angle control can be seen in Figures 8-23 and 8-24. Body rate control results are shown in Figures 8-25 and 8-26 while steady-state and percent errors are listed in Table 8.10 and 8.9.
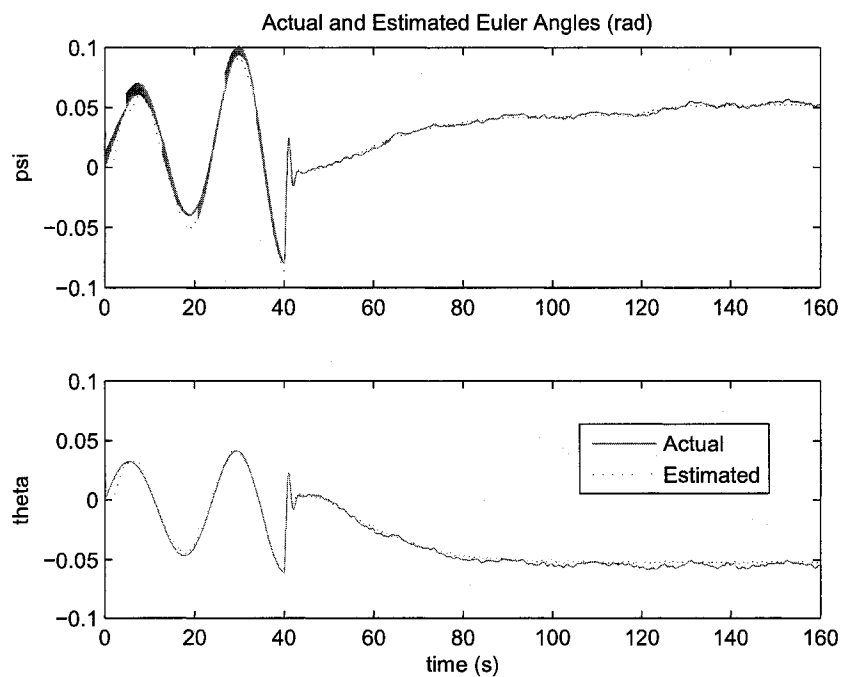


Figure 8-23: EKF-Based SMC: Actual and Estimated Euler Angles
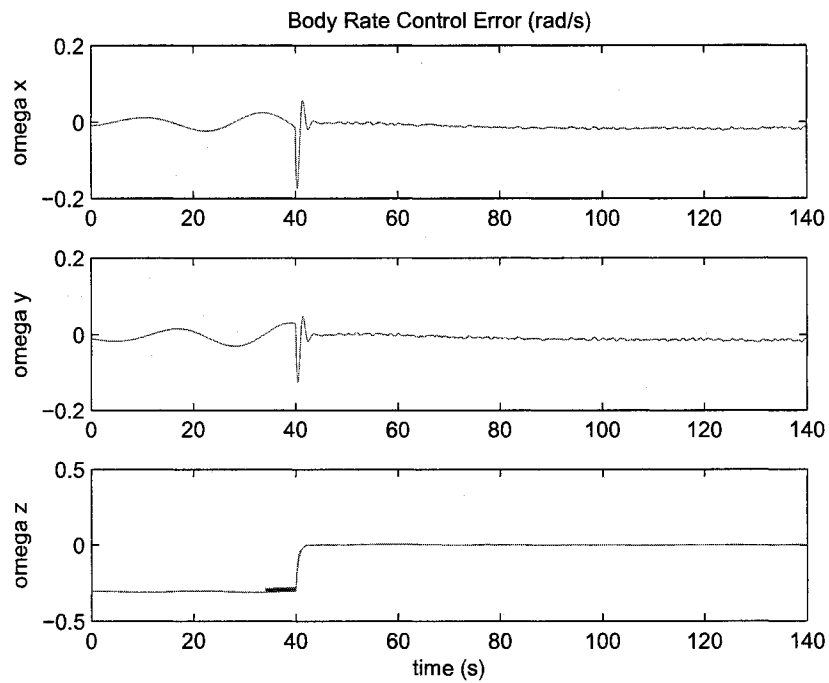
Figure 8-24: EKF-Based SMC: Euler Angle Control Error
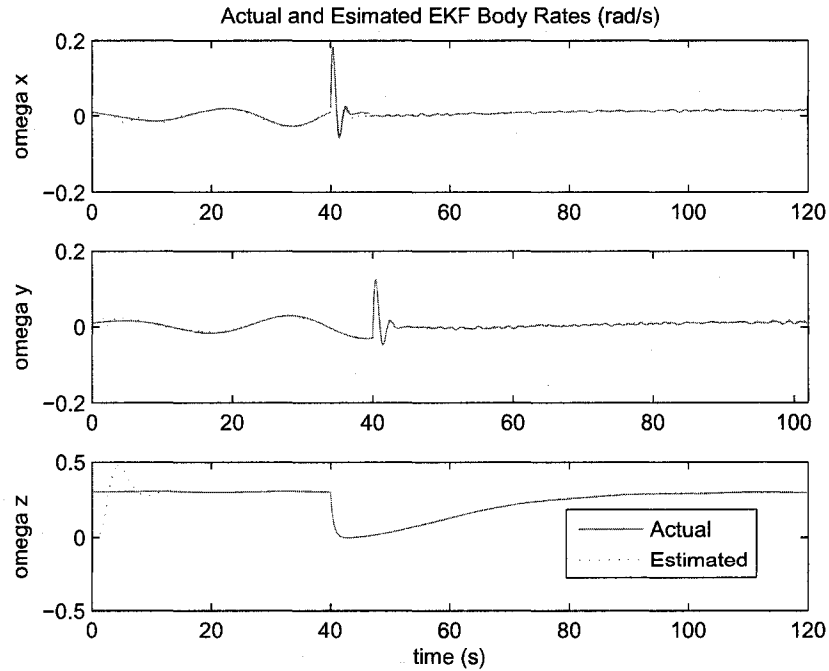


Figure 8-25: EKF-Based SMC: Actual and Estimated Satellite Body Rates
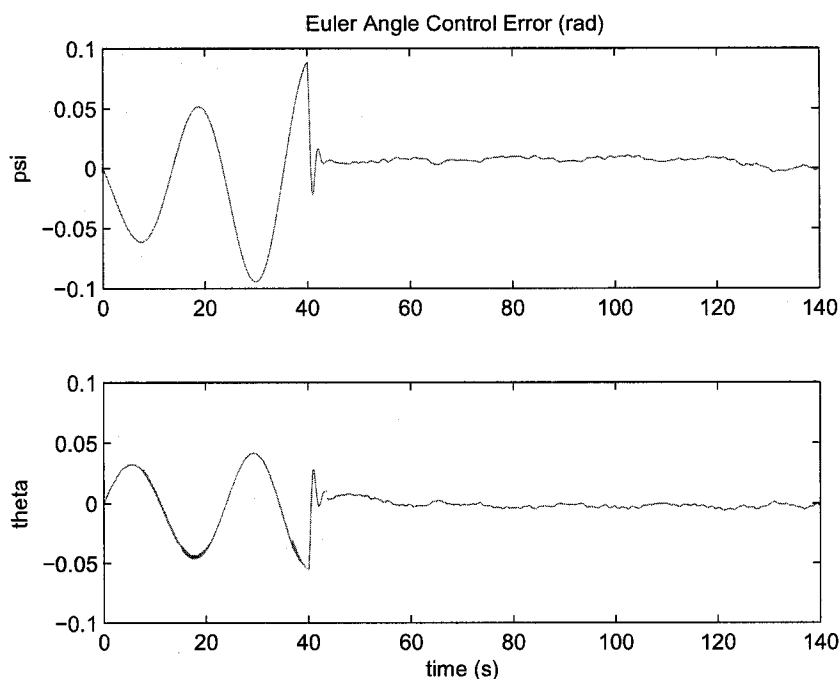
Figure 8-26: EKF-Based SMC: Body Rate Control Error

The average steady-state control error for attitude control is improved significantly over the linear feedback control system as seen in Figure 8-29. Also, since there is no differentiation of the feedback signals, body rate noise is reduced as seen in Figure 8-30. Steady-state body rate control error remains unimproved. However, noise is significantly reduced with the implementation of the SMC. Transient responses of body rate correction is reduced to almost half as compared to linear control, while steady-state oscillations of euler angles are considerably reduced with the implementation of the Sliding Mode Control. The major drawback of the Sliding Mode Control is the excessive oscillations that occur within the first 20 seconds of control operation. These oscillations can cause damage to actuators, as well as excite unknown dynamics in the flexible appendages/booms.
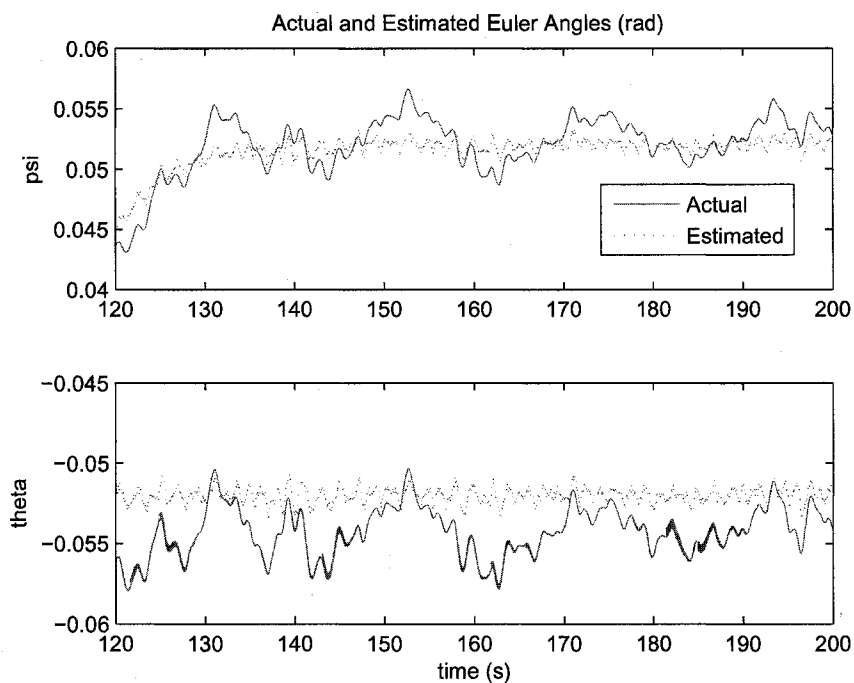
Figure 8-27: EKF-Based SMC: Steady-State Actual and Estimated Euler Angles
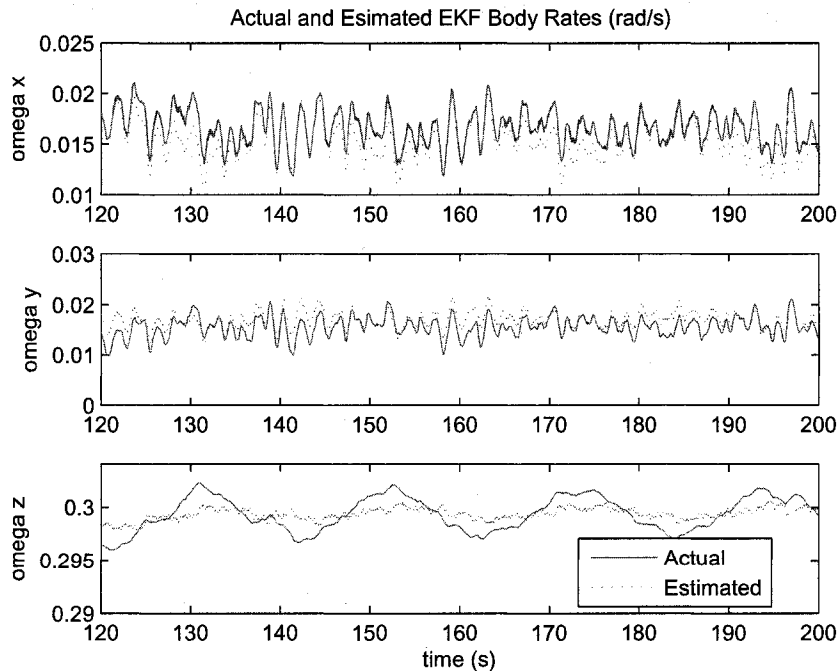


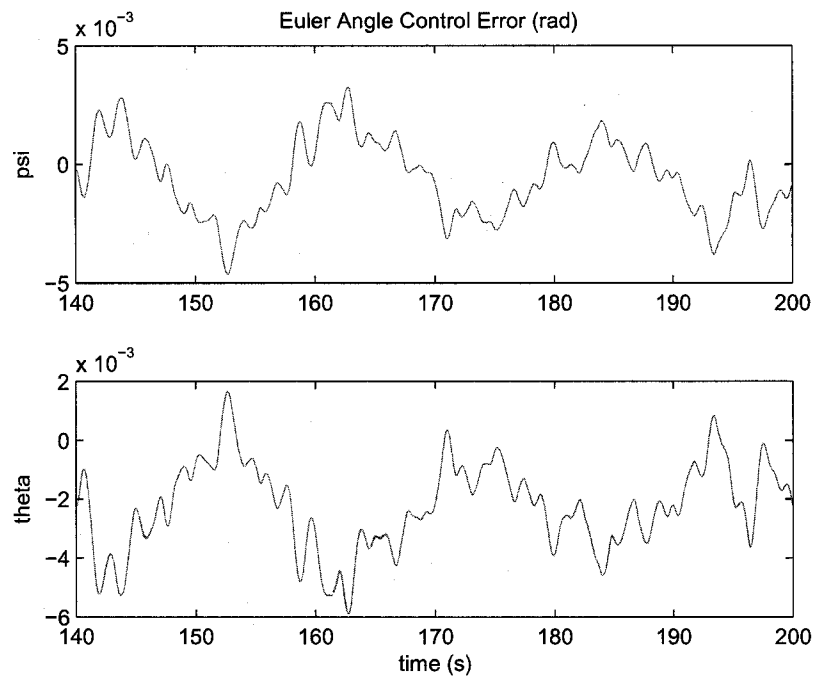Figure 8-28: EKF-Based SMC: Steady-State Actual and Estimated Body Rates

Figure 8-29: EKF-Based SMC: Steady-State Euler Angle Control Error
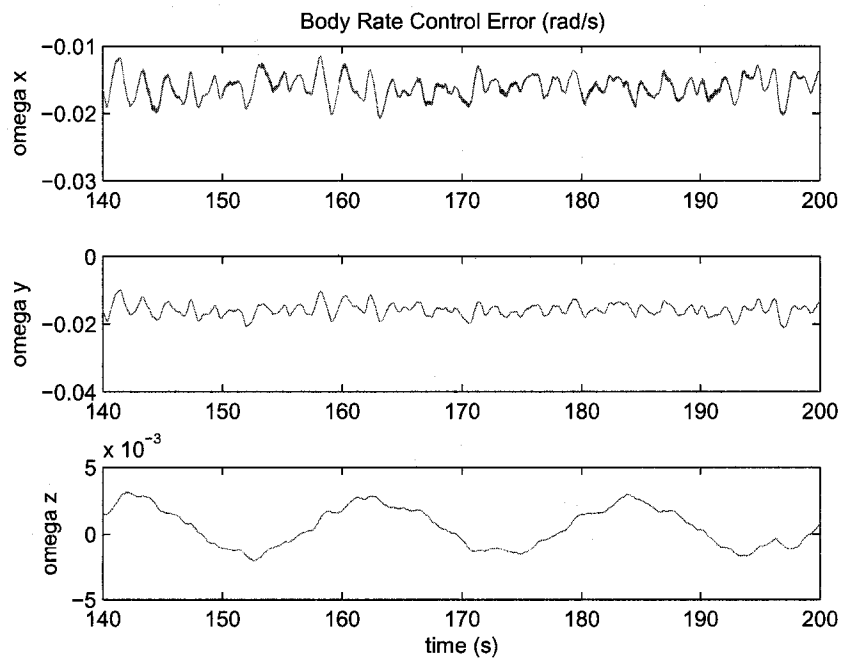


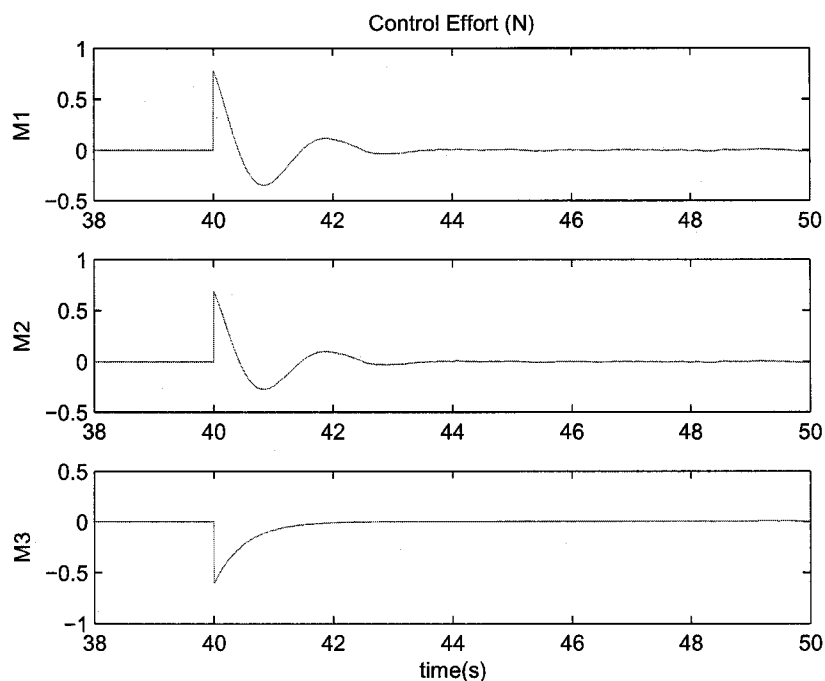Figure 8-30: EKF-Based SMC: Steady-State Body Rate Control Error

Figure 8-31: EKF-Based SMC Effort

It can also be seen in Figures 8-27 and 8-28 that the EKF is not as effective at tracking unknown disturbances when compared to the SMO in Figure 8-13. Since the EKF is not tracking these unknown disturbances, the controller is not capable of eliminating the oscillation of these states and error oscillations can result as seen in Figures 8-29 and 8-30. Control effort of the EKF-based SMC is optimal for all four cases. Figure 8-31 shows that the transient control effort is considerably smaller when compared to linear control techniques, while the settling time is increased to reduce large actuation of the satellite.

| | $\omega_x$ | $\omega_y$ | $\omega_z$ |
|---|---|---|---|
| Steady-State Error $(rad/s)$ | 0.015 | 0.015 | $\pm 0.001$ |
| Percent Error | - | - | 0.33 |

Table 8.9: Steady-State EKF-Based SMC: Body Rate Control Errors

| | $\psi$ | $\theta$ |
|---|---|---|
| Steady-State Error $(rad)$ | 0.0001 | 0.002 |
| Percent Error | 6.49 | 7.98 |

Table 8.10: Steady-State EKF-Based SMC: Euler Angle Control Errors

# CHAPTER 9

# CONCLUSIONS AND FUTURE WORK

## 9.1  Research Summary

In this research, flexible spacecraft boom dynamics of the NASA MMS satellite are investigated for future consideration in the proposed design of an observer-based attitude and nutation control algorithm. In the boom dynamic analysis, finite element methods are used to extract vibration characteristics to verify NASA results. Modal extraction and dynamic transient numerical analysis are the two methods used through the MSC.Marc finite element software in flexible dynamic modeling.

Also proposed in this research is the design and comparative analysis of nonlinear estimation and control algorithms for attitude and nutation control without the use of rate sensors. Euler angle dynamic models for spacecraft attitude are used in designing a Sliding Mode Observer and Extended Kalman Filter for full state estimation using only attitude sensors. These estimates are then implemented in a feedback control system that used a linear and Sliding Mode technique for maintaining satellite spin rate and attitude, while rejecting nutation. Proposed designs include a fully augmented observer-based control system incorporating measurement noise, parametric uncertainties and unknown disturbance torques to emulate flight conditions. Coupled with the finite element analysis, a fully flexible dynamic model proposed by Stoneking [26] is to be developed in future work for implementation on the proposed observer-based control systems.

Simulations for this research are done via MSC Marc Mentat 2005 r3 and MAT-

LAB / $Simulink^{TM}$ R2006a for finite element analysis and observer/control design, respectively. All finite element models are developed without the assistance of prior research. In regards to estimation and control design, Euler angle attitude models are adopted from [1].

The finite element analysis for flexible booms offered acceptable results for vibrational responses. NASA model results are confirmed through modal extraction and dynamic transient methods of vibrational analysis. In the process, it is also determined that dynamic transient methods offer accurate results of vibrational responses when a system is not fully constrained and modal extraction is impractical. In using dynamic transient simulations, it is also shown that numerical damping occurs with certain integration techniques in solving dynamic problems. The Newmark-Beta analysis does not have such numerical issues and should be utilized in future research in which vibrational responses of dynamic systems are to be investigated through dynamic transient methods. Numerical instabilities do, however, occur in dynamic analysis of rotation systems. While attempting to rotate the satellite model at 3 rotations per minute about, the inability of the software to transform coordinates after 90 degrees of rotation caused the rotation to cease. When such constraints on coordinate transformations are removed, or when the coordinate system is changed to cylindrical coordinates, the model began to expand in the radial direction. These inaccurate simulation results indicate that there are numerical instabilities that occur in dynamic transient simulations in which rotational motion is experienced. This numerical instability was confirmed by MSC support engineers, and proven to be insurmountable in the scope of this research. Overcoming this numerical instability in dynamic transient analysis through future research could have implications on several design and analysis situations in which coordinate transformations can cause inaccurate results.

For attitude and body rate estimation with only star tracker attitude measurements available, three different observers are explored. The linear Kalman filter is insufficient in providing estimates that will allow for effective control. The Sliding Mode Observer (SMO) and Extended Kalman Filter (EKF) are the two nonlinear state estimation techniques designed for the MMS application. Both offered acceptable results for attitude and body rate estimation given measurement noise, parametric uncertainties and disturbance torques. The results presented in Chapter 6 clearly illustrate the strengths and weaknesses of the EKF and SMO. The EKF does an exceptional job at filtering measurement noise for all six states. However, its weakness is in tracking satellite states with unknown disturbance torques and parametric uncertainties. Results illustrate a larger magnitude of error oscillation as compared to the SMO, due to the inability of the EKF to effectively track satellite states, especially body rates which are being directly influenced by external torques. Conversely, the SMO has slightly more noise in the estimation error signals. However, the magnitude of error oscillation is reduced through effective tracking of unknown disturbances. In either design, acceptable estimates of all six states, while only measuring satellite orientation, allowed for progression to the control development.

Not only are feedback gains, sliding surfaces, and weight matrices tuned for the development of the SMO and EKF, but also observer correction inputs are investigated for their influence on observer performance. During the estimation process, the observer works off error produced between measured attitude data, and the same estimated states. As can be seen in the results, both estimators effectively force the estimation error close to zero, however, error still exists in body rate signals. When observer parameters are exhaustively tuned, the estimation input correction terms are monitored to understand their influence on the overall observer performance. It is determined that by tuning the observer correction inputs, tracking results could

be improved for body rate estimation. Correction terms are tuned through trial and error simulations, in which tracking effectiveness is the most important performance characteristic in the final design. Noise amplification is another design parameter that is monitored in tuning estimation correction inputs. Although there is a limit to these fixed, tuned gains because of their amplification of noise in the signals, they do vastly improve results. Further analysis of this type of tuning is necessary since the gains are acquired for given initial conditions, noise characteristics, and unknown disturbances. Ranges of satellite operating conditions need to be determined for the given set of correction terms and their effectiveness for a wide range of system characteristics.

Control design commenced with the development of linear and nonlinear control techniques assuming all states are perfectly known. This allowed for insight into the ability of each controller given optimal operating conditions, and measurements of satellite states. Upon completion, these feedback controllers are implemented with EKF and SMO systems.

The linear, proportional and derivative (PD) control, and nonlinear Sliding Mode Control are both tested on state estimates to determine the overall most effective system for observer-based attitude and nutation control. Results in Chapter 8 offer acceptable results for a few different systems. The EKF, although optimal in measurement noise filtering, does not offer acceptable results when implemented with a linear feedback controller. The derivative feedback error signal resulted in excessive control noise that can cause actuator failure. Also, since the EKF is ineffective at tracking states with unknown disturbance torques, the control system is incapable of recognizing them in the error signal and acceptable control compensation does not occur.

The SMC is far more effective at rejecting nutation, and maintaining attitude while filtering measurement noise. Feedback control implementation with SMO also offers

acceptable results based on NASA design criteria. Linear feedback control again resulted in control signals with significant noise. However, the SMO's robustness allowed for effective rejection of unknown torques and disturbances compared to the EKF, with SMC implementation.

## 9.2 Future Work

Future work includes:

- augmentation of the attitude estimation and control algorithm with orbital state estimation and control. The MMS will require two orbital transfers during its mission in which the orbit must be known using minimal sensors, and a velocity change must be obtained. The coupling between attitude and orbital states will be essential to ensure that during and after orbital transfers, satellite reorientation can occur and flexible boom vibrations and deflections can be minimized.

- implementing a fully flexible spacecraft model into the estimation and control algorithms for investigation of boom vibrations during attitude correction and orbital transfers. The modal analysis that produced natural frequencies and mode shapes can be used to develop a discretized flexible spacecraft model based on "Multiple Bodies Connected by Spherical Joints in a Tree Topology" [26]. It is important to know whether flexible modes of vibration are excited during the spacecraft mission.

- investigating closed loop system stability using Monte-Carlo simulations for all possible initial conditions, unknown disturbances, and large angle orbital maneuvers. Since there is no guaranteed closed loop stability in using the Extended Kalman Filter, it will be imperative to run the system under all

possible conditions.

- inserting thruster models and allowable pulse widths into the control sequence. This will emulate the spacecraft's response to actual thruster firings and ensure that satellite dynamics will remain stable, even after discritization of the actuator signal.

- implementing star tracker measurement models into the simulations. This will provide insight into actual measurement noise characteristics, and ensure that system stability is still valid under discrete measurements.

- testing the system under quaternion attitude models. Quaternions insure that singularities do not occur during simulations due to inverse trigonometric functions in Euler angle models (also referred to as gimbal lock). In most instances, attitude measurement devices output in quaternions and it will be necessary to evaluate the proposed observer-based control systems under quaternion based states.

- investigating numerical instabilities in dynamic transient analysis by finite element methods for large displacement rotations. Allowing for a fully elastic model of complex structures experiencing time-varying loads, and evaluating their dynamic response through finite elements could be vital in many engineering applications. This type of research would also be very useful to many software packages in which dynamic transient analysis is available, but incapable of analyzing bodies experiencing large rotational displacements.

- investigating alternative control methods such as H-infinity and adaptive control techniques. Comparing results of control for perfect state knowledge and observer-based control systems indicate that the control system, and not the observer, is the limiting factor in closed-loop system performance. It will be

important in exploring alternative control techniques that could improve nutation control specifically.

Both observer-based systems met NASA design requirements. However, the trade-off is in system robustness, and effective measurement noise filtering. The proposed research offers promising results to meet the requirements of attitude and nutation control without the use of rate sensors. It is in the authors opinion that the EKF and SMO based SMC systems offer the most comprehensive control options given the MMS mission. A complete flexible dynamic model will be useful in determining observer and control system effectiveness and understanding flexible structure responses under orbital and attitude maneuvers.

# BIBLIOGRAPHY

[1] K. Koprubasi. Spacecraft attitude and angular rate estimation using sliding mode observers. Master's thesis, University of New Hampshire, 2004.

[2] U. Lee. "Dynamic continuum modeling of beamlike space structures using finite-element matrices". *Journal of Spacecraft and Rockets*, 28(4):725–731, 1990.

[3] D.V. Hutton. "Modal analysis of a deployable truss using the finite element method". *Journal of Spacecraft and Rockets*, 21(5):468–472, 1984.

[4] E.A Wheater, P.K. Pal, and T.J. Anderson. "New total-lagrangian fea and experiments on highly flexible structures". In *Proceedings of the 38th Annual AIAA/ASME Conf. on Structures, Structural Dynamics and Materials, April, 1997*, pages 1843–1852.

[5] J.R. Wertz (Ed.). *Spacecraft Attitude Determination and Control*. D.Reidel, Dordrecht, The Netherlands, 1978.

[6] M.H. Kaplan. *Modern Spacecraft Dynamics and Control*. Wiley, New York, 1989.

[7] M. J. Sidi. *Spacecraft Dynamics and Control*. Cambridge University Press, 1997.

[8] L. H. Grasshoff. "An onboard, closed-loop, nutation control system for a spin-stabilized spacecraft". *Journal of Spacecraft and Rockets*, 5:530–535, 1968.

[9] H.S Lin. "Spin-down and active nutation controller for the galileo project". *Journal of Guidance, Control, and Dynamics*, 5(2):181–188, 1982.

[10] da Silva W.C and L.C. de Souza. "Spin reduction of space vehicles using gas jets. *Space Mechanics and Control Division-DMC, National Institute for Space Research.*

[11] E.J. Lefferts, F.L. Markley, and M.D. Shuster. "Kalman filtering for spacecraft attitude estimation". *Journal of Guidance, Control, and Dynamics*, 5(5):417–429, 1982.

[12] M.L. Psiaki, F. Martel, and P.K. Pal. "Three-axis attitude determination via Kalman filtering of magnetometer data". *Journal of Guidance, Control and Dynamics*, 13(3):506–514, 1990.

[13] E. Gai, K. Daly, J. Harrison, and L. Lemos. "Star-sensor-based satellite attitude/attitude rate estimator". *Journal of Guidance, Control and Dynamics*, 8(5):560–565, 1985.

[14] J.L. Crassidis and F. L. Markley. "Predictive filtering for attitude estimation without rate sensors". *Journal of Guidance, Control, and Dynamics*, 20(3):522–527, 1997.

[15] A.G. Luk'yanov, S.J. Dodds, and J. Vittek. "Observer-based attitude control in the sliding mode". In *Proceedings of the 1996 3rd International Conference on Dynamics and Control of Structures in Space, SPACE 96.*

[16] E.A. Misawa. *Nonlinear State Estimation Using Sliding Observers.* PhD thesis, Massachusetts Institute of Technology, 1988.

[17] J.-J. E. Slotine, J. K. Hedrick, and E. A. Misawa. "On sliding observers for nonlinear systems". *Journal of Dynamic Systems, Measurement and Control*, 109(3):245–252, 1987.

[18] A.H. Gale and P. Likins. "Influence of flexible appendages on dual-spin spacecraft dynamics and control". *Journal of Spacecraft and Rockets*, 7(9):1049–1056, 1970.

[19] B. Wei and C.T. Plescia. "Attitude stabilization of flexible spacecraft during stationkeeping meaneuvers". *Journal of Guidance, Control and Dynamics*, 7(4):430–436, 1984.

[20] L. Meirovitch and H. Baruch. "Optimal control of damped flexible gyroscope systems". *Journal of Guidance, Control and Dynamics*, 4(2):157–163, 1981.

[21] H. Sira-Ramirez and T. Dwyer. "Variable structure controller design for spacecraft nutation damping". *IEEE Transactions on Automatic Control*, 32(5):435–438, 1987.

[22] D. J. Logan. *A First Course in the Finite Element Method.* Thomson Learning, Inc., 2002.

[23] D. V. Hutton. *Fundamentals of Finite Element Analysis.* McGraw-Hill, 2004.

[24] K. J. Bathe. *Finite Element Procedures in Engineering Analysis.* Prentice-Hall, Inc., 1992.

[25] B. Wei. *Space Vehicle Dynamics and Control.* American Institute of Aeronautics and Astronautics, Inc., 1998.

[26] E. Stoneking. "Equations of motion for a spacecraft composed of multiple rigid bodies connected by spherical joints in a tree topology". *NASA Goddard Space Flight Center*, 2006.

[27] L. Syrmos. *Optimal Control.* John Wiley and Sons, Inc., 1995.

[28] A. Gelb. *Applied Optimal Estimation.* MIT Press, Cambridge MA, 1994.

[29] M. J. Sidi and R. D. Harbor. *Feedback Control Systems.* Prentice-Hall, Inc., 1991.

# APPENDICES

# APPENDIX A

# Estimation Diagrams & MATLAB FILES

Included here are the necessary MATLAB/Simulink models for attitude estimation through a linear Kalman filter, Extended Kalman Filter and Sliding Mode Control. The MATLAB file **mms simulation code** is used to define spacecraft parameters, select feedback gains, and run MATLAB routines to solve Ricatti equations.
**mms simulation code.m**

```
%Spacecraft Moments of Inertia (kg-m^2)
Ix=8402.64
Iy=8411.97
Iz=16414.66
%Observer Moments of Inertia (kg-m^2)
Ixo=8000
Iyo=8600
Izo=17500
%Cross products of Inertia (kg-m^2)
Ixy=-58.8
Ixz=-44.6
Iyz=-100
delta=Ix*Iy*Iz-Ix*(Iyz^2)-(Ixy^2)*Iz-2*Ixy*Ixz*Iyz-(Ixz^2)*Iy
%SMO gains
k1=.001
k2=.001
k3=.001
k4=.001
k5=.001
k6=.001
phi=.0006
%EKF R inverse
R11=.0000010
R22=.0000010
R33=.0000010
%Kalman filter
n=.3
lamda=((Iz-Ix)/Ix)*n
A=[0 0 0 1 0 0; 0 0 0 0 1 0; 0 0 0 0 0 1; 0 0 0 0 -lamda 0; 0 0 0 lamda
0 0; 0 0 0 0 0 0]
C=[1 0 0 0 0 0; 0 1 0 0 0 0; 0 0 1 0 0 0]
G=[1 0 0 0 0 0; 0 1 0 0 0 0; 0 0 1 0 0 0; 0 0 0 1 0 0; 0 0 0 0 1 0; 0 0
0 0 0 1]
Q=[.01 0 0 0 0 0; 0 .01 0 0 0 0; 0 0 .01 0 0 0; 0 0 0 20000 0 0; 0 0 0 0
20000 0; 0 0 0 0 0 20000]
R=[10000 0 0; 0 10000 0; 0 0 10000]
NN=[0; 0]
SYS=ss(A,G,C,0)
[KEST,L,P]=KALMAN(SYS,Q,R)
%Linear Control Gains
alpha_des=[0.052;-0.052];          %Desired Euler Angles (rads)
omega_des=[0;0;0.3];               %Desired Body Rates (rads/s)
```

```
K_alpha=[300 50; 50 300; 0 0];
K_omega=[20 1 0; 1 20 0; 0 0 20];
K=[K_alpha K_omega]
K_d=0.1*K
%Sliding Mode Control
%Luenberger Gains
K_alpha_smc=1*[10 0; 0 10; 0 0];
K_omega_smc=1*[2 0 0; 0 2 0; 0 0 2];
K_smc=[K_alpha_smc K_omega_smc];
%SMC Gains
H_alpha_smc=.01*[5 0; 0 5; 0 0];
H_omega_smc=.001*[1 0 0; 0 1 0; 0 0 1];
H_smc=[H_alpha_smc H_omega_smc];
rho=.01;
lamda1=1
lamda2=.5
```

## A.1 Kalman Filter

The simulation diagram for the Kalman filter and system equations are shown below.
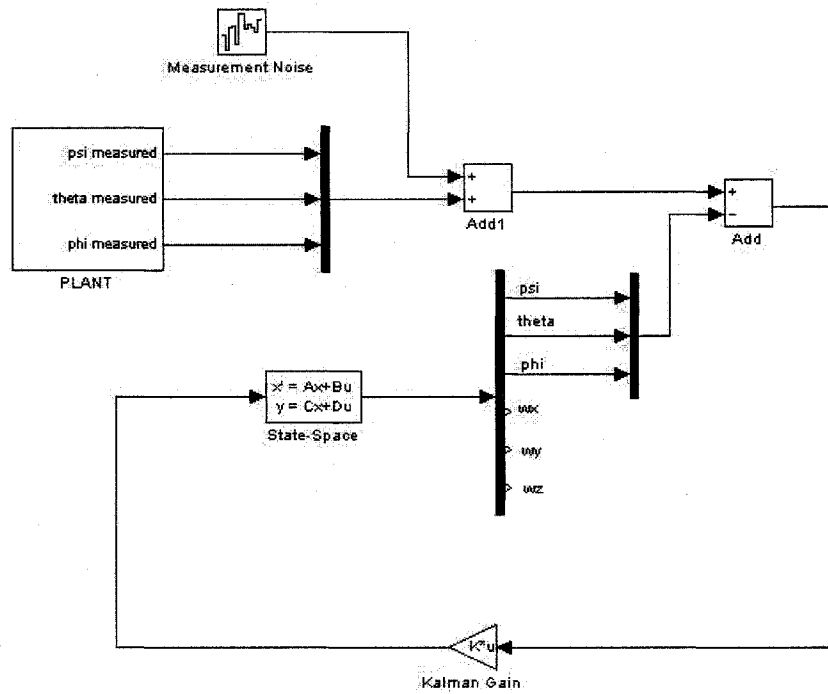


Figure A-1: Main Block Diagram - Kalman Filter
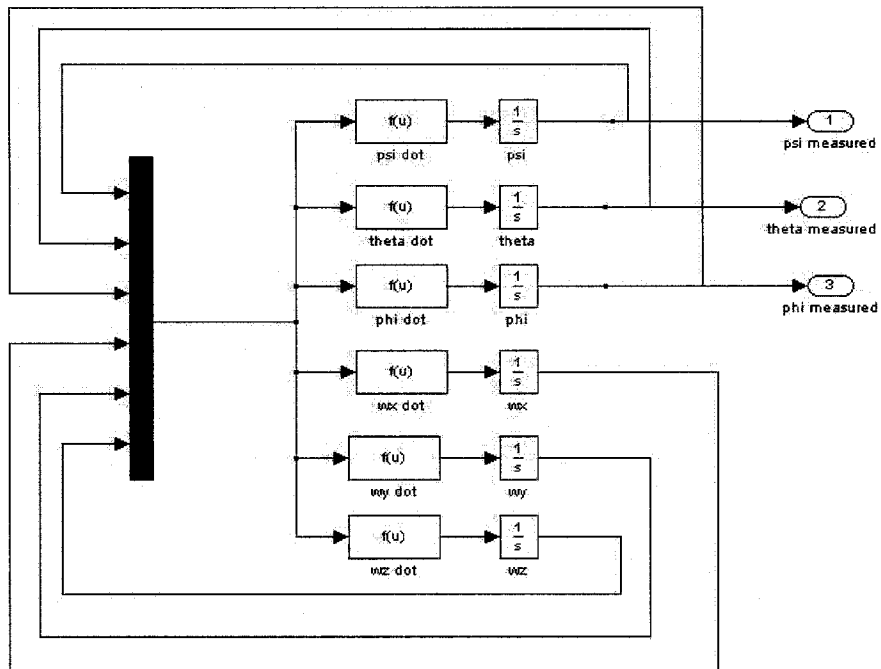
Figure A-2: Plant Sub-block

## A.2   Extended Kalman Filter

Simulation diagrams for the EKF are shown below. The linearized system equations that are updated with each estimate defined in the simulation diagrams as $F$ are shown in Figure A-10
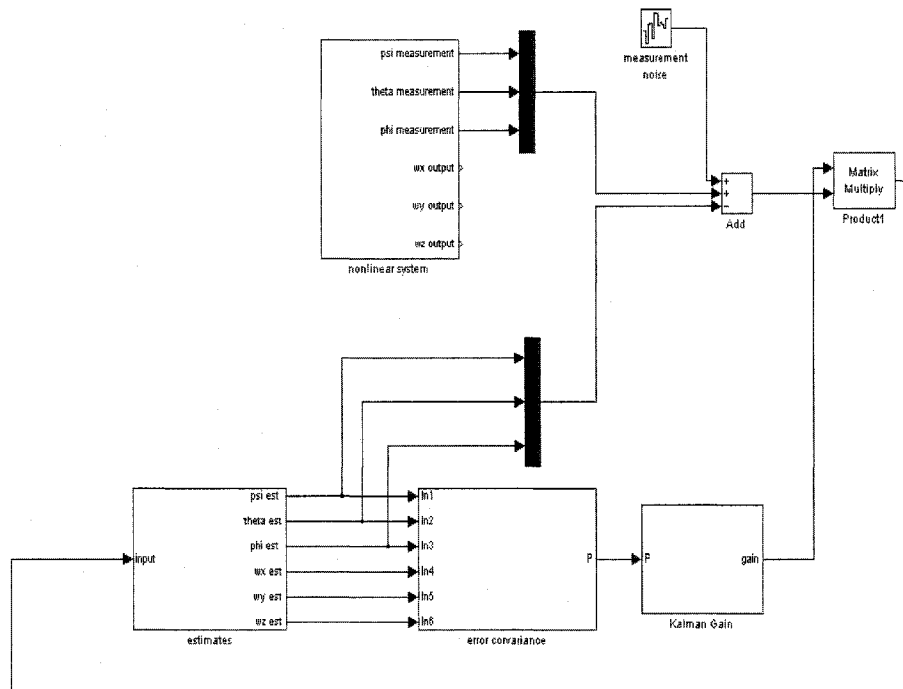


Figure A-3: Main Block Diagram - Extended Kalman Filter
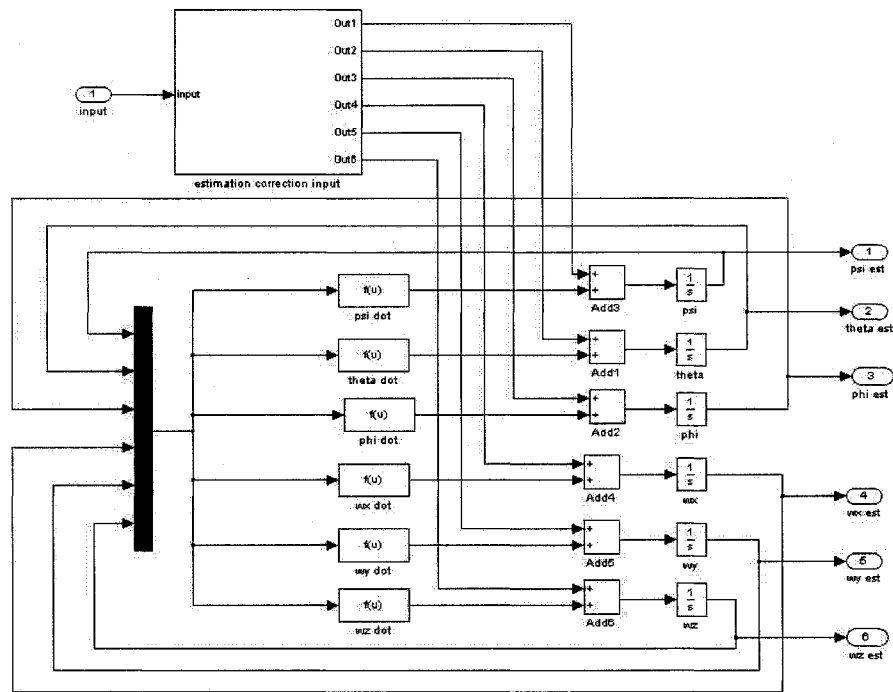
Figure A-4: Estimates Sub-block
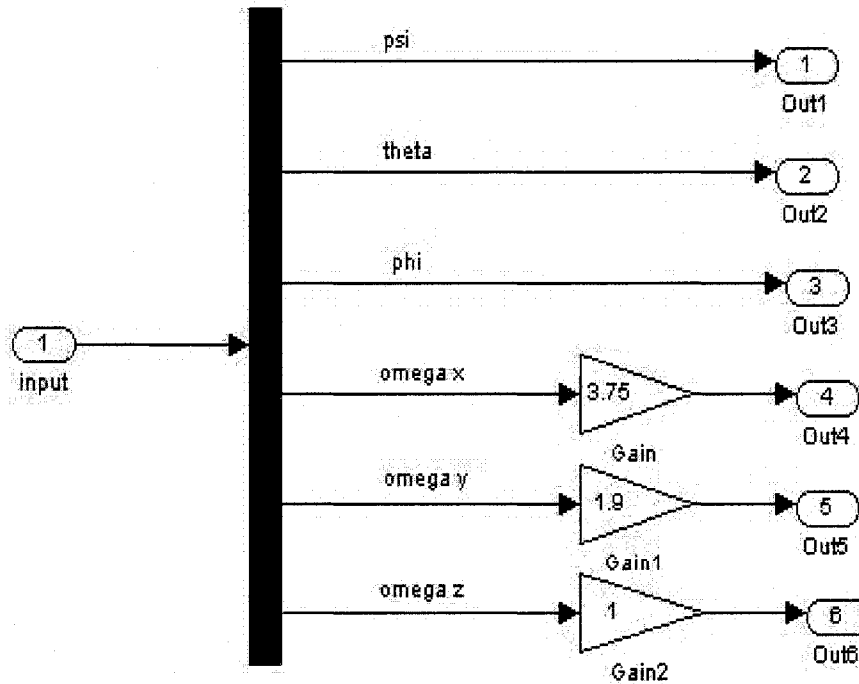


Figure A-5: Estimation Correction Input Sub-block
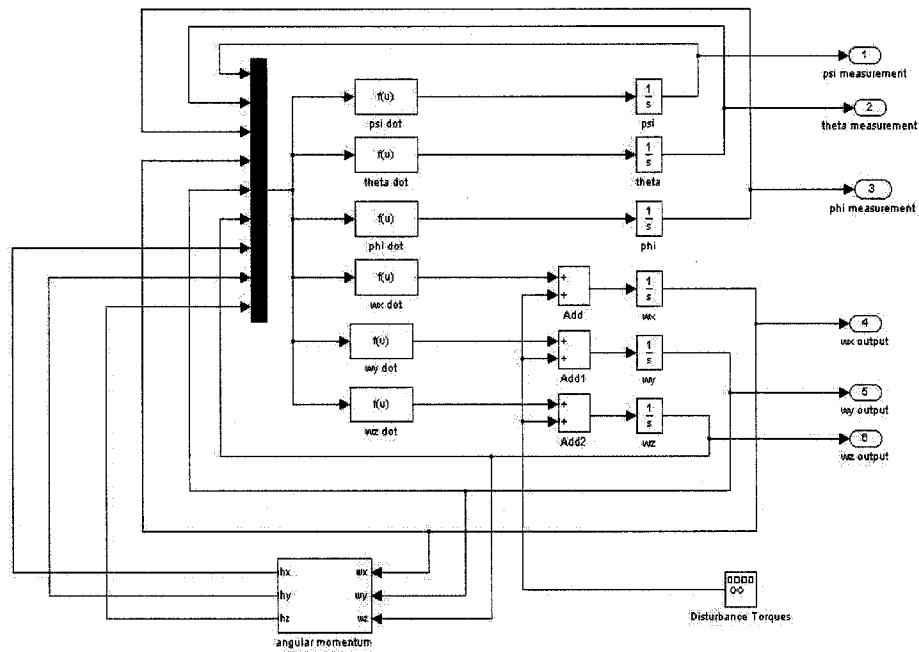
Figure A-6: Nonlinear System Sub-block
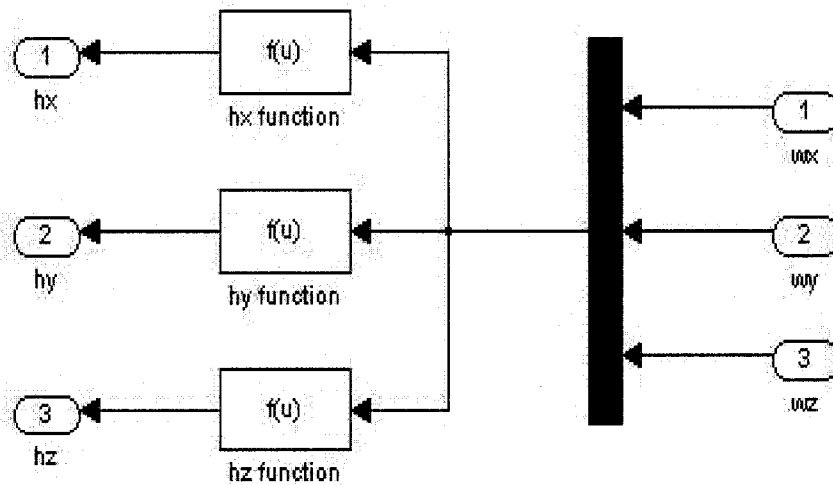


Figure A-7: Angular Momentum Sub-block
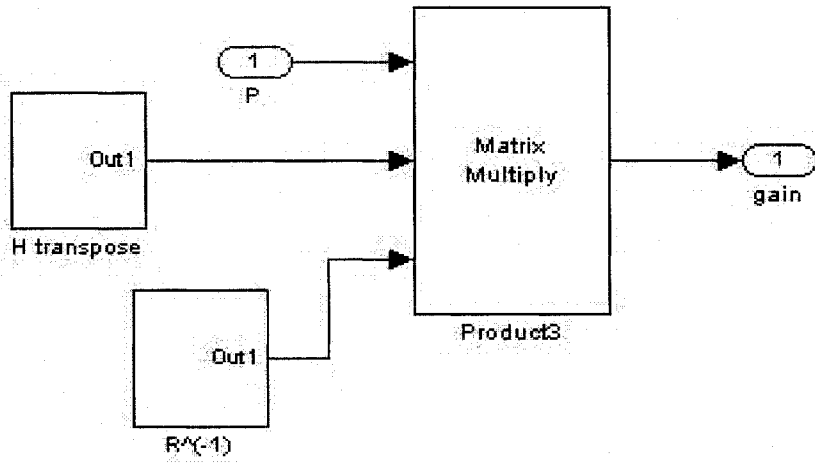
Figure A-8: Kalman Gain Sub-block
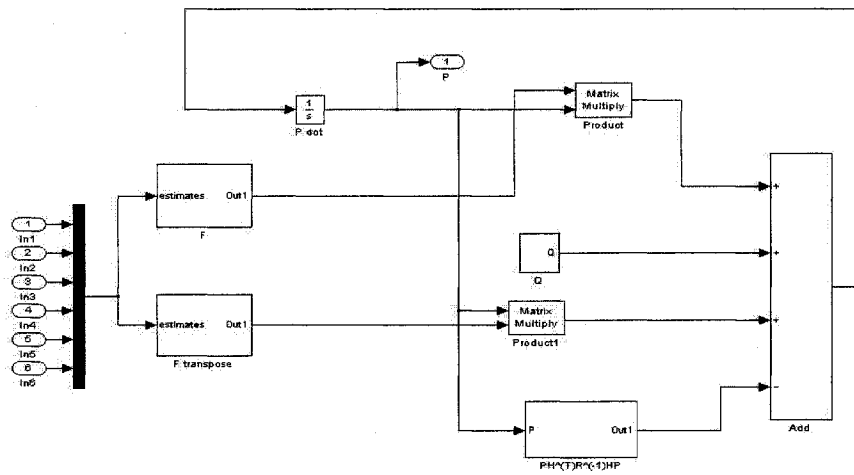


Figure A-9: Error Covariance Sub-block

$$F(\hat{x}(t),t) = \begin{bmatrix} -\hat{\omega}_x \tan\theta\sin\psi + \hat{\omega}_y \tan\theta\cos\psi & \hat{\omega}_x \sec^2\theta\sin\psi + \hat{\omega}_y \sec^2\theta\cos\psi & 0 & 1 & \tan\theta\sin\psi & \tan\theta\cos\psi \\ -\hat{\omega}_y \sin\psi - \hat{\omega}_x \cos\psi & 0 & 0 & 0 & \cos\psi & -\sin\psi \\ -\hat{\omega}_x \sec\theta\sin\psi + \hat{\omega}_y \sec\theta\cos\psi & \hat{\omega}_x \sec\theta\tan\theta\cos\psi + \hat{\omega}_y \sec\theta\tan\theta\sin\psi & 0 & 0 & \sin\psi\sec\theta & \cos\psi\sec\theta \\ 0 & 0 & 0 & 0 & \hat{\omega}_z\frac{I_y - I_z}{I_x} & \hat{\omega}_y\frac{I_y - I_z}{I_x} \\ 0 & 0 & 0 & \hat{\omega}_z\frac{I_z - I_x}{I_y} & 0 & \hat{\omega}_x\frac{I_z - I_x}{I_y} \\ 0 & 0 & 0 & \hat{\omega}_y\frac{I_x - I_y}{I_z} & \hat{\omega}_x\frac{I_x - I_y}{I_z} & 0 \end{bmatrix}$$

Figure A-10: System Jacobian Matrix
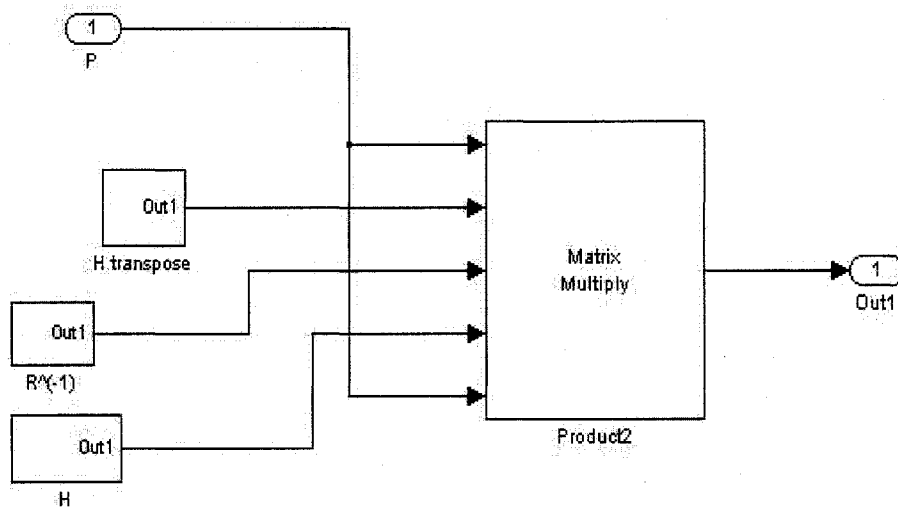


Figure A-11: $PH^T R^{-1} HP$ Sub-block

## A.3 Sliding Mode Observer

Sliding Mode Observer simulation diagrams are listed below. Nonlinear system and Estimates sub-blocks are identical to those found in EKF simulations. Figure A-12 shows the main block diagram of the Sliding Mode Observer.
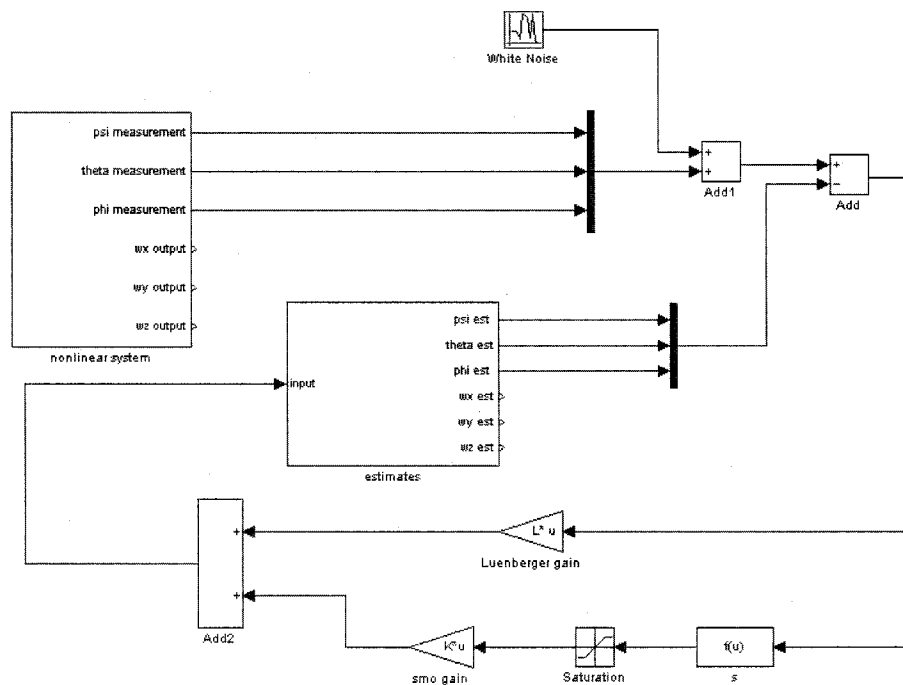


Figure A-12: Main Block Diagram - Sliding Mode Observer

# APPENDIX B

# Control Diagrams & MATLAB FILES

Included here are the necessary MATLAB/Simulink models for the attitude and nutation control implemented with perfect measurement data, Extended Kalman Filter and Sliding Mode Observer. Simulation code can be found in Appendix A.

## B.1 Perfect Measurements

Figures B-1 and B-2 represents the simulation diagram for feedback control and the governing nonlinear equations respectively assuming perfect measurements. Figures B-3 and B-4 are the linear feedback control and Sliding Mode Control simulation diagrams respectively. The input limiter Figures B-6 and B-7 and control sub-blocks will be identical for observer-based control simulations.
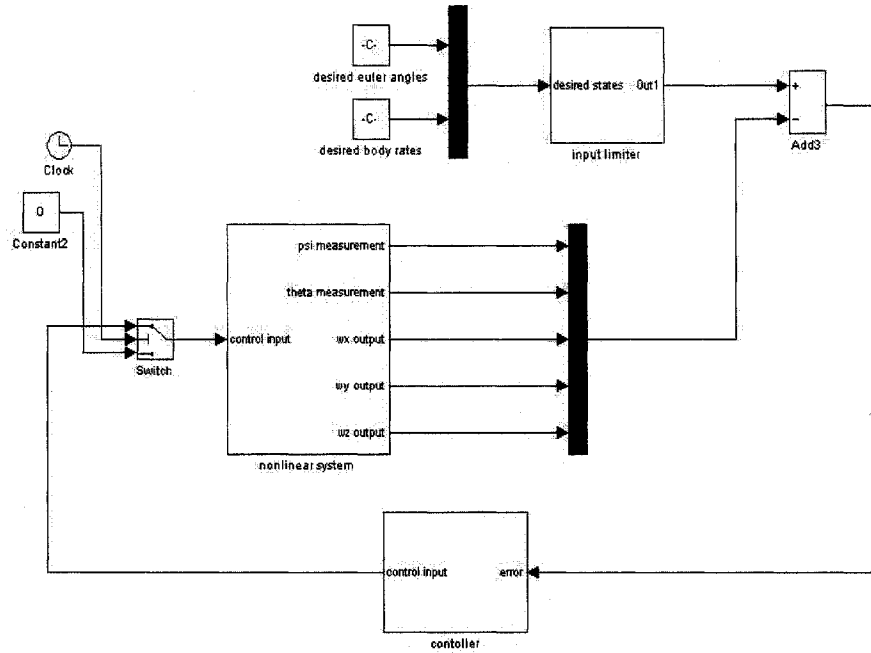
Figure B-1: Main Block Diagram - Feedback Control of Perfect Measurements
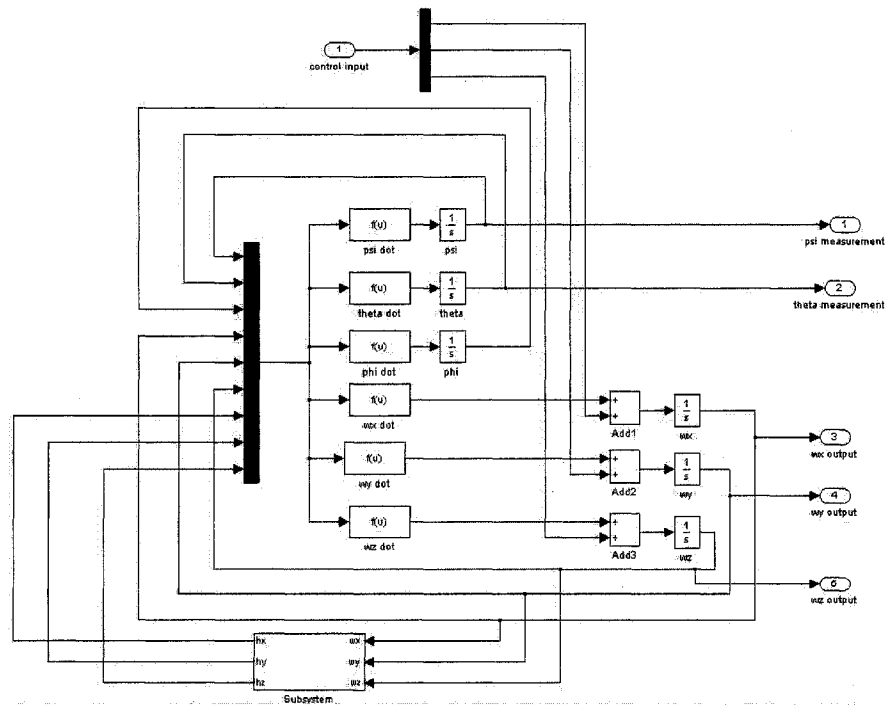


Figure B-2: Nonlinear System Sub-block
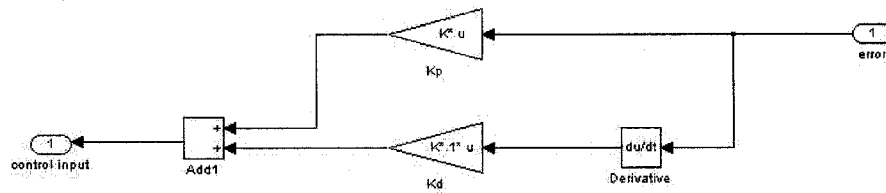
Figure B-3: Controller Sub-block (Linear)
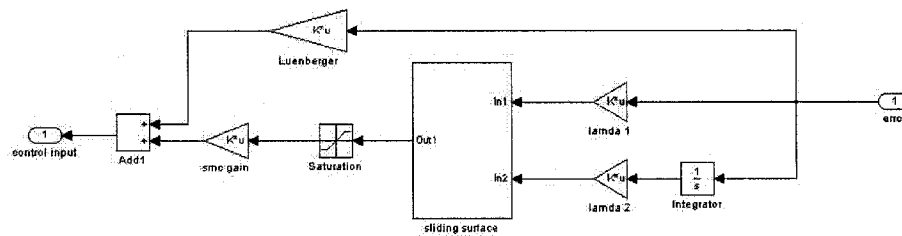


Figure B-4: Controller Sub-block (Sliding Mode Control)
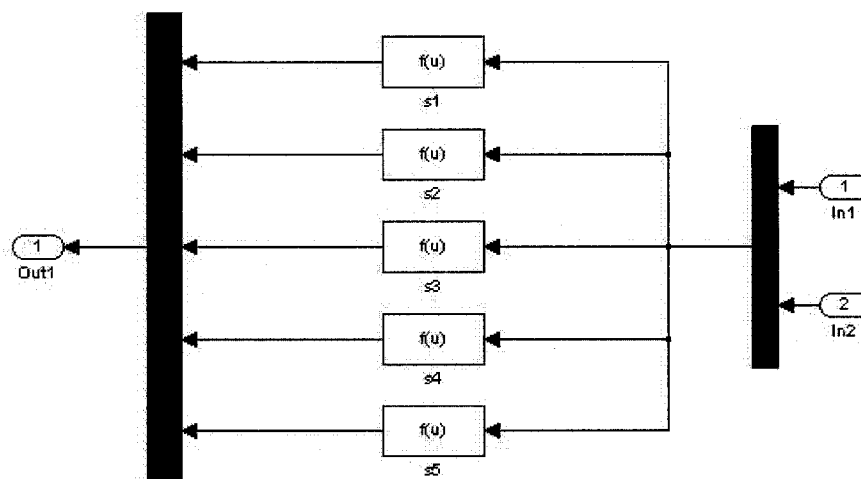


Figure B-5: Sliding Surfaces Sub-block
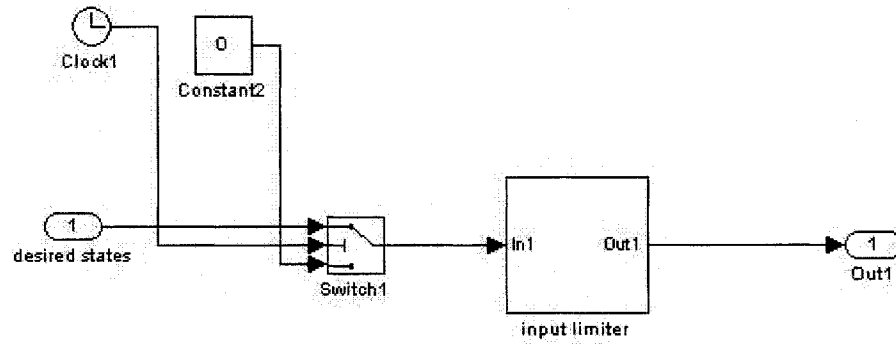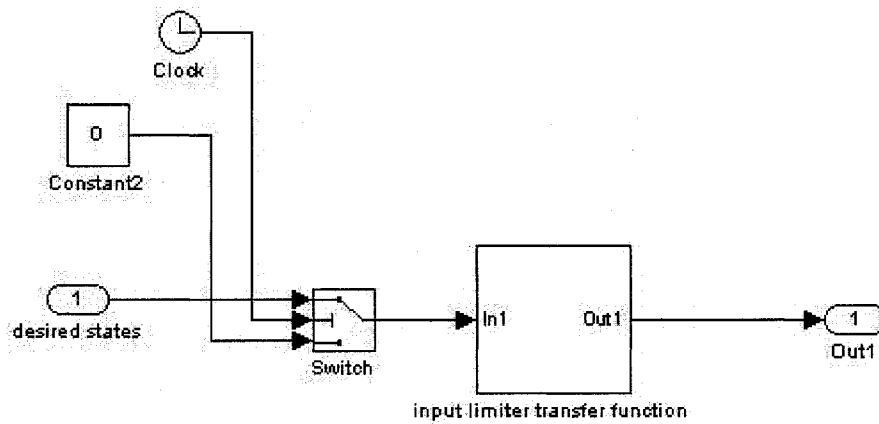
Figure B-6: Input Limiter Sub-block



Figure B-7: Input Limiter Transfer Function Sub-blok

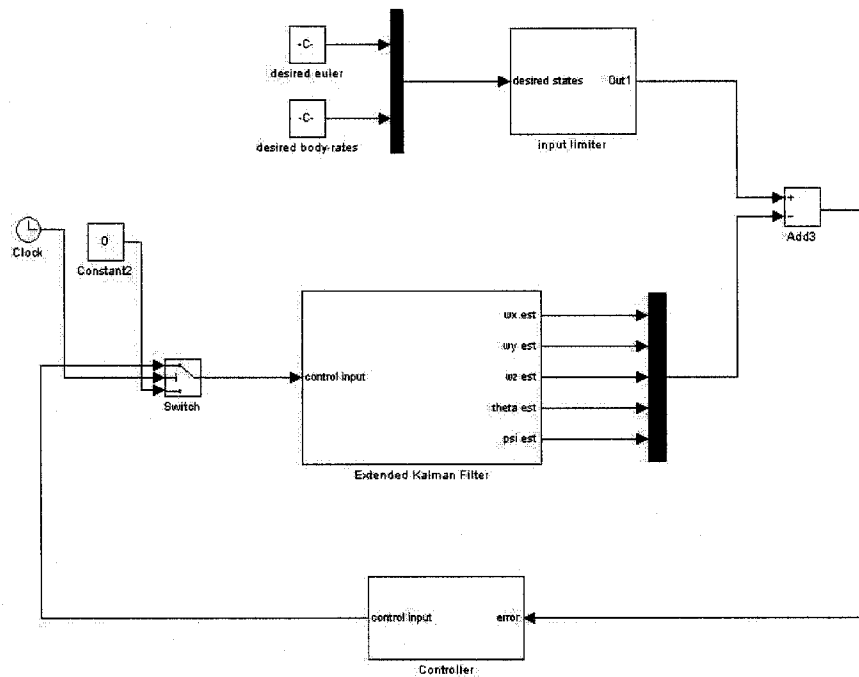Figure B-8: Main Block Diagram - EKF Based Feedback Control

## B.2   Extended Kalman Filter Based Control

Included below are Extended Kalman Filter based control systems. Figure B-8 shows the main simulation of the observer-based controller while Figure B-9 is the EKF that outputs state estimates for control use. Figures B-10 and B-11 illustrate control inputs for the system and observer dynamics respectively, while all other EKF sub-blocks can be found in Appendix A.
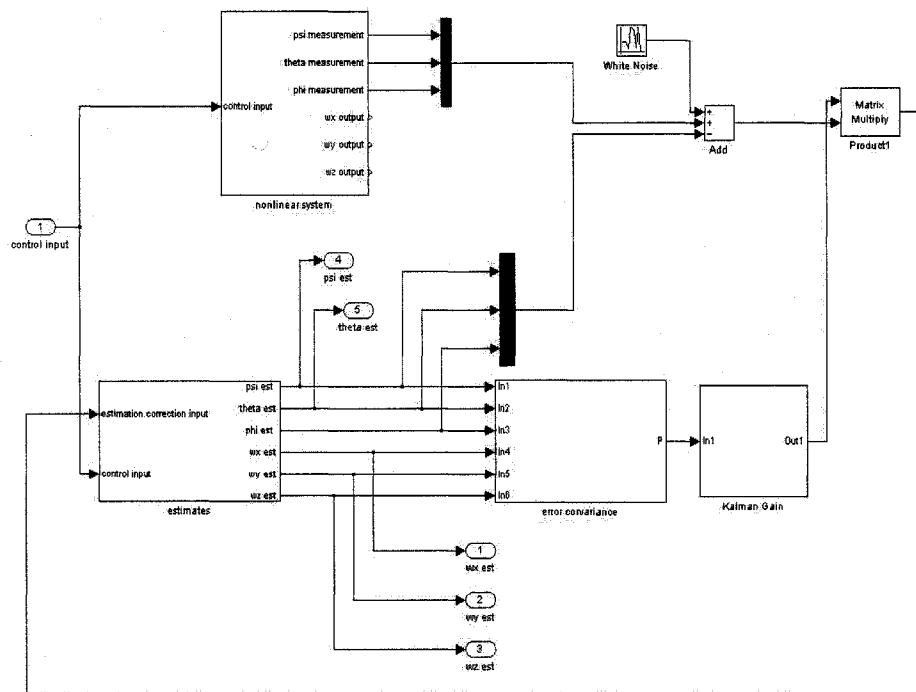
Figure B-9: Extended Kalman Filter Sub-block
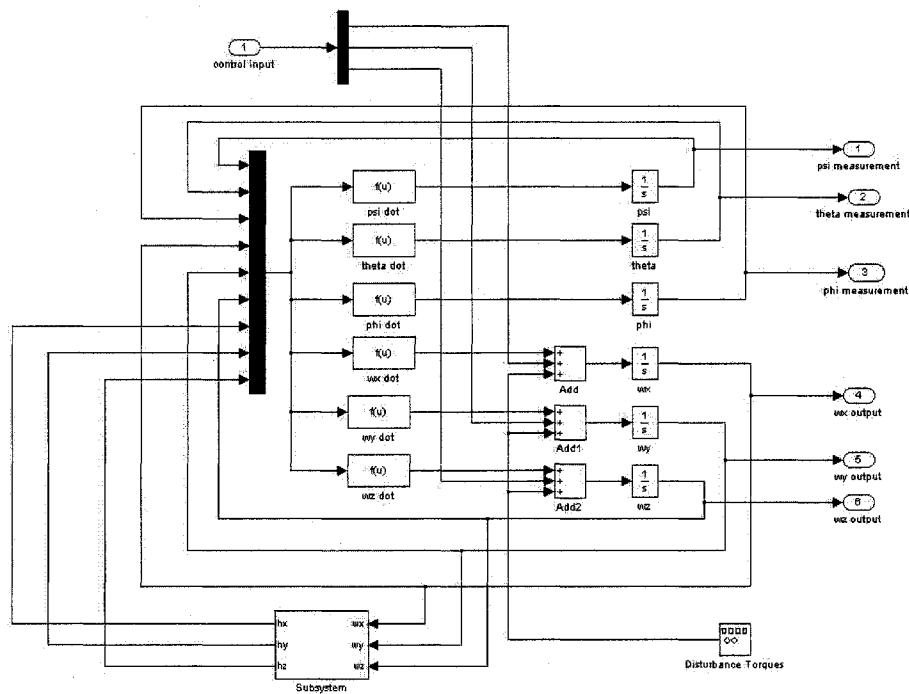


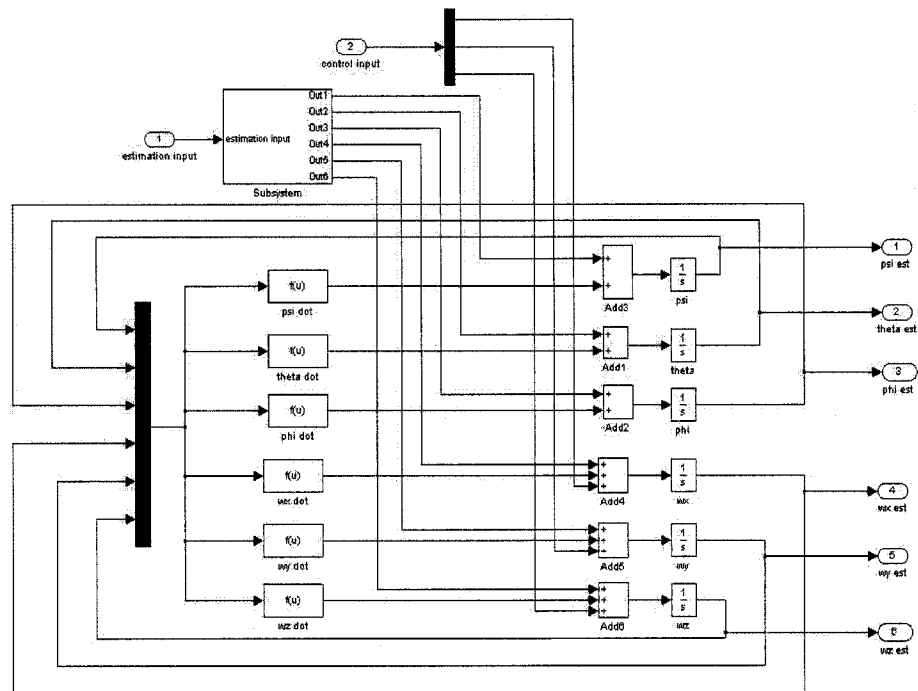Figure B-10: Nonlinear System Sub-block

Figure B-11: Estimates Sub-block

## B.3 Sliding Mode Observer Based Control

Simulation diagrams of Sliding Mode Observer based feedback control are shown in Figures B-12 and B-13. All sub-blocks related to the SMO can be found in Appendix A while nonlinear system, estimator and controller diagrams can be found in the above sections.
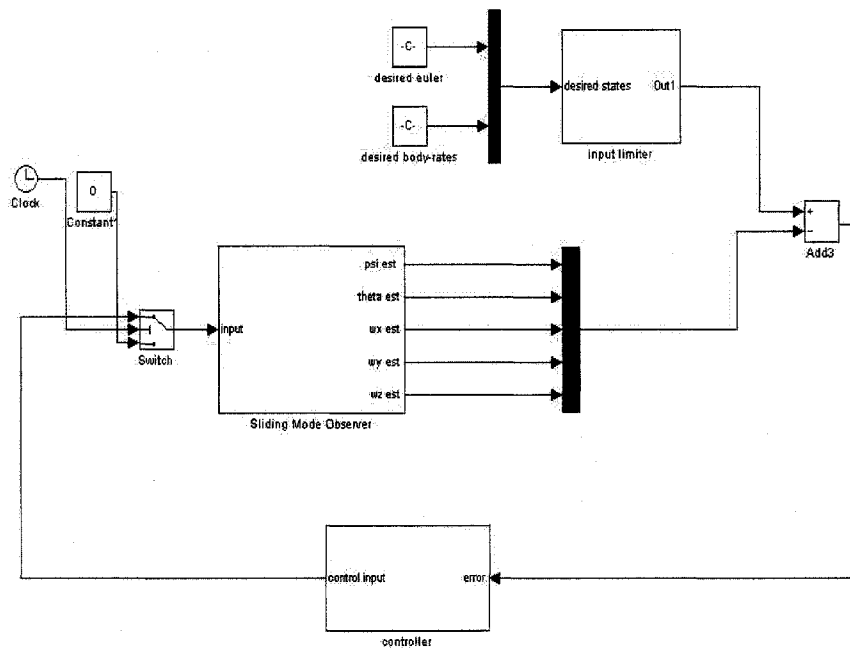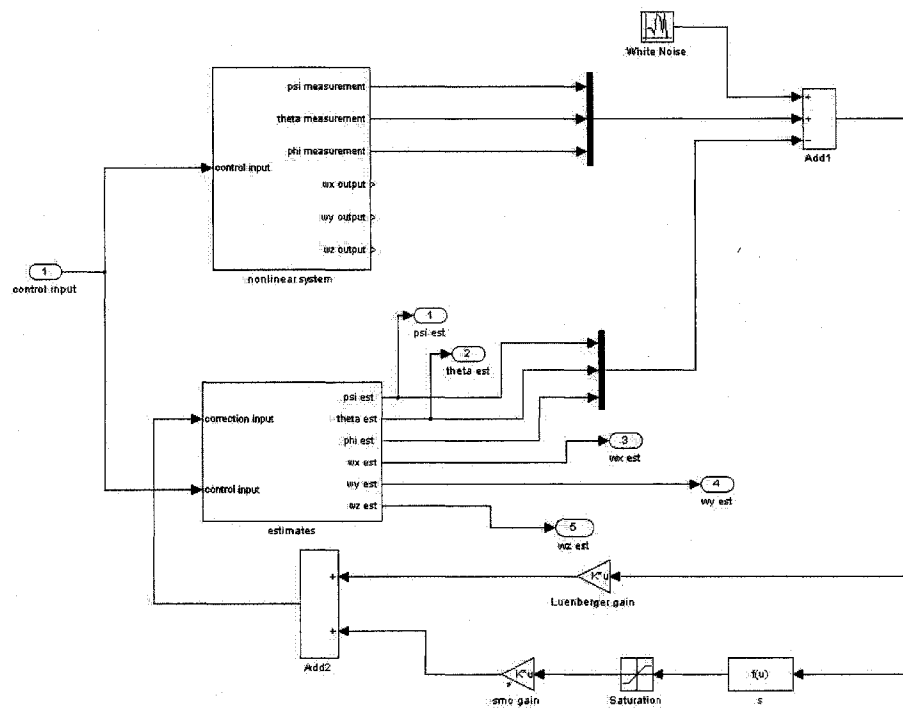


Figure B-12: Main Block Diagram - SMO Based Feedback Control

Figure B-13: Sliding Mode Observer Sub-block